UNIVERSITY OF CALIFORNIA SAN DIEGO

Novel genetic strategies to probe mechanisms underlying neuronal development and circuit formation

A dissertation submitted in partial satisfaction of the requirements for the degree Doctor of Philosophy

in

Neurosciences

by

Benjamin Taylor Throesch

Committee in charge:

Professor Kristin Baldwin, Chair
Professor Alysson Muotri, Co-chair
Professor Brenda Bloodgood
Professor Nicholas Spitzer
Professor Lisa Stowers

2020

The dissertation of Benjamin Taylor Throesch is approved, and it is acceptable in quality and form for publication on microfilm and electronically:

_____

_____

_____

_____
Co-chair

_____
Chair

University of California San Diego

2020

DEDICATION

To my parents for encouraging me from the start –

To my siblings for providing healthy competition throughout –

To my friends for always keeping my glass full –

To my husband for supporting and suffering through this with me –

And to myself for never giving up on this dream –

WE DID IT!

TABLE OF CONTENTS

LIST OF ABBREVIATIONS

ACSF	Artificial cerebral spinal fluid
ACx	Auditory cortex
AR	Antigen retrieval
CB	Cerebellum
CC	Corpus callosum
CC-3	Cleaved Caspase-3
CI	Confidence interval
CP	Caudoputamen
CPM	Counts per million
CrP	Cribriform plate
dpi	Days post injection
DTA	Diphtheria toxin
E	Embryonic day
eGFP	Enhanced green fluorescent protein
EPL	External plexiform layer
EPSP	Excitatory postsynaptic potential
ESC	Embryonic stem cell
eYFP	Enhanced yellow fluorescent protein
FACS	Fluorescent-activated cell sorting
FLAG	FLAG-tag
GC	Granule cell
GCL	Granule cell layer

GL	Glomerular layer
GO-term	Gene ontology term
HA	HA-tag, human influenza hemagglutinin
hChR2	Humanized channelrhodopsin-2
Hipp	Hippocampus
hUbc	Human ubiquitin promoter
ICC	Immunocytochemistry
IHC	Immunohistochemistry
iPSC	Induced pluripotent stem cell
IPSP	Inhibitory postsynaptic potential
IRES	Internal ribosome entry site
KO	Bax knockout
KsO	Kusabira orange
L	Layer
MCL	Mitral cell layer
MCx	Motor cortex
ME	Module eigengene
MEF	Mouse embryonic fibroblast
MT	Mitral and tufted
MT-T	*Pchd21*-IRES-Cre x TeNT mouse line
MT-T KO	*Pchd21*-IRES-Cre, KO x TeNT, KO mouse line
OB	Olfactory bulb
OE	Olfactory epithelium

ONL	Olfactory nerve layer
OSN	Olfactory sensory neuron
P	Postnatal day
PC	Principal component
PCA	Principal component analysis
PCR	Polymerase chain reaction
PCx	Piriform cortex
PSC	Pluripotent stem cell
REF	Rat embryonic fibroblasts
RNA-Seq	RNA sequencing
SSCx	Somatosensory cortex
SVZ	Subventricular zone
TeNT	Tetanus toxin
TH	Tyrosine hydroxylase
WGCNA	Weighted gene co-expression network analysis
WT	Wild-type

LIST OF FIGURES

LIST OF TABLES

ACKNOWLEDGEMENTS

First, I must thank Kristin Baldwin for providing me the opportunity to conduct my PhD research in her lab and for her continuous creativity and support throughout the process. I would also like to thank both current and previous members of the Baldwin lab, the DNC, and the UCSD Neuroscience Graduate Program for their regular encouragement and discussion of my experiments. In particular, a huge shout out to Valentina Lo Sardo, Sohyon Lee, Rachel Tsunemoto, Loraine Campanati, and Swetha Murthy who all provided unwavering support and motivation both inside and outside the lab. Furthermore, I would like to thank Alysson Muotri, Brenda Bloodgood, Nicholas Spitzer, and Lisa Stowers for serving on my committee and providing invaluable scientific insight. I also need to acknowledge Kathy Spencer for her microscopy support, Brian Seegers and Matt Haynes of the TSRI Flow Cytometry Core for their assistance with FACS, John Shimashita in the TSRI Sequencing Core for conducting the RNA sequencing, and Denyse Huff and the veterinary staff of the vivarium for their assistance with the mice.

Chapter 2, in part, is a reprint of the material as it appears in James, K.N., Throesch, B.T., Davini, W., Eade, K.T., Ghosh, S., Lee, S., Torabi-Rander, N., and Baldwin K.K., 2017, Activity based checkpoints ensure circuit stability in the olfactory system, bioRxiv. K.N.J. was the primary investigator and author of this paper.

Chapter 3, in part, is currently being prepared for submission for publication of the material. Throesch, B.T., Wu, J., Castaneda, R.M., Hartzell, A., Sakurai, M., Rodriguez, A.R., Martin, G., Lippi, G., Osten, P., Kupriyanov, S., Belmonte, J.C.I., and Baldwin, K.K. The dissertation author was the primary investigator and author of this paper.

VITA

2009-2011	Undergraduate Researcher, University of Michigan, Ann Arbor
2011	Bachelor of Science, University of Michigan, Ann Arbor
2011-2013	Post baccalaureate IRTA Research Fellow, National Institutes of Health
2020	Doctor of Philosophy, University of California San Diego

PUBLICATIONS

Lai, J.-I., Nachun, D., Petrosyan, L., **Throesch, B.**, Campau, E., Gao, R., Baldwin, K.K., Coppola, G., Gottesfeld, J.M., and Soragni, E. (2019). Transcriptional profiling of isogenic Friedreich Ataxia neurons and effect of an HDAC inhibitor on disease signatures. Journal of Biological Chemistry 294(6): 1846–1859.

Wang, Y., Fehlhaber, K.E., Sarria, I., Cao, Y., Ingram, N.T., Guerrero-Given, D., **Throesch, B.**, Baldwin, K., Kamasawa, N., Ohtsuka, T., Sampath, A.P., and Martemyanov, K.A. (2017). The auxiliary calcium channel subunit α2β4 is required for axonal elaboration, synaptic transmission, and wiring of rod photoreceptors. Neuron 93(6): 1359–1374.

James, K.N., **Throesch, B.T.**, Davini, W., Eade, K.T., Ghosh, S., Lee, S., Torabi-Rander, N., and Baldwin K.K. (2017). Activity based checkpoints ensure circuit stability in the olfactory system. bioRxiv 156372.

Hall, A.M., **Throesch, B.T.**, Buckingham, S.C., Markwardt, S.J., Peng, Y., Wang, Q., Hoffman, D.A., and Roberson, E.D. (2015). Tau-dependent Kv4.2 depletion and dendritic hyperexcitability in a mouse model of Alzheimer's Disease. Journal of Neuroscience 35(15): 6221–6230.

Lin, L., Sun, W., **Throesch, B.**, Kung, F., Decoster, J.T., Berner, C.J., Cheney, R.E., Rudy, B., and Hoffman, D.A. (2013). DPP6 regulation of dendritic morphogenesis impacts hippocampal synaptic development. Nature Communications 4(2270): 1–12.

Moore, S.J., **Throesch, B.T.**, and Murphy, G.G. (2011). Of mice and intrinsic excitability: genetic background affects the size of the postburst afterhyperpolarization in CA1 pyramidal neurons. Journal of Neurophysiology 106(3): 1570–1580.

ABSTRACT OF THE DISSERTATION

Novel genetic strategies to probe mechanisms underlying neuronal development and circuit formation

by

Benjamin Taylor Throesch

Doctor of Philosophy in Neurosciences

University of California San Diego, 2020

Professor Kristin Baldwin, Chair
Professor Alysson Muotri, Co-chair

The brain is a complex organ that contains hundreds of diverse cellular subtypes which organize into unique regions and build intricate neural circuits. Neurons all transition through developmental stages where they must specify into cellular subtypes, migrate to appropriate brain regions, and extend axons to innervate postsynaptic targets as well as elaborate dendritic trees to receive incoming information. These stages are shaped by a balance of intracellular transcriptional programs and extracellular signals such as guidance molecules, adhesion proteins,

and neuronal activity. While an extensive list of factors contributing to these processes has been catalogued, the details remain unclear on how they converge within a cell to direct its development. Therefore, we developed novel genetic systems to decipher the rules that shape neuronal development and circuit formation. In one set of studies, we selectively blocked synaptic activity from a subset of neurons within the rodent olfactory bulb to investigate their role in shaping olfactory circuit development. We observed a dramatic impact on the maturation of newborn inhibitory neurons which could not be completely rescued by inhibiting cell death. By assessing the transcriptome of these developmentally-stalled neurons, we identified gene networks that regulate the maturation and integration of neurons into established circuits. For the second set of experiments, we injected rat stem cells into mouse blastocysts to generate rat-mouse brain chimeras and determine whether rat neurons are flexible to develop into, and contribute to foreign neural circuits. In brain-complemented chimeras, we observed diverse rat neuronal subtypes that adopt their host's developmental timeline and functionally integrate into the mouse brain. Furthermore, we identified species-specific barriers to rat complementation when these neurons are challenged to reconstitute degenerated mouse circuits. Together, these studies provide insights into the mechanisms governing neuronal integration into foreign and compromised neural circuits, which will inform efforts in regenerative medicine.

Introduction:

In 1888, the father of neuroscience Santiago Ramón y Cajal began publishing a series of histological studies detailing the complexities and intricacies of the vertebrate nervous system (Cajal, 1911). This work formulated the neuron doctrine, which placed the nerve cell as the structural and functional unit of the nervous system, and detailed the rich structural diversity of neurons and their appendages. Furthermore, his hypotheses on neuronal function, development, and degeneration continue to drive and shape investigations into the complex organ that is the brain.

Today, we estimate the human brain contains ~90 billion neurons with an equal proportion of non-neuronal cellular subtypes (Azevedo et al., 2009). Just as Cajal illustrated, these billions of neurons are a heterogeneous population constituting potentially hundreds of distinct subtypes and form functional synaptic connections that number in the hundreds of trillions in order to build precise neural circuits (Lake et al., 2016; Zeisel et al., 2018). This complexity is necessary to build an organ that is capable of interpreting, adapting to, and interacting with an equally complex world. Whereas the size and intricacy of an organism's nervous system scales with both their body size and behavioral repertoire, all neurons must go through similar, conserved mechanisms of development (DeFelipe, 2011). How is this accomplished?

Broadly speaking, neurons transition through three main developmental stages. First, they must determine a cell fate and specify into a unique neuronal subtype. Then, neurons migrate to the location appropriate for their chosen subtype within the organizing nervous system. Finally, neurons integrate into circuits by extending and elaborating axons and/or dendrites and innervating appropriate target cells in order to form functional connections. It is necessary to

point out these stages are not independent of one another, but rather occur simultaneously exponentially magnifying the complexity of this endeavor. Decades of research have informed us these stages are a balance of intrinsic, genetic programs and external, environmental signals that work in concert to regulate intracellular processes, which drive neuronal development and circuit formation. In this chapter, I will provide a brief overview of the rules and mechanisms that guide each of these stages. My intention is not to provide a comprehensive overview of every molecule and protein involved, but rather to highlight broad themes and rules governing these stages.

Specification

Neural precursors populating the ventricular zone must transition through a series of intermediate stages to ultimately arrive at a terminal fate characterized by unique electrophysiological and morphological properties, as well as the expression of subtype-specific receptors, adhesion molecules, and neurotransmitter machinery genes. These transitions are partially shaped by exogenous signaling cues. Transplantation studies in the early 1990s found early neuronal progenitors were capable of giving rise to region-specific neuronal subtypes even when those progenitors were placed in mismatched, heterotopic brain areas (Brüstle et al., 1995; Fishell, 1995; Renfranz et al., 1991; Vicario-Abejon et al., 1995). These studies argued that the intrinsic genetic programs within progenitors remain plastic such that exogenous cues drive the commitment of daughter cells to distinct neuronal fates (Edlund et al., 1999).

Follow-up studies though emphasized that precursors become increasingly fate-committed and lose that plasticity despite the same exogenous cues. Using similar methods, transplanted late-stage progenitors were either unable to contribute to heterotopic regions or generated pre-determined neuronal subtypes (Campbell et al., 1995; Desai et al., 2000; Frantz et

al., 1996; Margrassi et al., 1998; McConnell 1988; Yang et al., 2000). These studies countered that intrinsic genetic programs become increasingly autonomous and dominate the specification of neuronal subtypes after initial regional patterning.

Intrinsic genetic programs are controlled by a constellation of transcription factors that work in concert to regulate neuronal development. Targeted manipulation of gene expression has implicated a number of transcription factors necessary for neuronal fate determination. For example, Nr1 expression in the retina is crucial for specifying neurons into rods rather than cones, Tlx1 and Tlx3 drive the production of glutamatergic neurons in the dorsal spinal cord, and Lhx3 works alone to drive interneuron development or with Isl1 to specify motor neurons in the ventral spinal cord (Cheng et al., 2004; McIlvain et al., 2007; Mears et al., 2001; Pfaff et al., 1996; Sharma et al., 1998; Thaler et al., 2002). Within the cortex, the number of transcription factors implicated in neuronal specification is even larger (Molyneaux et al., 2007). These transcription factors can also repress certain lineages and thus limit the number of potential neuronal fate pathways for a progenitor to follow (Lee et al., 2019; Nakatani et al., 2007; Puelles et al., 2006). Therefore, transcription factors act to both push cells down certain trajectories as well as limit possible pathways.

Recent experiments using directed-differentiation also demonstrate the sufficiency of transcriptional networks to shape neuronal fate and specificity. The transcription factor Fezf2 is crucial for the terminal development of subcortical projection neurons (Chen et al., 2005; Molyneaux et al., 2005; Lodato et al., 2014). Deletion of the gene leads to a loss of subcortical projection neurons, whereas its overexpression promotes the excessive production of these neuronal subtypes. In fact, ectopic expression of Fezf2 in corticocortical projection neurons can alter their subtype specificity by redirecting their axonal projections to subcortical targets (Chen

et al., 2008). Furthermore, directed Fezf2 overexpression *in vivo* is capable of reprogramming the cell fate of striatal progenitors to produce subcortical projection-like neurons rather than medium spiny neurons, as well as alter the identity of post-mitotic layer 4 neurons (De la Rossa et al., 2013; Rouaux et al., 2010).

The same transcription factor directed-differentiation technique can also be successfully used on cell types other than neurons. Terminally-differentiated glia can be reprogrammed *in vitro* to functional neurons by overexpressing Pax6, Neurog2, Mash1, or Dlx2 (Berninger et al., 2007; Heinrich et al., 2012; Heins et al., 2002). This method has further been adopted to convert cells that do not belong to the neuronal lineage into a rapidly expanding list of neuronal subtypes (Blanchard et al., 2015; Tsunemoto et al., 2015; Tsunemoto et al., 2018; Vierbuchen et al., 2010). Together, these studies demonstrate the power transcriptional networks exercise over neuronal cell fate determination and diverse subtype specification.

Intrinsic genetic programs are necessary beyond the initial fate choice in order to transition to later stages of neuronal development and maintain their terminal subtype state. Transcription factors use feedforward mechanisms in order to drive specification forward as has been shown in *Drosophila* (Baumgardt et al., 2007; Baumgardt et al., 2009). This was bioinformatically visualized in mouse cortical neurons recently using an unbiased single-cell RNA sequencing approach. In these experiments, researchers were able to identify and temporally order sets of regulatory transcriptional networks into sequential waves based on their expression patterns (Telley et al., 2016). After neurons reach their fully differentiated states, terminal networks are then further required in order to actively maintain these identities (Eade et al., 2012; Hobert, 2008; Leyva-Díaz et al., 2019).

In summary, intrinsic genetic mechanisms are sufficient to drive neuronal subtype specification and in some cases, disrupt and re-orient neurons to a different cell fate trajectory. How do these terminal-stage transcription factors interact with other intracellular programs to generate neuronal subtype-specific morphologies, electrophysiological properties, and complex gene expression patterns? Reprogramming and directed-differentiation studies demonstrated the strength of transcriptional networks, but the generated neuronal subtypes are not identical to their endogenous counterparts. This may be because derived cells lack relevant environmental cues to complete their specification. As seen in earlier progenitor stages, extrinsic cues inform intracellular signaling pathways to work with transcriptional networks to direct fate determination. How many of the subtype-specific properties are autonomously driven by transcriptional networks rather than enhanced by contextual signals? Continued work is thus required to identify a complete list of fate-specifying transcription factors, dissect the interactions between these transcriptional networks and how they are maintained, and determine how they are shaped by the external environment.

Migration

In the mammalian forebrain, subtype-fated neurons begin their migration to appropriate neocortical regions as soon as they are born from progenitors in the ventricular zone. Their end target and mode of migration is pre-determined by their location within the ventricular zone (De Carlos et al., 1996; Lavdas et al., 1999; Rakic, 1972; Wichterle et al., 2001). Lineage tracing experiments of radiolabeled cells determined glutamatergic neurons are generated in the embryonic pallium and initially use radial migration to build cortical layers from the inside-out, whereas GABAergic neurons in the subpallium migrate tangentially to appropriate neocortical

areas (Ang Jr et al., 2003; Angevine Jr et al., 1961; Rakic, 1972; Tamamaki et al., 1997; Wichterle et al., 2001).

Radial migration is utilized in structures such as the cortex and cerebellum in order to organize neurons into discrete layers. Histological studies have identified radial glial cells in the ventricular zone that extend a process to the pial surface in order to act as a structural scaffold for migrating neurons (Cajal, 1911; Rakic, 1972). Time-lapse imaging of radially-migrating neurons have shown they rely on two modes of travel; 1) locomotion, where a cell climbs along the radial cell fiber, or 2) somal translocation, where the migrating neuron extends a neurite to the pial surface and drags the nucleus through the process (Nadaraja et al., 2001). Once radially-migrating neurons reach the correct layer, they detach from glia and move tangentially to spread throughout the layer (O'Rourke et al., 1992; Walsh et al., 1993). Alternatively, tangentially migrating GABAergic neurons move long-distances without a glial scaffold. Interestingly, radially-migrating projection neurons and tangentially-migrating GABAergic neurons born at the same time will localize to the same layers despite traveling different distances (Ayala et al., 2007). What mechanisms regulate these efforts?

Adhesive interactions play a fundamental role in shaping both radial and tangential migration. Interactions between migrating neurons and radial glia are mediated by membrane-bound adhesion proteins such as astrotactin, neuregulin, AMOG, and integrins (Anton et al., 1999; Antonicek et al., 1987; Edmondson et al., 1988; Rio et al., 1997). For example, blocking astrotactin on cerebellar granule neurons *in vitro* using antibodies or generating mutant knockout mice demonstrated neurons were less adhesive to glia, had slower rates of migration, and impacted the development of the cerebellum (Adams et al., 2002; Stitt et al., 1990). Tangentially migrating neurons interact with the components of the extracellular matrix as well as other

migrating neurons to direct their movements. Neuronal-neuronal homotypic interactions can be attractive and support migration, as evidenced by NCAM1-dependent chain migration of neuroblasts into the olfactory bulb (Hu et al., 1996; Tomasiewicz et al., 1993; Wichterle et al. 1997). Homotypic interactions can alternatively be inhibitory in order to encourage neurons with matching subtypes to spread tangentially within a layer, as is seen with Cajal-Retzius cells (Borrell et al., 2006). Heterotopic interactions between neurons and the extracellular matrix, including axonal fibers and blood vessels, can also guide migrating neurons to their targets (Bovetti et al., 2007; Wray, 2002). Together, these adhesive mechanisms mainly act to guide migrating neurons to the correct location, as well as encourage their spread and equal coverage of target regions.

Soluble guidance molecules build gradients in the extracellular matrix to act as either chemoattractants or repellents over both long and short distances. A classic example of this is reelin, which was identified by a spontaneous recessive mutation in a mouse line named *reeler* due to its pronounced ataxia phenotype (Falconer, 1951). In *reeler* mice, the architecture of the cerebral cortex is flipped such that the older generations of neurons are located near the pial surface rather than in deeper cortical layers (Caviness Jr et al., 1973; Caviness Jr 1982). Upon isolation of the secreted glycoprotein reelin, studies identified the VLDLR and ApoER2 receptors on migrating neurons which regulate their attractive response to reelin (D'Arcangelo et al., 1995; D'Arcangelo et al., 1999; Hiesberger et al., 1999). Since the discovery of reelin, a host of other guidance molecules including Slit, Netrin1, semaphorin 3A and 3E, the Wnt family of proteins, and Neuregulin-1 have been implicated in playing subtype-specific chemoattractant and repellent roles of neuronal migration as well as axonal guidance (Ayala et al., 2007). Together these attractant molecules play a similar role as adhesive cues do in migration, whereas

chemorepellents are thought to restrict certain migrating subtypes from entering incorrect brain regions. The individual response of a migrating neuron to these and adhesive cues is dependent on its subtype, which controls the selective expression of receptors and intracellular signaling cascades that mediate the neurons specific actions.

In order to physically relocate, migrating neurons go through three standard steps: 1) they extend a leading neurite; 2) nuclear translocation draws the nucleus closer to the tip of the leading neurite; and 3) the trailing process is retracted (Ayala et al., 2007). These movements are a coordinated effort of actin and microtubules of the cellular cytoskeleton. Experiments destabilizing actin filaments with the compound cytochalasin B, were sufficient to inhibit the migration of cerebellar granule neurons *in vitro* (Rivas et al., 1995). Furthermore, live imaging has implicated the actin component of the cytoskeleton in coordinating nuclear translocation during migration as well as regulating growth cone extension (Martini et al., 2010; Solecki et al., 2009; Tian et al., 2015). Alternatively, microtubules and associated proteins focus on stabilizing the growing neurite structure (Ayala et al., 2007; Ka et al., 2014; Schaar et al., 2005). While actin, microtubules, and especially their associated proteins, kinases, and GTPases are clearly necessary for regulating neuronal migration, the mechanisms by which these proteins are regulated and coordinate with one another remain unclear.

In summary, neuronal migration relies heavily on extracellular guidance and adhesion molecules to activate intracellular programs that regulate, rearrange, and stabilize cytoskeletal dynamics. Attractive and repulsive forces work together to lure migrating neurons to the correct region and create a heterogeneous mixture within designated regional layers. The complete repertoire of these guidance molecules, growth factors, and adhesion proteins is by no means completely understood, especially as interest in the roles non-neuronal cells play in regulating

brain development grows. In addition, the intracellular protein networks linking these extracellular cues to the cytoskeleton and regulating their dynamics remain active areas for investigation. Intersecting these networks with programs that specify neuronal fate will also yield important insights into intrinsic mechanisms regulating neuronal migration.

Integration

Once neurons migrate to the correct location, they begin to extend axons and then elaborate dendritic trees in order to innervate appropriate target regions. Growing neurites continuously survey their local environment to interpret signals and determine whether to elongate or pause their growth, to initiate or repress new collateral branches, as well as to stimulate or inhibit the elaboration of terminal branches. In some cases, such as for glutamatergic projection neurons, they may extend axonal projections to distant regions, whereas local GABAergic inhibitory neurons restrict their axonal branches to local circuits. Within the central nervous system, neurons also build highly diverse, complex branched dendritic trees within their local region in search of axons with which to form synaptic structures. Once again, these processes are a balance of extrinsic cues and subtype-specific intrinsic programs governing targeting and branching patterns.

The same extracellular signaling molecules and adhesion proteins that regulate neuronal migration also drive the initial formation and structure of axonal projections and dendritic trees (Kalil et al., 2014). Studies using dissociated cells or cortical explants have demonstrated secreted signaling molecules, such as Netrin1, attract cortical axons and can stimulate local branches in order to promote axonal and dendritic elaboration, while Sema3A inversely causes cortical axonal branches to retract yet dendrites to grow (Calderon de Anda et al., 2012; Dent et

al., 2004; Fenstermaker et al., 2004; Métin et al., 2017; Polleux et al., 1998; Richards et al., 2017; Serafina et al., 2016). Establishing concentration gradients for these competing forces *in vivo* is essential for guiding subtype-specific neurites away from undesired locations and attracting them to elaborate within the correct region in order to build functional layered structures such as the topographic maps seen in visual system (Luo et al., 2007). Furthermore, soluble neurotrophic growth factors such as FGF, NGF, and BDNF, as well as morphogens like the Wnt family of proteins act to evoke neurite branching by regulating various components of the cytoskeletal machinery (Danzer et al., 2002; Gallo et al., 1998; Hall et al., 2000; Jeanneteau et al., 2010; Szebenyi et al., 2001). Together, these molecules drive growing neurites to target regions where they will meet their future synaptic partners.

Contact-mediated mechanisms acting through cell adhesion molecules also shape axon and dendrite morphogenesis. In the case of dendritic development, the 22 γ-protocadherins are expressed throughout the central nervous system as tetramers that could specify into more than 100,000 unique combinations (Schreiner et al., 2010). Through homophilic interactions in *trans*, neurons use a unique combinatorial expression of γ-protocadherins in order to avoid their own processes (self-avoidance) and interact with the processes from other neurons (Garrett et al., 2012; Molumby et al., 2016; Molumby et al., 2017; Thu et al., 2014). Another family of adhesion proteins, DSCAMs, was identified as an axon guidance receptor that regulates dendrite self-avoidance in *Drosophila*, and has also been shown to shape arborization and tiling in the mouse retina (Fuerst et al., 2008; Hughes et al., 2007; Matthews et al., 2007; Schmucker et al., 2000; Soba et al., 2007). Both γ-protocadherins and DSCAMs ensure dendrites fully cover their regional territory to maximize synaptic contacts with innervating axon terminals.

In some instances transcription factors have been demonstrated to directly alter axonal projections or dendritic branching patterns (Santiago et al., 2014). As described earlier, overexpression of Fezf2 in cortical projection neurons is capable of redirecting their axonal projections after they have already been established (Chen et al., 2008). Furthermore, overexpression of diverse transcription factor pairs in mouse embryonic fibroblasts is sufficient to generate neurons *in vitro* with unique morphologies, including the characteristic pseudo-unipolar morphology of peripheral sensory neurons (Blanchard et al., 2015; Tsunemoto et al., 2018). These transcription factors must indirectly regulate the cytoskeletal machinery, as has been demonstrated by the regulation of axon growth by the transcription factor Srf and dendritic branching by Cux1 (Li et al., 2010; Stern et al., 2013). Yet, the intracellular networks that give rise to these unique morphologies in the absence of the complex *in vivo* extracellular signaling molecule environment remain unclear. Continued efforts in this field to expand the list of transcriptional regulators shaping neuronal morphology, including those activated by neuronal activity and calcium signals, are necessary for further insight.

The final component driving axonal targeting and dendritic development, as well as migration and specification, is calcium signaling. Calcium transients in developing neurites activate important second messenger systems, which in turn regulate downstream gene expression (Rosenberg et al., 2011; West et al., 2001). Spontaneous calcium waves mediated by internal stores and voltage-gated calcium channels are seen in developing cortical and xenopus spinal neuron growth cones (Gomez et al., 1999; Gu et al., 1994; Tang et al., 2003). Interestingly, these transients are correlated with periods of axon pausing and retraction, whereas blocking them stimulates axonal outgrowth. Calcium waves can also be simulated to drive late stage programs of neuronal maturation and specification such as neurotransmitter expression and

channel maturation (Gu et al., 1995). Furthermore, live imaging experiments in xenopus tectal neurons demonstrated calcium signals driven by glutamate signaling through NMDA receptors are necessary for the initial development of the dendritic arbor (Rajan et al., 1998).

The initial phases of neurite growth and branching may not be dependent on neuronal activity though. A key study blocked neurotransmitter release from the entire brain of developing mouse embryos and observed neuronal migration and circuit formation remained intact (Verhage et al., 2000). These findings indicate intrinsic mechanisms and guidance/adhesion cues were sufficient to grossly pattern the nervous system. In later stages of development though, circuits atrophy as a result of large waves of cell death suggesting activity is crucial for the survival and maintenance of neuronal circuits. This is consistent with a wealth of experimental evidence in sensory systems assessing the crucial role neuronal activity plays in sculpting and refining both axonal terminals and dendritic branches (Shatz et al., 1988; Sretavan et al., 1988; Moore et al., 1985; Antón-Bolaños et al., 2019). After circuits are largely formed, neuronal activity continues to play a dominant role in refining neuronal morphology at the subcellular level (Carulli et al., 2011, Pan et al., 2020). Therefore, regardless of whether neuronal activity is necessary for the initial stages of neuronal circuit formation, it unarguably shapes neuronal specificity, morphology, and plasticity throughout a neuron's lifetime.

To summarize, at early stages of neuronal specification, intrinsic genetic mechanisms dominate developmental programs. But as neurons transition into later stages of migration, integration and synapse formation, extrinsic cues play an increasing role in shaping neuronal development. Intracellular transcriptional networks always remain active in order to maintain terminal-differentiation programs, but they evolve as the neuron matures to take into account aspects of dendritic branching pattern, axonal morphology, regional and laminar location, as well

as the expression of terminal-stage synaptic machinery and ion channels. Furthermore, they are instructed by neuronal activity, adhesion molecules, and growth factors throughout an organism's lifetime to incorporate experience-dependent changes and refinements. Much work remains to decipher the list of both intracellular and extracellular cues, but further experiments will likely aim to identify terminal-stage programs as well as the path neurons take to arrive in these reinforced stages. Further work also will test the plasticity of these specifications, as neurons have been demonstrated to change key aspects of their identity, such as neurotransmitter expression (Dulcis, et al., 2013). Finally, the complex interactions between all these regulators, both intrinsic and extrinsic, are necessary in order to grasp the complete story of neuronal development.

Building a comprehensive understanding of the molecular logic driving neuronal development and circuit formation is not only important from a basic biology perspective, but also for understanding neurodevelopmental and neurodegenerative disorders. A goal of regenerative medicine is to functionally reconstitute lost populations of cells underlying disease. Whereas other organs in the body such as the heart, kidneys, and pancreas can be wholly replaced with healthy donor organs, this does not work for the brain. Rather, efforts for neurodegenerative disorders may rely on the successful transplantation and integration of healthy, donor neurons or stem cells into impacted circuits. Thus, not only understanding the basic mechanisms driving neuronal development and integration, but also how these change beyond the initial stages of circuit formation and are conserved between foreign contexts is critical for success in neuroregenerative medicine. To this end, I will describe in the following chapters our efforts to understand the rules regulating the integration of neurons into adult and foreign neuronal circuits by developing novel genetic systems.

References:

Adams, N.C., Tomoda, T., Cooper, M., Dietz, G., and Hatten, M.E. (2002). Mice that lack astrotactin have slowed neuronal migration. Development 129(4): 965–972.

Ang Jr., E.S.B.C., Haydar, T.F., Gluncic, V., and Rakic, P. (2003). Four-dimensional migratory coordinates of GABAergic interneurons in the developing mouse cortex. Journal of Neuroscience 23(13): 5805–5815.

Angevine Jr, J.B., and Sidman, R.L. (1961). Autoradiographic study of cell migration during histogenesis of cerebral cortex in the mouse. Nature 192: 766–768.

Anton, E.S., Kreidberg, J.A., and Rakic, P. (1999). Distinct functions of α3 and αV integrin receptors in neuronal migration and laminar organization of the cerebral cortex. Neuron 22(2): 277–289.

Antón-Bolaños, N., Sempere-Ferràndez, A., Guillamón-Vivancos, T., Martini, F.J., Pérez-Saiz, L., Gezelius, H., Filipchuk, A., Valdeolmillos, M., and López-Bendito, G. (2019). Prenatal activity from thalamic neurons governs the emergence of functional cortical maps in mice. Science 364(6444), 987–990.

Antonicek, H., Persohn, E., and Schachner, M. (1987). Biochemical and functional characterization of a novel neuron-glia adhesion molecule that is involved in neuronal migration. Journal of Cell Biology 104(6): 1587–1595.

Ayala, R., Shu, T., and Tsai, L.H. (2007). Trekking across the brain: the journey of neuronal migration. Cell 128(1): 29–43.

Azevedo, F.A.C., Carvalho, L.R.B., Grinberg, L.T., Farfel, J.M., Ferretti, R.E.L., Leite, R.E.P., Filho, W.J., Lent, R., and Herculano-Houzel, S. (2009). Equal numbers of neuronal and nonneuronal cells make the human brain an isometrically scaled-up primate brain. Journal of Comparative Neurology 513(5): 532–541.

Baumgardt, M., Karlsson, D., Terriente, J., Díaz-Benjumea, F.J., and Thor, S. (2009). Neuronal subtype specification within a lineage by opposing feed-forward loops. Cell 139(5): 969–982.

Baumgardt, M., Miguel-Aliaga, I., Karlsson, D., Ekman, H., and Thor, S. (2007). Specification of neuronal identities by feedforward combinatorial coding. PLoS Biology 5(2): e37.

Blanchard, J.W., Eade, K.T., Szũcs, A., Lo Sardo, V., Tsunemoto, R.K., Williams, D., Sanna, P.P., and Baldwin, K.K. (2015). Selective conversion of fibroblasts into peripheral sensory neurons. Nature Neuroscience 18(1): 25–35.

Berninger, B., Costa, M.R., Koch, U., Schroeder, T., Sutor, B., Grothe, B., and Götz, M. (2007). Functional properties of neurons derived from *in vitro* reprogrammed postnatal astroglia. Journal of Neuroscience 27(32): 8654–8664.

Borrell, V., and Marín, O. (2006). Meninges control tangential migration of hem-derived Cajal-Retzius cells via CXCL12/CXCR4 signaling. Nature Neuroscience 9(10): 1284–1293.

Bovetti, S., Hsieh, Y.C., Bovolin, P., Perroteau, I., Kazunori, T., and Puche, A.C. (2007). Blood vessels form a scaffold for neuroblast migration in the adult olfactory bulb. Journal of Neuroscience 27(22): 5976–5980.

Brüstle, O., Maskos, U., and McKay, R.D.G. (1995). Host-guided migration allows targeted introduction of neurons into the embryonic brain. Neuron 15(6): 1275–1285.

Calderon de Anda, F., Rosario, A.L., Durak, O., Tran, T., Gräff, J., Meletis, K., Rei, D., Soda, T., Madabhushi, R., Ginty, D., Kolodkin, A.L., and Tsai, L.H. (2012). Autism spectrum disorder susceptibility gene TAOK2 affects basal dendrite formation in the neocortex. Nature Neuroscience 15(7): 1022–1031.

Campbell, K., Olsson, M., and Björklund, A. (1995). Regional incorporation and site-specific differentiation of striatal precursors transplanted to the embryonic forebrain ventricle. Neuron 15(6): 1259–1273.

Carulli, D., Foscarin, S., and Rossi, F. (2011). Activity-dependent plasticity and gene expression modifications in the adult CNS. Frontiers in Molecular Neuroscience 4: 50.

Caviness Jr, V.R. (1982). Neocortical histogenesis in normal and reeler mice: a developmental study based upon [3H]thymidine autoradiography. Brain Research 256(3): 293–302.

Caviness Jr, V.R., and Sidman, R.L. (1973). Time of origin or corresponding cell classes in the cerebral cortex of normal and reeler mutant mice: an autoradiographic analysis. Journal of Comparative Neurology 148(2): 141–151.

Chen, B., Schaevitz, L.R., and McConnell, S.K. (2005). Fezl regulates the differentiation and axon targeting of layer 5 subcortical projection neurons in cerebral cortex. PNAS 102(47): 17184–17189.

Chen, B., Wang, S.S., Hattox, A.M., Rayburn, H., Nelson, S.B., and McConnell, S.K. (2008). The Fezf2-Ctip2 genetic pathway regulates the fate choice of subcortical projection neurons in the developing cerebral cortex. PNAS 105(32): 11382–11387.

Cheng, L., Arata, A., Mizuguchi, R., Qian, Y., Karunaratne, A., Gray, P.A., Arata, S., Shirasawa, S., Bouchard, M., Luo, P., Chen, C.-L., Busslinger, M., Goulding, M., Onimaru, H., and Ma, Q. (2004). Tlx3 and Tlx1 are post-mitotic selector genes determining glutamatergic over GABAergic cell fates. Nature Neuroscience 7(5): 510–517.

Danzer, S.C., Crooks, K.R.C., Lo, D.C., and McNamara, J.O. (2002). Increased expression of brain-derived neurotrophic factor induces formation of basal dendrites and axonal branching in

dentate granule cells in hippocampal explant cultures. Journal of Neuroscience 22(22): 9754–9763.

D'Arcangelo, G., Miao, G.G>, Chen, S.C., Soares, H.D., Morgan, J.I., and Curran, T. (1995). A protein related to extracellular matrix proteins deleted in the mouse mutant reeler. Nature 374(6524): 719–723.

D'Arcangelo, G., Homayouni, R., Keshvara, L., Rice, D.S., Sheldon, M., and Curran, T. (1999). Reelin is a ligand for lipoprotein receptors. Neuron 24(2): 471–479.

De Carlos, J.A., López-Mascaraque, L., and Valverde, F. (1996). Dynamics of cell migration from the lateral ganglionic eminence in the rat. Journal of Neuroscience 16(19): 6146–6156.

DeFelipe, J. (2011). The evolution of the brain, the human nature of cortical circuits, and intellectual creativity. Frontiers in Neuroanatomy 5: 29.

De la Rossa, A., Bellone, C., Golding, B., Vitali, I., Moss, J., Toni, N., Lüscher, C., and Jabaudon, D. (2013). In vivo reprogramming of circuit connectivity in postmitotic neocortical neurons. Nature Neuroscience 16(2): 193–200.

Dent, E.W., Barnes, A.M., Tang, F., and Kalil, K. (2004). Netrin-1 and Semaphorin 3A promote or inhibit cortical axon branching, respectively, by reorganization of the cytoskeleton. Journal of Neuroscience 24(12): 3002–3012.

Desai, A.R., and McConnell, S.K. (2000). Progressive restriction in fate potential by neural progenitors during cerebral cortical development. Development 127(13): 2863–2872.
Dulcis, D., Jamshidi, P., Leutgeb, S., and Spitzer, N.C. (2013). Neurotransmitter switching in the adult brain regulates behavior. Science 340(6131): 449–453.

Eade, K.T., Fancher, H.A., Ridyard, M.S., and Allan, D.W. (2012). Developmental transcriptional networks are required to maintain neuronal subtype identity in the mature nervous system. PLoS Genetics 8(2): e1002501.

Edlund, T., and Jessell, T.M. (1999). Progression from extrinsic to intrinsic signaling in cell fate specification: a view from the nervous system. Cell 96(2): 211–224.

Falconer, D.S. (1951). Two new mutants, "trembler" and "reeler", with neurological actions in the house mouse (Mus musculus L.). Journal of Genetics 50(2): 192–205.

Fenstermaker, V., Chen, Y., Ghosh, A., and Yuste, R. (2004). Regulation of dendritic length and branching by Semaphorin 3A. Journal of Neurobiology 58(3): 403–412.

Fishell, F. (1995). Striatal precursors adopt cortical identities in response to local cues. Development 121: 803–812.

Frantz, G.D., and McConnell, S.K. (1996). Restriction of late cerebral cortical progenitors to an upper-layer fate. Neuron 17(1): 55–61.

Friedmann-Morvinski, D., Bushong, E.A., Ke, E., Soda, Y., Marumoto, T., Singer, O., Ellisman, M.H., and Verma, I.M. (2013). Dedifferentiation of neurons and astrocytes by oncogenes can induce gliomas in mice. Science 338(6110): 1080–1084.

Fuerst, P.G., Koizumi, A., Masland, R.H., and Burgess, R.W. (2008). Neurite arborization and mosaic spacing in the mouse retina require DSCAM. Nature 451(7177): 470–474.

Gallo, G., and Letourneau, P.C. (1998). Localized sources of neurotrophins initiate axon collateral sprouting. Journal of Neuroscience 18(14): 5403–5414.

Garrett, A.M., Schreiner, D., Lobas, M.A., and Weiner, J.A. (2012). γ-Protocadherins control dendrite arborization by regulating activity of a FAK/PKC/MARCKS signaling pathway. Neuron 74(2): 269–276.

Gomez, T.M., and Spitzer, N.C. (1999). In vivo regulation of axon extension and pathfinding by growth-cone calcium transients. Nature 397(6717): 350–355.

Gu, X., Olson, E.C., and Spitzer, N.C. (1994). Spontaneous neuronal calcium spikes and waves during early differentiation. Journal of Neuroscience 14(11): 6325–6335.

Gu, X., and Spitzer, N.C. (1995). Distinct aspects of neuronal differentiation encoded by frequency of spontaneous Ca2+ transients. Nature 375(6534): 784–787.

Hall, A.C., Lucas, F.R., and Salinas, P.C. (2000). Axonal remodeling and synaptic differentiation in the cerebellum is regulated by Wnt-7a signaling. Cell 100(5): 525–535.

Heinrich, C., Götz, M., and Berninger, B. (2012). Reprogramming of postnatal astroglia of the mouse neocortex into functional, synapse-forming neurons. Methods in Molecular Biology 814: 485–498.

Heins, N., Malatesta, P., Cecconi, F., Nakafuku, M., Tucker, K.L., Hack, M.A., Chapouton, P., Barde, Y.-A., and Götz, M. (2002). Glial cells generate neurons: the role of the transcription factor Pax6. Nature Neuroscience 5(4): 308–315.

Hiesberger, T., Trommsdorff, M., Howell, B.W., Goffinet, A., Mumby, M.C., Cooper, J.A., and Herz, J. (1999). Direct binding of Reeling to VLDL receptor and ApoE receptor 2 induces tyrosine phosphorylation of disabled-1 and modulates tau phosphorylation. Neuron 24(2): 481–489.

Hobert, O. (2008). Regulatory logic of neuronal diversity: terminal selector genes and selector motifs. PNAS 105(51): 20067–20071.

Hu, H., Tomasiewicz, H., Magnuson, T., and Rutishauser, U. (1996). The role of polysialic acid in migration of olfactory bulb interneuron precursors in the subventricular zone. Neuron 16(4): 735–743.

Hughes, M.E., Bortnick, R., Tsubouchi, A., Bäumer, P., Kondo, M., Uemura, T., and Schmucker, D. (2007). Homophilic Dscam interactions control complex dendrite morphogenesis. Neuron 54(3): 417–427.

Jeanneteau, F., Deinhardt, K., Miyoshi, G., Bennett, A.M., and Chao, M.V. (2010). The MAP kinase phosphatase MKP-1 regulates BDNF-induced axon branching. Nature Neuroscience 13(11): 1373–1379.

Ka, M., Jung, E.M., Mueller, U. and Kim, W.Y. (2014). MACF1 regulates the migration of pyramidal neurons via microtubule dynamics and GSK-3 signaling. Developmental Biology 395 (1): 4–18.

Lake, B.B., Ai, R., Kaeser, G.E., Salathia, N.S., Yung, Y.C., Liu, R., Wildberg, A., Gao, D., Fung, H.L., Chen, S., Vijayaraghavan, R., WOng, J., Chen, A., Sheng, X., Kaper, F., Shen, R., Ronaghi, M., Fan, J.B., Wang, W., Chun, J., and Zhang, K. (2016). Neuronal subtypes and diversity revealed by single-nucleus RNA sequencing of the human brain. Science 352(6293): 1586–1590.

Lavdas, A.A., Grigoriou, M., Pachnis, V., and Parnavelas, J.G. (1999). The medial ganglionic eminence gives rise to a population of early neurons in the developing cerebral cortex. Journal of Neuroscience 19(18): 7881–78888.

Lee, J., Taylor, C.A., Barnes, K.M., Shen, A., Stewart, E.V., Chen, A., Xiang, Y.K., Bao, Z., and Shen, K. (2019). A Myt1 family transcription factor defines neuronal fate by repressing non-neuronal genes. eLife 8: e46703.

Leyva-Díaz, E., and Hobert, O. (2019). Transcription factor autoregulation is required for acquisition and maintenance of neuronal identity. Development 146(13): dev177378.

Li, N., Zhao, C.T., Wang, Y., and Yuan, X.B. (2010). The transcription factor Cux1 regulates dendritic morphology of cortical pyramidal neurons. PLoS One 5(5): e10596.

Lodato, S., Molyneaux, B.J., Zuccaro, E., Goff, L.A., Chen, H.H., Yuan, W., Meleski, A., Takahashi, E., Mahony, S., Rinn, J.L., Gifford, D.K., and Arlotta, P. (2014). Gene co-regulation by Fezf2 selects neurotransmitter identity and connectivity of corticospinal neurons. Nature Neuroscience 17(8): 1046–1054.

Luo, L., and Flanagan, J.G. (2007). Development of continuous and discrete neural maps. Neuron 56(2): 284–300.

Magrassi, L., Ehrlich, M.E., Butti, F., Pezzotta, S., Govoni, S., and Cattaneo, E. (1998). Basal ganglia precursors found in aggregates following embryonic transplantation adopt a striatal phenotype in heterotopic locations. Development 125(15): 2847–2855.

Martini, F.J., and Valdeolmillos, M. (2010). Actomyosin contraction at the cell rear drives nuclear translocation in migrating cortical interneurons. Journal of Neuroscience 30(25): 8660–8670.

Matthews, B.J., Kim, M.E., Flanagan, J.J., Hattori, D., Clemens, J.C., Zipursky, S.L., and Grueber, W.B. (2007). Dendrite self-avoidance is controlled by *Dscam*. Cell 129(3): 593–604.

McConnell, S.K. (1988). Fates of visual cortical neurons in the ferret after isochronic and heterochronic transplantation. Journal of Neuroscience 8(3): 945–950.

McIlvain, V.A., and Knox, B.E. (2007). Nr2e3 and Nrl can reprogram retinal precursors to the rod fate in xenopus retina. Developmental Dynamics 236(7): 1970–1979.

Mears, A.J., Kondo, M., Swain, P.K., Takada, Y., Bush, R.A., Saunders, T.L., Sieving, P.A., and Swaroop, A. (2001). Nrl is required for rod photoreceptor development. Nature Genetics 29(4): 447–452.

Métin, C., Deléglise, D., Serafini, T., Kennedy, T.E., Tessier-Lavigne, M. (1997). A role for netrin-1 in the guidance of cortical efferents. Development 124(24): 5063–5074.

Molumby, M.J., Anderson, R.M., Newbold, D.J., Koblesky, N.K., Garrett, A.M., Schreiner, D., Radley, J.J., and Weiner, J.A. (2017). γ-Protocadherins interact with neuroligin-1 and negatively regulate dendritic spine morphogenesis. Cell Reports 18(11): 2702–2714.

Molumby, M.J., Keeler, A.B., and Weiner, J.A. (2016). Homophilic protocadherin cell-cell interactions promote dendrite complexity. Cell Reports 15(5): 1037–1050.

Molyneaux, B.J., Arlotta, P., Hirata, T., Hibi, M., and Macklis, J.D. (2005). Fezl is required for the birth and specification of corticospinal motor neurons. Neuron 47(6): 817–831.

Moore, D.R., and Kitzes, L.M. (1985). Projections from the cochlear nucleus to the inferior colliculus in normal and neonatally cochlea-ablated gerbils. Journal of Comparative Neurology 240(2): 180–195.

Nadarajah, B., Brunstrom, J.E., Grutzendler, J., Wong, R.O.L., and Pearlman, A.L. (2001). Two modes of radial migration in early development of the cerebral cortex. Nature Neuroscience 4(2): 143–50.

Molyneaux, B.J., Arlotta, P., Menezes, J.R.L., and Macklis, J.D. (2007). Neuronal subtype specification in the cerebral cortex. Nature Reviews Neuroscience 8(6): 427–437.

Nakatani, T., Minaki, Y., Kumai, M., and Ono, Y. (2007). Helt determines GABAergic over glutamatergic neuronal fate by repressing Ngn genes in the developing mesencephalon. Development 134(15): 2783–2793.

O'Rourke, N.A., Dailey, M.E., Smith, S.J., and McConnell, S.K. (1992). Diverse migratory pathways in the developing cerebral cortex. Science 258(5080): 299–302.

Pan, Y., and Monje, M. (2020). Activity shapes neural circuit form and function: a historical perspective. Journal of Neuroscience 40(5): 944–954.

Pfaff, S.L., Mendelsohn, M., Stewart, C.L., Edlund, T., and Jessel, T.M. (1996). Requirement for LIM homeobox gene *Isl1* in motor neuron generation reveals a motor neuron-dependent step in interneuron differentiation. Cell 84(2): 309–320.

Polleux, F., Giger, R.J., Ginty, D.D., Kolodkin, A.L., and Ghosh, A. (1998). Patterning of cortical efferent projections by semaphorin-neuropilin interactions. Science 282(5395): 1904–1906.

Puelles, E., Acampora, D., Gogoi, R., Tuorto, F., Papalia, A., Guillemot, F., Ang, S.-L., and Simeone, A. (2006). Otx2 controls identity and fate of glutamatergic progenitors of the thalamus by repressing GABAergic differentiation. Journal of Neuroscience 26(22): 5955–5964.

Rajan, I., and Cline, H.T. (1998). Glutamate receptor activity is required for normal development of tectal cell dendrites in vivo. Journal of Neuroscience 18(19): 7836–7846.

Rakic, P. (1972). Mode of cell migration to the superficial layers of fetal monkey neocortex. Journal of Comparative Neurology. 145(1): 61–83.

Ramón y Cajal, S. (1911). Histology of the nervous system of man and vertebrates. Oxford, UK, Oxford University Press.

Renfranz, P.J., Cunningham, M.G., and McKay, R.D. (1991). Region-specific differentiation of the hippocampal stem cell line HiB5 upon implantation into the developing mammalian brain. Cell 66(4): 713–729.

Richards, L.J., Koester, S.E., Tuttle, R., and O'Leary, D.D. (1997). Directed growth of early cortical axons is influenced by a chemoattractant released from an intermediate target. Journal of Neuroscience 17(7): 2245–2458.

Rio, C., Rieff, H.L., Qi, P., and Corfas, G. (1997). Neuregulin and erbB receptors play a critical role in neuronal migration. Neuron 19(1): 39–50.

Rivas, R.J., and Hatten, M.E. (1995). Motility and cytoskeletal organization of migrating cerebellar granule neurons. Journal of Neuroscience 15(2): 981–989.

Rosenberg, S.S., and Spitzer, N.C. (2011). Calcium signaling in neuronal development. Cold Spring Harbor Perspectives in Biology 3(10): a004259.

Rouaux, C., and Arlotta, P. (2010). Fezf2 directs the differentiation of corticofugal neurons from striatal progenitors *in vivo*. Nature Neuroscience 13(11): 1345–1347.

Santiago, C., and Bashaw, G.J. (2014). Transcription factors and effectors that regulate neuronal morphology. Development 141(24): 4667–4680.

Shatz, C.J., and Stryker, M.P. (1988). Prenatal tetrodotoxin infusion blocks segregation of retinogeniculate afferents. Science 242(4875): 87–89.

Schmucker, D., Clemens, J.C., Shu, H., Worby, C.A., Xiao, J., Muda, M., Dixon, J.E., and Zipursky, S.L. (2000). Drosophila Dscam is an axon guidance receptor exhibiting extraordinary molecular diversity. Cell 101(6): 671–684.

Schreiner, D., and Weiner, J.A. (2010). Combinatorial homophilic interaction between gamma-protocadherin multimers greatly expands the molecular diversity of cell adhesion. PNAS 107(33): 14893–14898.

Serafini, T., Colamarino, S.A., Leonardo, E.D., Wang, H., Beddington, R., Skarnes, W.C., and Tessier-Lavigne, M. (1996). Netrin-1 is required for commissural axon guidance in the developing vertebrate nervous system. Cell 87(6): 1001–1014.

Sharma, K., Sheng, H.Z., Lettieri, K., Li, H., Karavanov, A., Potter, S., Westphal, H. and Pfaff, S.L. (1998). LIM homeodomain factors Lhx3 and Lhx4 assign subtype identities for motor neurons. Cell 95(6): 817–828.

Soba, P., Zhu, S., Emoto, K., Younger, S., Yang, S.J., Yu, H.H., Lee, T., Jan, L.Y., and Jan, Y.N. (2007). *Drosophila* sensory neurons require Dscam for dendritic self-avoidance and proper dendritic field organization. Neuron 54(3): 403–416.

Solecki, D.J., Trivedi, N., Govek, E.E., Kerekes, R.A., Gleason, S.S., and Hatten, M.E. (2009). Myosin II motors and F-actin dynamics drive the coordinated movement of the centrosome and soma during CNS glial-guided neuronal migration. Neuron 63(1): 63–80.

Southall, T.D., Davidson, C.M., Miller, C., Carr, A., and Brand, A.H. (2014). Dedifferentiation of neurons precedes tumor formation in *lola* mutants. Developmental Cell 28(6): 685–696.

Sretavan, D.W., Shatz, C.J., and Stryker, M.P. (1988). Modification of retinal ganglion cell axon morphology by prenatal infusion of tetrodotoxin. Nature 336(6198): 468–471.

Stern, S., Haverkamp, S., Sinske, D., Tedeschi, A., Naumann, U., Di Giovanni, S., Kochanek, S., Nordheim, A., and Knöll, B. (2013). The transcription factor serum response factor stimulates axon regeneration through cytoplasmic localization and cofilin interaction. Journal of Neuroscience 33(48): 18836–18848.

Stitt, T.N., and Hatten, M.E. (1990). Antibodies that recognize astrotactin block granule neuron binding to astroglia. Neuron 5(5): 639–649.

Szebenyi, G., Dent, E.W., Callaway, J.L., Seys, C., Lueth, H., and Kalil, K. (2001). Fibroblast growth factor-2 promotes axon branching of cortical neurons by influencing morphology and behavior of the primary growth cone. Journal of Neuroscience 21(11): 3932–3941.

Tamamaki, N., Fujimori, K.E., and Takuji, R. (1997). Origin and route of tangentially migrating neurons in the developing neocortical intermediate zone. Journal of Neuroscience 17(21): 8313–8323.

Tang, F., Dent, E.W., and Kalil, K. (2003). Spontaneous calcium transients in developing cortical neurons regulate axon outgrowth. Journal of Neuroscience 23(3): 927–936.

Telley, L., Govindan, S., Prado, J., Stevant, I., Nef, S., Dermitzakis, E., Dayer, A., and Jabaudon. (2016). Sequential transcriptional waves direct the differentiation of newborn neurons in the mouse neocortex. Science 351(6280): 1443–1446.

Thaler, J.P., Lee, S.K., Jurata, L.W., Gill, G.N., and Pfaff, S.L. (2002). LIM factor Lhx3 contributes to the specification of motor neuron and interneuron identity through cell-type-specific protein-protein interactions. Cell 110(2): 237–249.

Thu, C.A., Chen, W.V., Rubinstein, R., Chevee, M., Wolcott, H.N., Felsovalyi, K.O., Tapia, J.C., Shapiro, L., Honig, B., and Maniatis, T. (2014). Single-cell identity generated by combinatorial homophilic interactions between α, β, and γ protocadherins. Cell 158(5): 1045–1059.

Tian, D., Diao, M., Jiang, Y., Sun, L., Zhang, Y., Chen, Z., Huang, S., and Ou, G. (2015). Anillin regulates neuronal migration and neurite growth by linking RhoG to the actin cytoskeleton. Current Biology 25(9): 1135–1145.

Tomasiewicz, H., Ono, K., Yee, D., Thompson, C., Goridis, C., Rutishauser, U., and Magnuson, T. (1993). Genetic deletion of a neural cell adhesion molecule variant (N-CAM-180) produces distinct defects in the central nervous system. Neuron 11(6): 1163–1174.

Tsunemoto, R.K., Eade, K.T., Blanchard, J.T., and Baldwin K.K. (2015). Forward engineering neuronal diversity using direct reprogramming. EMBO Journal 34(11): 1445–1455.

Tsunemoto, R., Lee, S., Szũcs, A., Chubukov, P., Sokolova, I., Blanchard, J.W., Eade, K.T., Bruggemann, J., Wu, C., Torkamani, A., Sanna, P.P., and Baldwin, K.K. (2018). Diverse reprogramming codes for neuronal identity. Nature 557(7705): 375–380.

Verhage, M., Maia, A.S., Plomp, J.J., Brussaard, A.B., Heeroma, J.H., Vermeer, H., Toonen, R.F., Hammer, R.E., van den Berg, T.K., Missler, M., Geuze, H.J., Südhof, T.C. (2000).

Synaptic assembly of the brain in the absence of neurotransmitter secretion. Science 287(5454): 864–869.

Vicario-Abejon, C., Cunningham, M.G., and McKay, R.D. (1995). Cerebellar precursors transplanted to the neonatal dentate gyrus express features characteristic of hippocampal neurons. Journal of Neuroscience 15(10): 6351–6363.

Vierbuchen, T., Ostermeier, A., Pang, Z.P., Kokubu, Y., Südhof, T.C., and Wernig, M. (2010). Direct conversion of fibroblasts to functional neurons by defined factors. Nature 463(7284): 1035–1041.

Walsh, C., and Cepko, C.L. (1993). Clonal dispersion in proliferative layers of developing cerebral cortex. Nature 362(6421): 632–635.

West, A.E., Chen, W.G., Dalva, M.B., Dolmetsch, R.E., Kornhauser, J.M., Shaywitz, A.J., Takasu, M.A., Tao, X., and Greenberg, M.E. (2001). Calcium regulation of neuronal gene expression. PNAS 98(20): 11024–11031.

Wichterle, H., Turnbull, D.H., Nery, S., Fishell, G., and Alvarez-Buylla, A. (2001). In utero fate mapping reveals distinct migratory pathways and fates of neurons born in the mammalian basal forebrain. Development 128(19): 3759–3771.

Wichterle, H., Garcia-Verdugo, J.M., and Alvarez-Buylla, A. (1997). Direct evidence for homotypic, glia-independent neuronal migration. Neuron 18(5): 779–791.

Wray, S. (2002). Molecular mechanisms of migration of placodally derived GnRH neurons. Chemical Senses 27(6): 569–572.

Yang, H., Mujtaba, T., Venkatraman, G., Wu, Y.Y., Rao, M.S., and Luskin, M.B. (2000). Region-specific differentiation of neural tube-derived neuronal restricted precursor cells after heterotopic transplantation. PNAS 97(24): 13366–13371.

Zeisel, A., Hochgerner, H., Lönnerberg, P., Johnsson, A., Memic, F., van der Swan, J., Häring, M., Braun, E., Borm, L.E., Manno, G.L., Codeluppi, S., Furlan, A., Lee, K., Skene, N., Harris, K.D., Hjerling-Leffler, J., Arenas, E., Ernfors, P., Marklund, U., and Linnarsson, S. (2018). Molecular architecture of the mouse nervous system. Cell 174(4): 999–1014.

Chapter 2: Activity-based checkpoints for interneuron maturation and connectivity

Summary:

Olfactory circuits function at birth, yet are continuously remodeled by the integration of postnatally-born interneurons into the olfactory bulb (OB) in a manner that preserves perception throughout adult life. The mechanisms that regulate the development of interneurons and ensure circuit stability in this dynamic context remain poorly understood. Since granule cell (GC) interneurons sculpt the excitatory output of mitral and tufted (MT) neurons to the olfactory cortex, we predicted that MT neurons instruct interneuron integration in the adult brain. By blocking synaptic transmission from MT neurons using genetically-encoded tetanus toxin, we previously showed MT neuronal activity is critical to maintain OB integrity and interneuron survival. Here we have identified gene network modules that may regulate activity-dependent GC development. Inhibiting interneuron cell death in silent MT OBs uncovered a second activity-dependent checkpoint regulating GC dendrite morphology. Single cell tracing analyses of GCs showed these interneurons exhibit improved dendritic branching, yet still resemble immature neurons. Finally, transcriptome analyses of mature GCs and those stalled at developmental milestones identified gene regulatory networks that correlate with activity-dependent maturation and functional integration. These studies identify a circuit-specific role for non-sensory activity in regulating integration of neurons into the adult brain, which has implications for efforts in regenerative medicine.

Introduction:

Neurons form stereotyped circuits during development, yet must retain flexibility to adapt when challenged with new experiences throughout their lifetime. Intrinsic genetic programs are believed to dominate the initial formation of neuronal circuits, while neuronal activity in sensory systems has been shown to sculpt these architectures in later stages (Antón-Bolaños et al., 2019; Moore et al., 1985; Shatz et al., 1988; Sretavan et al., 1988; Verhage et al., 2000). Large parts of restructuring are completed before developmental critical periods either by spontaneous or sensory-driven activity, but are continuously refined and maintained at the synaptic level (Carulli et al., 2011, Pan et al., 2020). Whereas these processes have been studied extensively in the visual, auditory, somatosensory, and other sensory systems, less is known about how these mechanisms are balanced in the olfactory system.

For most systems, sensory information passes from the periphery through the thalamus before filtering into complex, six-layered cortical regions for additional downstream processing. The olfactory system is simpler. Odorants are detected by olfactory sensory neurons (OSNs) that express one in ~1200 odorant receptors in the peripheral, main olfactory epithelium (Young et al., 2002; Zhang et al., 2002). Dependent on their odorant receptor expression, OSNs project their axons to discrete, stereotyped locations in the olfactory bulb (OB) and converge with other OSNs expressing the same odorant receptor to form unique synaptic structures called glomeruli (Belluscio et al., 2002; Bozza et al., 2002; Gogos et al., 2000). Within glomeruli, OSNs form synapses with, and relay sensory information to innervating mitral and tufted (MT) neurons (Carlson et al., 2000; Chen et al., 1997; Schoppa et al., 2001). These MT neurons are the primary projection neurons of the OB, which transmit sensory information to the 3-layered piriform cortex and other olfactory areas (Schneider et al., 1983; Scott, 1981).

The olfactory system is further unique in that it is the only sensory system with adult neurogenesis in rodents (Lledo et al., 2016). OSNs in the periphery have a half-life of ~90 days and must project new axons to find already constructed glomeruli in order to form synapses with MT and periglomerular neurons and to maintain the transmission of sensory information into the brain (Gogos et al., 2000). Within the OB, new interneurons integrate throughout the lifetime of the animal and regulate both OSN and MT activity (Abraham et al., 2010; Tan et al., 2010). These inhibitory interneurons are born in the subventricular zone (SVZ) and migrate through the rostral migratory stream to reach the OB (Doetsch et al., 1996). Once they enter the OB, interneurons continue to migrate to different layers during which time they extend and elaborate dendritic branches as they seek active synaptic partners (Carleton et al., 2003; Petreanu et al., 2002). The largest group of these cells are granule cells (GCs) that form reciprocal synapses with MT neurons and shape outgoing signals to olfactory cortical areas. Roughly 50% of adult-born GCs die within the first two weeks of being born, likely as a mechanism to maintain proper excitatory/inhibitory balance within the OB dependent on successful synaptic integration (Petreanu et al., 2002). These principals of the olfactory system provide us a model system to study neuronal development beyond embryogenesis and mechanisms of integration into pre-existing neuronal circuits, which may be relevant for efforts in regenerative medicine.

Previous studies investigating the role of sensory activity in the olfactory system showed a driving role in shaping OSN development and glomerular targeting, but is limited for developing OB circuits (Yu et al., 2004). Enhanced sensory experience and occlusion experiments both show a mild impact on GC survival, dendritic branching, and spine density, but the architecture of the OB remains relatively unperturbed (Dahlen et al., 2011; Najbauer et al., 1995; Petreanu et al., 2002; Saghatelyan et al., 2005). These studies do not account for the role of

MT neurons, which exhibit spontaneous activity and may be the main drivers of OB development (Chaput et al., 1992). In fact, GCs receive the majority of their excitatory inputs from MTs starting as early as 10 days after being born in the SVZ (Whitman et al., 2007). This led us to ask whether MT neuronal activity impacts GC and OB development.

MT neurons drive activity in GCs through basal dendrites before forming direct reciprocal synapses on distal dendrites (Whitman et al., 2007). Previous work demonstrated MT input onto GCs regulates local dendritic branching and spine dynamics (Breton-Provencher et al., 2014; Breton-Provencher et al., 2016). In the Baldwin laboratory, a genetically-encoded tetanus toxin (TeNT) approach was developed to globally block synaptic transmission from MT neurons to their synaptic partners (James, 2013). Using this approach, they found MT activity plays a dramatic role in promoting GC survival and maturation as well as shaping the development of the OB. We aimed to extend these results in order to probe and understand the molecular mechanisms regulating integration and maturation of GCs in OB circuits.

Results:

Blocking cell death uncovers a developmental checkpoint regulated by MT activity

Previous experiments in the Baldwin laboratory established MT activity is important for regulating both GC survival and development as indicated by the complexity of their apical dendritic tree (James, 2013). One signature of programmed cell death in neurons is neurite degeneration, where dendrites and axons shorten prior to cell death (Yang et al., 2013). Are the short, simple dendritic trees we observed in MT-activity-attenuated GCs a symptom of cell death or a sign of immature neurons? To distinguish between these models, we utilized a global Bax knockout transgenic mouse (KO) to block apoptosis (Knudson et al., 1995).

The Bax genetic deletion was bred into the TeNT-GFP and *Pchd21*-IRES-Cre mouse lines, which were then crossed to generate MT-T KO mice (Figure 2.1a and b). Similar to *Pchd21*-IRES-Cre X TeNT (MT-T) mice, MT-T KO animals were significantly smaller than wild-type (WT) and KO littermates indicating they may still have olfactory deficits (Figure 2.2). In order to validate the Bax genetic deletion, we stained for cleaved caspase-3 (CC-3), a marker for apoptotic cells, and counted dying GCs in the OB granule cell layer (GCL). MT-T KO mice exhibited a dramatically reduced density of CC-3+ cells in the GCL, showing that deleting Bax rescues the GC cell death phenotype (Figure 2.3a and b).

The blockade of MT activity in MT-T mice showed a significant decrease in immediate early gene expression throughout the olfactory system (James, 2013). To ensure rescuing cell death and increasing the number of inhibitory GCs did not alter network levels of activity within the OB, we quantified the expression of two immediate early genes in GCs, Egr1 and cFos. Importantly, the density of Egr1+ and cFos+ cells in the GCL did not change between MT-T and MT-T KO mice (Figure 2.4a and b). We also examined a direct target of both OSNs and MT neurons in the OB, the periglomerular neurons, which express tyrosine hydroxylase (TH) in an activity-dependent manner (McLean et al., 1988). The density of TH+ neurons in the glomerular layer (GL) was unaltered in any genotype, likely because OSN signaling remains intact (Figure 2.4a and b). Together, these results indicate the removal of Bax rescues the cell death phenotype yet maintains the activity deficit as desired.

Having validated our cell death blockade, we assessed its impact on the development of the OB. Our previous studies showed silencing MT neuronal activity led to dramatically smaller OBs with aberrant laminar structures (James, 2013). Quantifications of each layer in MT-T KO mice revealed the OB architecture was partially rescued (Figure 2.5a). The overall increase in

area was driven mainly by the restoration of the GCL as compared to MT-T mice (Figure 2.5b). MT-T KO OBs remain significantly smaller than WT though due to an only partial increase in the external plexiform layer (EPL), where GCs form reciprocal dendro-dendritic synapses with MT neurons (Rall et al., 1966; Nicoll, 1969). This suggests that although the cell death blockade increases the number of GCs populating the GCL, the elaboration of their dendritic trees into the EPL may remain impaired.

The development of postnatally-born GCs has been described to occur in five distinct stages (Carleton et al., 2003; Petreanu et al., 2002). Neuroblasts migrating through the rostral migratory stream (Stage 1) direct the orientation of their leading process radially toward the outer layers of the OB (Stage 2) once they reach the inner core. These young neurons continue to migrate and extend their leading dendritic process toward the EPL and begin to exhibit excitatory and inhibitory postsynaptic events (Stage 3). By 14 days, most newborn GCs have elaborated, spineless apical dendrites that branch into the EPL (Stage 4). Finally, starting as early as 15 days after birth, the dendrites develop more branches and dendritic spines, and GCs reliably fire action potentials (Stage 5).

Previously the Baldwin lab demonstrated blocking MT activity dramatically reduces GC dendritic length, complexity, and spine density as early as 15.5 days after birth (James, 2013). To determine how the deletion of Bax alters the development and maturation of newborn GCs, we used a lentiviral approach to label neuronal progenitors surrounding the SVZ with a hUbc-HA-FLAG-eGFP cassette via intraventricular injection (Figure 2.6a). This allows us to sparsely label newborn GCs and monitor their migration and growth at desired time points (Figure 2.6b). Building three-dimensional reconstructions of labelled cells 21 days post-injection (dpi) showed GCs in MT-T KO mice are not fully mature. Blocking apoptosis allows these neurons to extend

their apical dendrite further than in MT-T mice, but their dendritic branch complexity remains significantly reduced compared to GCs in WT mice (Figure 2.7a and b). These findings are consistent with the partial rescue of EPL area that we observed and suggest that non-sensory activity levels separately regulate both GC survival and morphological maturation.

The immune system in the brain has gained recent attention for its role in both neuronal circuit maintenance as well as degeneration (Li et al., 2018). Since blocking MT neurotransmission within the OB circuit creates a degenerative phenotype with elevated levels of interneuron cell death and neurite atrophy, we hypothesized microglia, the brain's immune cells, would be more active in MT-T mice. To investigate this in our system, we stained and counted active microglia in the OB. The density of Iba1+ microglia was increased in the GCL and EPL of MT-T but not MT-T KO mice as compared to WT (Figure 2.8a and b). Furthermore, the percentage of these Iba1+ microglia expressing CD68, a marker for active phagocytic cells (Perego et al., 2011), was increased in all three OB layers of MT-T mice compared to both WT and MT-T KO, indicating these cells are actively clearing cellular debris, including dead GCs (Figure 2.8a and b). The recruitment of active microglia to sites of degenerating interneurons in MT-T OBs suggests this is a reproducible system to model neuronal degeneration and its associated immune response.

Defining gene networks regulating GC development and maturation

A goal of developmental neuroscience is to define and dissect genetic mechanisms that enable neurons to specify, mature, and integrate into circuits throughout development as well as in degenerative states. To identify genes that regulate the activity-dependent survival and maturation of GCs in the OB, we used population RNA sequencing (RNA-Seq) to profile the

transcriptome of developing GCs in our genetic system. Newborn GCs were labelled with HA-FLAG-eGFP and collected at either dpi 14 or 21 using fluorescent-activated cell sorting (FACS) to enrich for DAPI-, DRAQ5+, eGFP+ GCs at different developmental milestones (Figure 2.9a and b). Approximately 3,000 to 4,000 cells were required to obtain 2 ng of total RNA, which served as input to build RNA-Seq cDNA libraries (Table 2.1). Libraries were sequenced to an average depth of ~39.6 million reads, aligned to a reference mouse genome, and a CPM filter imposed to remove non-expressed genes (36132/48397, 74.66%).

In order to verify the sequenced cells were GCs, we explored the expression of known genes from all OB cell subtypes (Figure 2.10a). As expected, samples showed high expression of common neuronal genes (*Map2*, *Tubb3*, and *Snap25*) and genes selective to GABAergic neurons (*Gad1, Gad2, Slc32a1/Vgat,* and *Slc6a1/Gat1*), but low expression for genes selectively expressed in glutamatergic neurons (*Slc17a6/Vglut2* and *Slc17a7/Vglut1*), MT neurons (*Eomes/Tbr2, Tbr1,* and *Cdhr1/Pcdh21*), OSNs (*Omp*), microglia (*Tmem119, Cx3cr1,* and *Aif1/Iba1*), and astrocytes (*Gfap* and *Slc1a3/Eaat1*). Some samples showed contamination by subsets of these populations. To remove any bias of these gene subsets from downstream analyses, samples were grouped based on their median expression of subtype-specific and sex-dependent genes (Figure 2.10b) and used for comparison to identify differentially expressed genes (Figure 2.10c). In total, 1083 (1083/12265, 8.83%) unique genes were removed, leaving 11182 genes for downstream analysis (11182/48397, 23.10%).

To understand the relationship amongst GCs collected from all genotypes at different time points, we conducted correlation clustering. Samples largely segregated by time point as well as the expression of TeNT with the exception of some MT-T KO and KO samples (Figure 2.11). Principal component analysis (PCA) can provide more informative clustering including

the weight every gene contributes to each component. Using PCA, we detected four clusters within the first three calculated principal components (PCs): 1) dpi 21 WT and KO; 2) dpi 21 MT-T KO; 3) dpi 21 MT-T; and 4) dpi 14 all samples (Figure 2.12a). Notably, PC1 separated dpi 14 from dpi 21 except for dpi 21 MT-T, which grouped closer to more immature, dpi 14 samples (Figure 2.12b). Gene ontology term (GO-term) analysis for the top 200 contributing genes for each direction showed positive PC1 samples (dpi 14) were significantly enriched for genes that regulate cell migration, whereas negative PC1 (dpi 21) samples were enriched for genes necessary for more mature neuronal processes, including synaptic transmission (Figure 2.12c). Alternatively, PC2 identified the expression of TeNT such that WT and KO scored high and MT-T and MT-T KO scored low, but GO-term analysis only implicated cell adhesion. Separation by PC3 on its own was unclear. Together, these analyses demonstrate transcriptional analysis has the power to separate GC samples into phenotypically-relevant clusters.

These PCA-defined clusters follow what we might expect from our GC morphology analysis such that WT, MT-T, and MT-T KO occupy distinct developmental stages (Figure 2.13a). In order to identify genes relevant for each hypothesized stage, three differential gene expression analyses were set up for neighboring phenotypes: 1) MT-T vs MT-KO, 2) MT-KO vs KO, and 3) MT-T vs WT. We hypothesized that looking at the overlap of genes identified from these comparisons may implicate gene sets crucial for the transitions between our hypothesized developmental stages (Figure 2.13b). Differential gene expression analyses were run (Figure 2.14a) and genes significantly upregulated in the more mature phenotype (dpi 14: 683/955 genes, 71.51%; dpi 21: 1063/1298, 81.89%) were used for overlap analysis (Figure 2.14b). At dpi 14, when GCs are predicted to be in the middle stages of their development, 39 (39/638, 6.11%) genes were identified as stage 4 development genes and only 6 (6/638, 0.94%) for stage 5. As

suspected, these numbers expanded to 102 (102/834, 12.23%) and 84 (84/834, 10.07%) at dpi 21, when WT GCs are morphologically mature.

Transcription factors are regulators of the genome that work together to coordinate a larger expression gene profile, which can drive the specification and development of neurons (Tsunemoto et al., 2018; Yap, et al., 2018). To identify what genes may establish these developmental stages, we used a GO-term search for transcriptional regulators amongst the significantly upregulated gene lists at dpi 14 and 21, and conducted an overlap analysis (Figure 2.15a). Only one (1/30, 3.33%) transcriptional regulator, *Ndn*, was implicated for the stage 4 transition at dpi 14 (Figure 2.15b), which has been found to promote GABAergic neuron differentiation as well the survival of sensory neurons in dorsal root ganglion (Andrieu et al., 2006; Kurita et al., 2006; Kuwajima et al., 2006). As few GCs enter the final stage of their development by 14 days, it is unsurprising that no transcriptional regulators were identified for the stage 5 transition at this time point.

At dpi21 the stage 4 transcriptional regulators increased to 6 (6/41, 14.63%). Whereas *Aebp1*, *Klf9,* and *Bhlhe40* mainly regulate stress responses, *Plagl1* regulates differentiation and development within the cerebellum and cortex, and both *Mkl2* and *Nr4a1* shape dendritic branch morphology and spine density in an activity-dependent manner (Adnani et al., 2015; Besnard et al., 2018; Chen, et al., 2014; Chung et al., 2011; Hamilton et al., 2018; Kaneda et al., 2018; Majdalawieh et al., 2010; Shijo et al., 2018). Furthermore, four genes were identified for stage 5 (4/41, 9.76%), including the neuroprotector *Pparg* and circadian gene *Npas2* (DeBruyne et al., 2007; Warden et al., 2016). *Hdac5* is an upstream regulator of the immediate-early gene *Npas4*, which has been shown to regulate spine density of GCs in an activity-dependent manner, and is in the same family as *Hdac4*, a known regulator of neuronal survival and synaptic strength in the

hippocampus (Sando III et al., 2012; Taniguchi et al., 2017; Yoshihara et al., 2014; Zhu et al., 2019). *Hivep2* has also been implicated to play a role in spine morphology and may have relevance for schizophrenia and autism (Nakao et al., 2017; Srivastava, et al., 2015). Together, these implicated transcriptional regulators highlight the role spine dynamics, dendritic branch morphology, and cell survival play in the final stage of GC development.

Alternative to a biased, manual overlap analysis, weighted gene co-expression network analysis (WGCNA) can be used to identify unbiased, highly correlated gene clusters, which can then be related to observed phenotypes (Langfelder et al., 2008; Zhang et al., 2005). We ran WGCNA on all 24 samples to identify 22 unique modules that accounted for 10438 of the input gene list (10438/11182, 93.35%) (Figure 2.16a and b). Plotting the expression pattern across each genotype identified certain modules that were enriched in more mature GCs as well as in less developed genotypes, resembling our results from the overlap comparisons. Four modules (modules 2, 3, 4, and 11) showed enriched expression in dpi 21 WT samples and included genes related to transcription, calcium signaling, and synaptic transmission (Figure 2.17a and b). Intriguingly, modules 3 and 4, which are most enriched for genes important for neuronal signaling show different patterns, such that module 3 is highly enriched in stage 4 genotypes (MT-T KO, KO, and WT), and module 4 is highest in stage 5 genotypes (KO and WT). Of the 11 transcriptional regulators identified through overlap analysis, 10 (10/11, 90.91%) were contained in modules 3, 4, and 11, yet these modules identified an additional 51 regulators (Module 3: 16; Module 4: 28; Module 11: 7). The only one missing, *Aebp1*, was not assigned to any module. Furthermore, other transcription factors previously identified to play an activity-dependent role in shaping neuronal development and synaptogenesis were contained within these modules (Module 2: *Myc*, *Mycn*, *Jun*, *Junb*; Module 3: *Crem*; Module 4: *Fosl2*; Module 11:

Fosb, *Npas4*). Together, these bioinformatic analyses document gene networks that are directly regulated by MT activity and shape discrete stages of newborn GC development and integration into established OB circuits.

Discussion:

Here, we identify a second activity-dependent developmental checkpoint for newborn GCs integrating into the OB by inhibiting their ability to undergo programmed cell death. While their initial survival is gated by MT neuronal activity, GCs require continued input from MT neurons for their full maturation into olfactory circuits. Furthermore, we have uncovered unique gene networks that regulate these checkpoints using RNA-Seq. These studies extend our understanding of olfactory circuit development and maintenance, and provide insights into the rules governing the integration and survival of neurons into pre-existing circuits with relevance for ongoing studies in regenerative medicine.

A second activity-dependent developmental checkpoint

MT neurons have a basal firing rate that is enhanced by OSN activity. While most studies have focused on the role OSN input plays in olfactory system development, few have examined how MT activity shapes these circuits beyond local regulation of GC synapses (Breton-Provencher et al., 2014; Breton-Provencher et al., 2016). Previous experiments in the Baldwin laboratory identified an activity-based checkpoint in GC development by blocking neurotransmission from MT neurons (James 2013). Both embryonically- and adult-born interneurons were shown to require MT activity for their survival in OB circuits. This mechanism may exist in order to regulate the number of incoming neurons into the OB and thus

maintain appropriate excitatory/inhibitory balance for olfactory circuits, which is important for proper sensory coding and perception (Sohal, et al., 2019; Zhou et al., 2018). Indeed, computational models have previously predicted that GC death maximizes odor discrimination for a changing environment, and experimental evidence demonstrates neurogenesis promotes OB plasticity and complex odor discrimination (Alonso et al., 2012; Breton-Provencher et al., 2009; Cecchi et al., 2001; Nissant et al., 2009).

In an effort to understand the mechanisms that enable integration, here we identify a second activity-dependent developmental checkpoint for GCs. By globally knocking out Bax, we show the full maturation of surviving GCs requires continued MT neuronal activity. These findings suggest activity instructs dendritic growth of GCs and is necessary to drive their complete integration into OB circuits. This is the opposite of other circuits, where activity refines overly-elaborate dendritic trees (Leighton et al., 2016). Furthermore, this may be a different integration mechanism than for embryonic-born GCs in the OB, which do not change their dendritic trees upon loss of sensory activity (Saghatelyan et al., 2005). Therefore, activity-dependent dendritic growth of newborn GCs and their innervation onto synaptic targets may be a feedback mechanism for shaping MT activity based on the relative abundance of environmental olfactory cues. Together with regulating an initial GC survival checkpoint, this second activity-dependent GC innervation checkpoint may help govern the excitatory/inhibitory balance for olfactory circuits as needed based on experience. It is intriguing to hypothesize that MT neurons may recruit GCs based on their levels of excitation. Future studies utilizing approaches to perturb the activity in local groups of MT neurons would be needed in order to address whether MT neurons compete for GC innervation.

Intrinsic mechanisms governing integration into existing neural circuits

Activity-dependent calcium signaling in neurons is important for the regulation of many processes including migration, growth, plasticity, and survival (Rosenberg et al., 2011). One molecular mechanism through which internal calcium mediates these processes is by altering gene expression (West et al., 2001). Transcriptional analysis by RNA-Seq has led to an eruption of studies investigating the gene networks regulating cell identity, development, and degeneration. Using an unbiased approach to profile the transcriptome of developing GCs in our system, we identify distinct gene sets that may regulate unique stages of GC survival, maturation, and integration into OB circuits. Additionally, we isolated several transcriptional regulators that may be key to guiding transitions between developmental stages and activity-dependent checkpoints. For example, *Ndn* was found to be highly expressed in earlier stages of GC development, possibly to promote cell survival as well as the specification into a GABAergic neuronal identity. At later times, regulators of stress response (*Aebp1*, *Bhlhe40*, and *Klf9*) may be activated to promote cell survival, while other programs are initiated through the recruitment of *Nr4a1*, *Mkl2*, and *Plagl1* to drive dendritic development and stabilize a terminal, GABAergic neuronal identity. Finally, the activation of end-stage transcriptional programs (*Hdac5* and *Hivep2*) may push GCs beyond their second checkpoint to elaborate dendritic trees and form synapses, thus finalizing their integration into the OB.

These identified transcriptional programs are by no means exhaustive. WGCNA built gene modules with similar expression profiles to our overlap analysis and implicated an additional 51 transcriptional regulators that may direct GCs through these developmental checkpoints. In addition, some modules showed interesting differential expression patterns that were time-dependent (modules 7, 8, and 12) or enriched in MT genotypes (modules 5, 9, 10, 18,

and 19). These should be explored thoroughly to gain insight into activity-independent programs of maturation as well as programs driving degeneration and cell death. Deeper computational analyses of these generated gene modules is also required in order to investigate the interplay between them, build regulatory gene networks, and perhaps identify upstream master regulators. Ideally, these networks would be validated with *in vivo* overexpression and knock-down experiments of candidate genes. Furthermore, characterization of genes belonging to other gene families such as surface adhesion molecules and receptors will paint a broader picture of the molecular landscape regulating GC survival, development, and integration (Ledderose et al., 2013; Luo et al., 2015; Tseng et al., 2017).

One caveat to our study is the population of sequenced cells represents a heterogeneous pool of neurons from diverse subtypes and at various stages of their development. To get around this, we attempted a similar experiment but using single-cell RNA-Seq, which would allow us to profile the transcriptome of individual neurons and bioinformatically build developmental trajectories based on gene expression signatures. Unfortunately, our methods did not detect the large number of high-quality cells needed for such downstream analyses (<1500 cells, mean gene discovery rate ~500, data not shown). Alternatively, a recent study conducted a series of single-cell RNA-Seq experiments from all OB neuronal subtypes in WT, environmentally-enriched, and olfactory-deprived mice (Tepe et al., 2018). By omitting a FACS step to purify a neuronal subtype of interest, they collected >50,000 cells and could readily cluster inhibitory neurons based on developmental stages and subtypes. Using pseudo-timeline analysis, they found GCs evenly followed one of two trajectories, which became biased by either olfactory enrichment or deprivation. Conducting differential expression analysis, the authors identified transcriptional regulators enriched in the olfactory enrichment path including *Hivep2*, *Fosl2*, and *Mef2d*. We

also identified these three regulators in GCs using WGCNA (module 4). Further comparisons between this single-cell and our population RNA-Seq datasets may better inform our understanding of the molecular mechanisms regulating these developmental checkpoints.

It is tempting to ask whether our identified gene networks function the same in embryonically- and postnatally-born GCs. Given these two populations show differential responses to activity, they may regulate these activity-dependent gene networks differently. Alternatively, embryonically-born GCs may utilize different pathways. Differential transcriptome analyses of these populations and *in vivo* genetic manipulation studies would yield insight to these questions.

Ultimately, these data provide a genetic model to systematically study the rules for driving neuronal development and integration into pre-existing circuits. Furthermore, we index genes revealed to be differentially expressed at key developmental checkpoints for neuronal maturation. Future studies will continue to elucidate these molecular mechanisms that regulate neuronal circuit formation and plasticity, with the goal of aiding efforts in therapeutic strategies for regenerative medicine.

Acknowledgements:

Chapter 2, in part, is a reprint of the material as it appears in James, K.N., Throesch, B.T., Davini, W., Eade, K.T., Ghosh, S., Lee, S., Torabi-Rander, N., and Baldwin K.K., 2017, Activity based checkpoints ensure circuit stability in the olfactory system, bioRxiv. K.N.J. was the primary investigator and author of this paper.

Materials and methods:

Mouse strains

The TeNT-GFP mouse strain was previously provided by Martin Goulding (Zhang et al., 2008). *Pcdh21*-IRES-Cre (Boland et al., 2009) mice were generated by Kristin Baldwin in the Axel laboratory. Bax knockout mice were originally generated by Stanley Korsmeyer (Knudson et al., 1995) and ordered from The Jackson Laboratory (Stock # 002994). All lines were bred as homozygous except for Bax knockout mice as homozygous KOs do not produce litters. To generate triple transgenic *Pcdh21*-IRES-Cre, TeNT-GFP, KO (MT-T KO) mice, Bax heterozygous knockout mice were bred first with *Pcdh21*-IRES-Cre and TeNT-GFP mice to generate dual transgenic lines, which were subsequently used as breeders for MT-T KO mice. WT controls were either Cre or TeNT-GFP positive, and Bax WT.

All animal experiments were conducted in accordance with the protocols approved by the IACUC of The Scripps Research Institute and NIH guidelines for animal use.

Genomic PCR

Genomic DNA was extracted from tail tip samples using the DNeasy Blood and Tissue kit (Qiagen 69504) or the REDExtract-N-Amp Tissue PCR kit (Sigma-Aldrich XNAT-100RXN). PCRs were performed using the Platinum PCR SuperMix High-Fidelity kit (Thermo Fischer Scientific 12532016), the Q5 Hot Start High-Fidelity 2X master mix (New England Biolabs M0494S), or the REDExtract-N-Amp PCR Readymix (Sigma-Aldrich R4775).

The following primers were used for genotyping:

TeNT-GFP Mutant Forward: 5’ – GGA GCG GGA GAA ATG GAT ATG – 3’

TeNT-GFP WT Forward: 5’ – CAT CAA GGA AAC CCT GGA CTA CTG – 3’

TeNT-GFP Reverse: 5’ – AAA GTC GCT CTG AGT TGT TAT – 3’

Cre Forward: 5’ – CGC ATA ACC AGT GAA ACA GCA – 3’

Cre Reverse: 5’ – CGC ATA ACC AGT GAA ACA GCA – 3’

Pcdh21 WT Forward: 5’ – ACC ACC CCC TAA AAT GGC ATC C – 3’

Pcdh21 WT Reverse: 5’ – TCT GAG GCA TCT CTT GCC CAA – 3’

Bax knockout Mutant Forward: 5’ – CTT CCT GAC TAG GGG AGG AG – 3’

Bax knockout WT Forward: 5’ – GCA GAG GGT TAA AAG CAA GG – 3’

Bax knockout Common Reverse: 5’ – ACC CAG CCA CCC TGG TCT – 3’

Tissue preparation and immunohistochemistry

Mice P21 were transcardially perfused with dPBS (Gibco 14910) and subsequently with 4% PFA (EMS 15710) in dPBS. Brains with OBs attached were dissected from the skull and placed in 4% PFA solution overnight at 4°C. The following day, brains were washed and stored in dPBS at 4°C. For vibratome sections, brains were embedded in 4% low-melt agarose (Bio-Rad 161-3114) and sectioned in the coronal plane at 80 μm using a Leica VT1000S. For IHC, free-floating sections in 24-well plates were treated with blocking buffer (10% heat-inactivated horse serum (Lonza BioWhittaker 14-403F) in dPBS-T (dPBS + 0.1% Triton X-100 (Sigma-Adlrich T8787))) for 1 hr at room temperature. Primary antibodies were diluted 1:500 in blocking buffer, added to sections, and left gently agitating overnight at 4°C. Sections were washed in dPBS-T three times for 10 min per wash to remove excess primary antibody before secondary antibodies and DAPI (5 mg/ml, Invitrogen D1306), both diluted 1:1000 in dPBS-T, were applied for 1 hr at room temperature. Sections were rinsed again in dPBS-T three times for

10 min each, then mounted using ProLong Diamond Antifade Mountant (Invitrogen P36965), and left covered overnight at room temperature to dry before imaging.

Primary antibodies used:

CC-3 (rabbit, CST 9661)

Egr1 (rabbit, SCBT sc-189)

cFos (guinea pig, SySy 226 004)

TH (rabbit, Pel-Freez P40101-150)

HA (mouse, BioLegend 901501)

Iba1 (goat, Abcam ab5076)

CD68 (rat, AbD Serotec MCA1957GA)

Secondary antibodies used:

rabbit, Alexa Fluor 488 (donkey, Invitrogen A21206)

rabbit, Alexa Fluor 555 (donkey, Invitrogen A31572)

guinea pig, Alexa Fluor 647 (donkey, Jackson ImmunoResearch 706 605 148)

mouse, Alexa Fluor 488 (donkey, Invitrogen A21202)

goat, Alexa Fluor 647 (donkey, Abcam ab150131)

rat, Alexa Fluor 488 (donkey, Abcam ab150154)

Lentiviral constructs, production, and intraventricular injection

The HA-FLAG-eGFP cassette (Addgene #22612) was generated in the laboratory of W. Harper (Sowa et al., 2009) and cloned into a lentiviral transfer plasmid with a hUbC promoter in the laboratory of K. Baldwin (James, 2013). To generate lentivirus, third generation packaging plasmids pRRE (Addgene #12251) and pRev (Addgene #12253), envelope expressing plasmid

pMD2.G (Addgene #12259), and transfer plasmid were co-transfected using the calcium-phosphate precipitation method (Graham et al., 1973) into HEK cells (ATCC CRL-3216). HEK cells were cultured with standard HEK media (DMEM with GlutaMAX (Gibco 10566016), 10% heat-inactivated fetal bovine serum (FBS), 1X penicillin-streptomycin (Gibco 15140122)). Live lentivirus was harvested 48 hr post-transfection, concentrated by ultracentrifugation (2 hr, 25000 rpm at 4°C), resuspended at 1:250 in dPBS, and stored at -80°C.

For intraventricular injections, a simple manual air pressure-based system using a 3 ml syringe, plastic adaptors, and thin tubing was constructed and fitted with a glass micropipette (~10 μm tip diameter). Neonatal mice (P0-P2) were anesthetized on wet ice. To identify the sites for injection, a line was drawn from bregma (visualized through the skin) to each eye and the target marked with a fine-tip marker approximately 1/3 of the way from bregma. The micropipette was inserted through the skin and skull to a depth of 1-2 mm relative to the skin surface, and 1-2 μl of virus was ejected. After a brief pause, the micropipette was slowly removed before injecting the other hemisphere. Tail samples were collected for genomic PCR and animals were tattooed for identification using the AIMS Neo-9 Neonate Rodent Tattooing System (Thermo Fisher Scientific 14-370-129). Mice recovered in a cage resting on a warm heating pad for several minutes before returning to their home cage.

Confocal imaging, image processing, and neuronal reconstructions

All images were acquired on a Nikon A1 confocal microscope and analysis was performed using Nikon NIS-Elements. Cell counts were either automated (CC-3, Egr1, cFos) or done manually (TH, Iba1, CD68) depending on the signal intensity, background, and colocalization. Measurements were normalized by area to anatomically defined regions using

DAPI counterstaining. To calculate the area of each OB layer, maximal coronal sections just anterior to the accessory olfactory bulb were used. Three concentric rings were drawn using DAPI counterstaining as a guide. The first region traced the interior edge of the mitral cell layer (MCL), and the calculated area defined the GCL. The second region followed the interior edge of the GL, and the difference between this and the first section defined the EPL. The third region traced the outer edge of the GL, omitting the olfactory nerve layer (ONL). Subtracting the other two regions from this defined the GL.

For GC dendritic branch reconstructions, images were acquired as automatically stitched, large-image, z-stacks at 40x and were traced using MBF Bioscience Neurolucida. For each image, up to thee neurons entirely contained within the z-stack were chosen to reconstruct in the outermost layers of the GCL. Trailing dendrites were excluded from tracings.

Fluorescence-activated cell sorting

Lentiviral-labelled GCs were isolated from appropriately genotyped mice at P14 or P21 similar to Tsunemoto et al. (2018). Briefly, mice were anesthetized using isoflurane and then rapidly decapitated. The skull was lifted to expose the OBs, which were removed and placed briefly into cold HAGB solution (Hibernate-A (Gibco A1247501), 1x B-27 supplement (Gibco 12587010), 500 μM GlutaMAX (Gibco 35050061)). HAGB solution was replaced with 37°C papain solution (Hibernate-A, 500 μM GlutaMAX, 2 U/ml DNase I (NEB M0303S), 10 U/ml PAP2 (Worthington Biochemical LK003176)) for a maximum of 10 min. During papain digestion, samples were triturated every 5 min using P1000 plastic tips. Digested samples were loaded onto 4-layered density gradients starting from 7.4% (% v/v) on top, 9.9%, 12.4%, and 17.3% OptiPrep (Sigma-Aldrich D1556) in Hibernate-A, and centrifuged at 800 *g* for 15 min.

The cell pellet was washed in 5 ml fresh HAGB solution, centrifuged at 200 *g* for 5 min, and subsequently resuspended in HAGB before being strained through a 35 μm nylon mesh filter. Cells were stored on ice and the viability markers DAPI (1 μM) and DRAQ5 (BioStatus DR50050, 1 μM) were added to the single-cell suspension at least 10 min before sorting. Appropriate gates were set based on DAPI, DRAQ5, and eGFP intensities to isolate live, eGFP-positive neurons using a MoFlo Astrios (Beckman Coulter). Isolated cells were sorted directly into 500 μl TRIzol LS (Invitrogen 10296010).

Population RNA isolation, library preparation, and sequencing

RNA was isolated from sorted cells using the Direct-zol RNA MiniPrep Kit (Zymo Research R2050). The manufacturer's protocol was followed using the in-column DNase I treatment, except 1 μg/μl linearized acrylamide (Invitrogen AM9520) was added to each sample before starting the purification, and Zymo-Spin IC columns were substituted for IIC columns because of low expected RNA yields. RNA quality and quantity was determined using an Agilent 2100 Bioanalyzer.

For all samples, 2 ng of RNA was used to prepare cDNA with the SMARTer Ultra Low Input RNA Kit for Sequencing v3 (Clontech Laboratories). First strand cDNA was amplified for 11 cycles, assessed using the Qubit Fluorometer (Invitrogen), and sheared using the Covaris system. Sequencing libraries were built with 7 ng of cDNA per sample using the NEBNext Ultra DNA Library Prep Kit for Illumina and sequenced using Illumina's NextSeq platform to an average depth of ~39.6 million reads per sample (range: 27.3 to 57.8 million reads). Adaptor sequences were removed from single-end reads using Trimmomatic v0.36 (Bolger et al., 2014)

and then aligned to the mouse genome (UCSC mm10 database) using STAR v2.3.0 (Dobin et al., 2013). Transcript counts were generated using HTSeq (Anders et al., 2015).

RNA-Seq data analysis

RNA-Seq data analysis was conducted using R. Raw read counts were first transformed to counts per million (CPM). To remove low-expressed genes, biological replicates were averaged together and genes with CPM values below 5 for all averaged samples were removed for downstream analysis (36132/48397 transcripts, 74.66%). Expression values were further transformed using the $\log_2$(CPM+1) transformation. To identify contaminating genes from undesired cell populations (astrocytes, microglia, OSNs, MT neurons) or condition (sex), expression values of known genes for all samples were plotted. Samples falling outside the 95% confidence interval (CI) were grouped together for differential gene expression analysis using DESeq2 v3.10 (Love et al. 2014). Genes enriched for microglia (284), astrocytes (758), OSNs (1), MT neurons (811), and sex-specific differences (11) were removed for downstream analysis (1083 total) leaving 11182 (23.10%) genes for analysis.

Correlation clustering and PCA were run using $\log_2$(CPM+1) counts. Heatmaps were generated using gplots and principal component plots with pca3d R packages. Differential gene expression analysis between genotypes was run on rawcounts using the DESeq2 package. GO-term enrichment analysis was conducted with the Panther Classification System (Huaiyu et al., 2018) considering Slim Biological Process terms, using Fisher's Exact test, and the Bonferroni correction for multiple testing. WGCNA (Zhang et al., 2005; Langfelder et al., 2008) was applied to generate signed gene modules from filtered $\log_2$(CPM+1) counts with a power=20, minModuleSize=30, deepSplit=4, cutHeight=0.999, and mergeCutHeight=0.20.

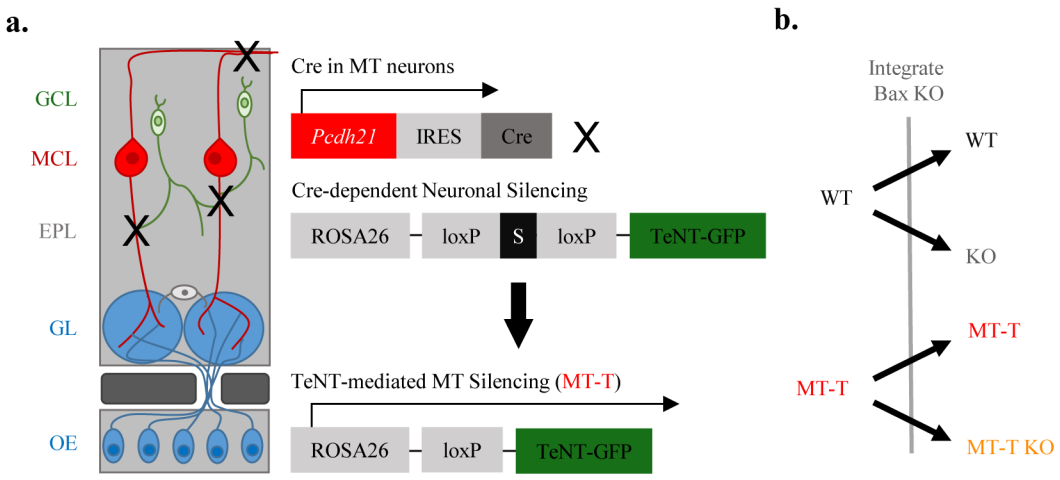

Figure 2.1: Genetic strategy schematic to globally block cell death.
(a) Cre is selectively co-expressed with Pcdh21 using IRES in MT neurons. Crossing these mice with TeNT-GFP mice leads to the deletion of the stop codon in order to permit expression of TeNT in MT neurons.
(b) The Bax knockout allele was bred into *Pcdh21*-IRES-Cre and TeNT-GFP mice in order to generate four genotypes for comparisons; WT, WT with Bax knockout (KO), MT-T, and MT-T with Bax knockout (MT-T KO).

a.

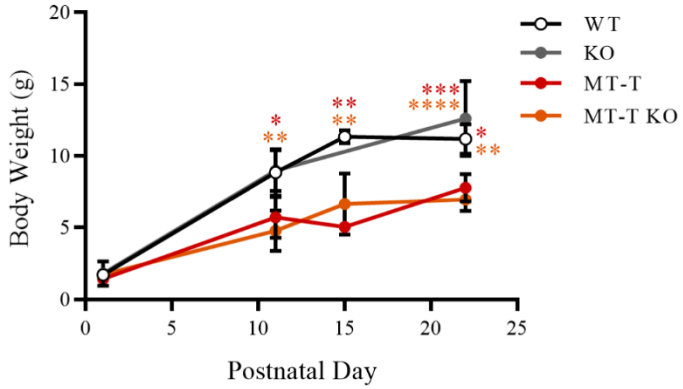

Figure 2.2: MT-T KO animals exhibit growth abnormalities.
(a) MT-T and MT-T KO mice were significantly smaller than WT littermates throughout their first three weeks of development. 3 animals/genotype, except no p15 KO mice. Dots and error bars represent mean plus SD. P1: WT: 1.73 ± 0.15; KO: 1.80 ± 0.85; MT-T: 1.43 ± 0.23; and MT-T KO: 1.73 ± 0.25. No significance in any comparisons. P11: WT: 8.85 ± 1.62; KO: 8.99 ± 1.43; MT-T: 5.72 ± 1.43; and MT-T KO: 4.79 ± 1.39. WT vs MT-T p = 0.0263, WT vs MT-T KO p = 00.30, KO vs MT-T p = 0.0192, KO vs MT-T KO p = 0.0021. P15: WT: 11.35 ± 0.46; MT-T: 5.06 ± 0.28; and MT-T KO: 6.66 ± 2.15. WT vs MT-T p = 0.0023, WT vs MT-T KO p = 0.0099. P22: WT: 11.19 ± 1.04; KO: 12.60 ± 2.60; MT-T: 7.79 ± 0.95; and MT-T KO: 6.96 ± 0.81. WT vs MT-T p = 0.0142, WT vs MT-T KO p = 0.0020, KO vs MT-T p = 0.0005, KO vs MT-T KO p < 0.001. Two-way ANOVA followed by Tukey's multiple comparisons test.
*p < 0.05, **p < 0.01, ***p < 0.001, ****p < 0.0001.

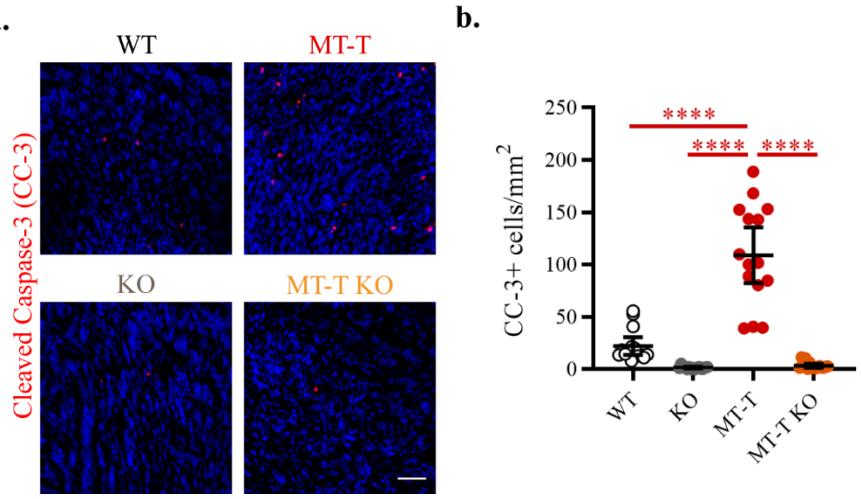

Figure 2.3: Global Bax knockout rescues GC cell death phenotype.
(a) Representative images of IHC staining for Cleaved Caspase-3 (CC-3) in the GCL. Scale bar is 50 µm.
(b) Quantification revealed the elevated density of CC-3+ cells in the GCL of MT-T animals is decreased in MT-T KO. 5 animals/genotype, 3 slices/animal. Bar and error represent mean with 95% confidence interval (CI). WT: 22.08, 13.77-30.39; KO: 1.47, 0.73-2.21; MT-T: 108.9, 82.27-135.5; and MT-T KO: 3.35, 1.48-5.22. One-way ANOVA followed by Tukey's multiple comparisons test. WT, KO, and MT-T KO vs MT-T, $p < 0.0001$. ****$p < 0.0001$.

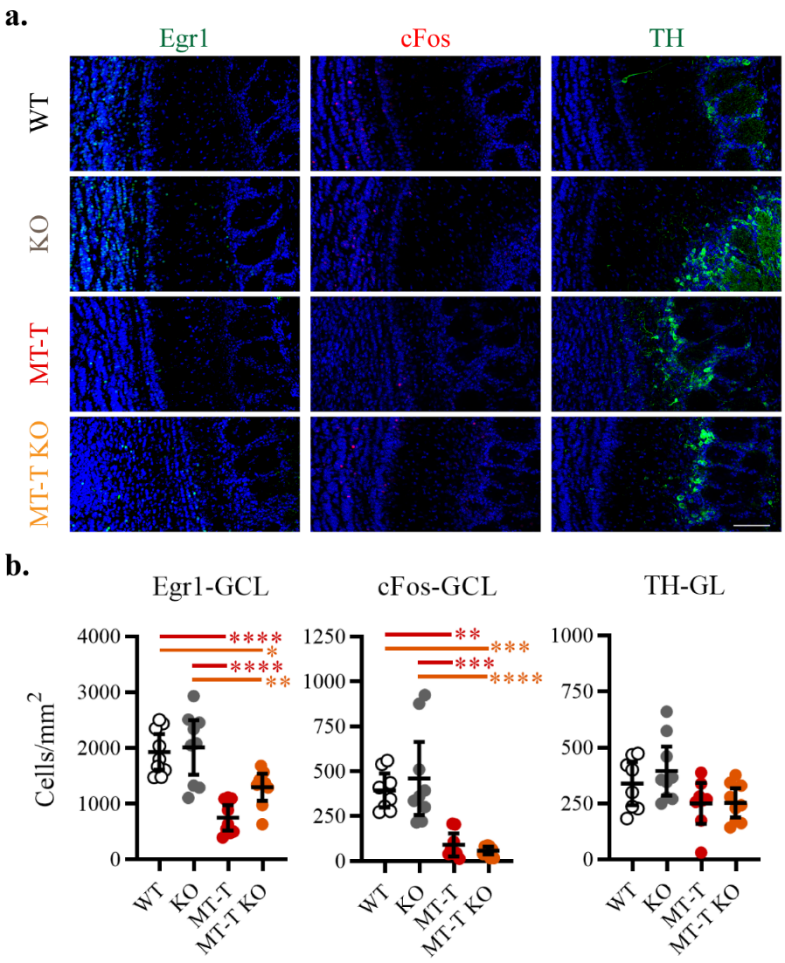

Figure 2.4: OB circuit activity is unaltered by Bax deletion.
(a) Representative images of IHC staining for Egr1 (GCL), cFos (GCL), and TH (GL). Scale bar is 100 μm.
(b) Quantifications revealed density of Egr1 and cFos remain significantly decreased in MT-T KO animals and TH density is unaltered. 3 animals/genotype, 2-3 slices/animal. Bar and error represent mean with 95% CI. Egr1: WT (9): 1928, 1608-2247; KO (9): 2009, 1522-2497; MT-T (9): 746.9, 519.3-974.6; and MT-T KO (9): 1293, 1051-1535. WT vs MT-T $p < 0.0001$, WT vs MT-T KO $p < 0.05$, KO vs MT-T $p < 0.0001$, KO vs MT-T KO $p < 0.05$. cFos: WT (8): 393.3, 298.7-488.0; KO (9): 460.1, 256.2-664.1; MT-T (8): 91.02, 27.50-154.4; and MT-T KO (9): 59.19, 38.0-80.39. WT vs MT-T $p = 0.0023$, WT vs MT-T KO $p = 0.0005$, KO vs MT-T $p = 0.001$, KO vs MT-T KO $p < 0.0001$. TH: WT (8): 338.7, 241.9-435.5; KO (9): 395.2, 285.9-504.6; MT-T (8): 250.1, 159.4-340.8; and MT-T KO (9): 253.2, 187.9-318.5. One-way ANOVA followed by Tukey's multiple comparisons test. *$p < 0.05$, **$p < 0.01$, ***$p < 0.001$, ****$p < 0.0001$.

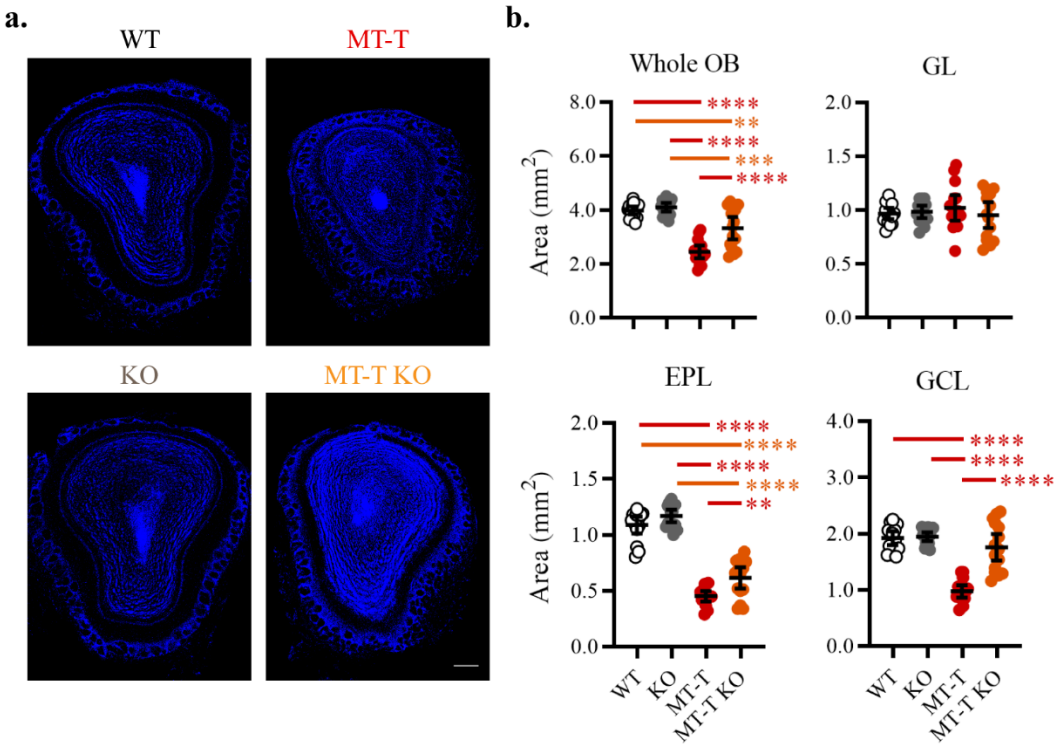

Figure 2.5: OB architecture is partially rescued in MT-T KO mice.
(a) Representative images of maximal coronal OB sections. Scale bar is 250 µm.
(b) Quantifications reveal the GCL is rescued in MT-T KO OBs, but the EPL and whole OB remain smaller than WT. 5 animals/genotype, 3 slices/animal. Bar and error represent mean with 95% CI. Whole OB: WT: 3.98, 3.83-4.13; KO: 4.1, 3.94-4.26; MT-T: 2.45, 2.21-2.68; and MT-T KO: 3.33, 2.91-3.74. WT vs MT-T $p < 0.0001$, WT vs MT-T KO $p = 0.0022$, KO vs MT-T $p < 0.0001$, KO vs MT-T KO $p = 0.0002$, MT-T vs MT-T KO $p < 0.0001$. GL: WT: 0.97, 9.2-1.02; KO: 0.98, 0.93-1.04; MT-T: 1.02, 0.90-1.14; and MT-T KO: 0.95, 0.83-1.07. EPL: WT: 1.09, 101-1.16; KO: 1.17, 1.11-1.23; MT-T: 0.45, 0.41-0.50; and MT-T KO: 0.62, 0.52-0.71. WT vs MT-T $p < 0.0001$, WT vs MT-T KO $p < 0.0001$, KO vs MT-T $p < 0.0001$, KO vs MT-T KO $p < 0.0001$, MT-T vs MT-T KO $p = 0.0048$. GCL: WT: 1.92, 1.80-2.04; KO: 1.95, 1.87-2.02; MT-T: 0.97, 0.86-1.08; MT-T KO: 1.76, 1.52-1.99. WT vs MT-T $p < 0.0001$, KO vs MT-T $p < 0.0001$, MT-T vs MT-T KO $p < 0.0001$. One-way ANOVA followed by Tukey's multiple comparisons test. *$p < 0.05$, **$p < 0.01$, ***$p < 0.001$, ****$p < 0.0001$.

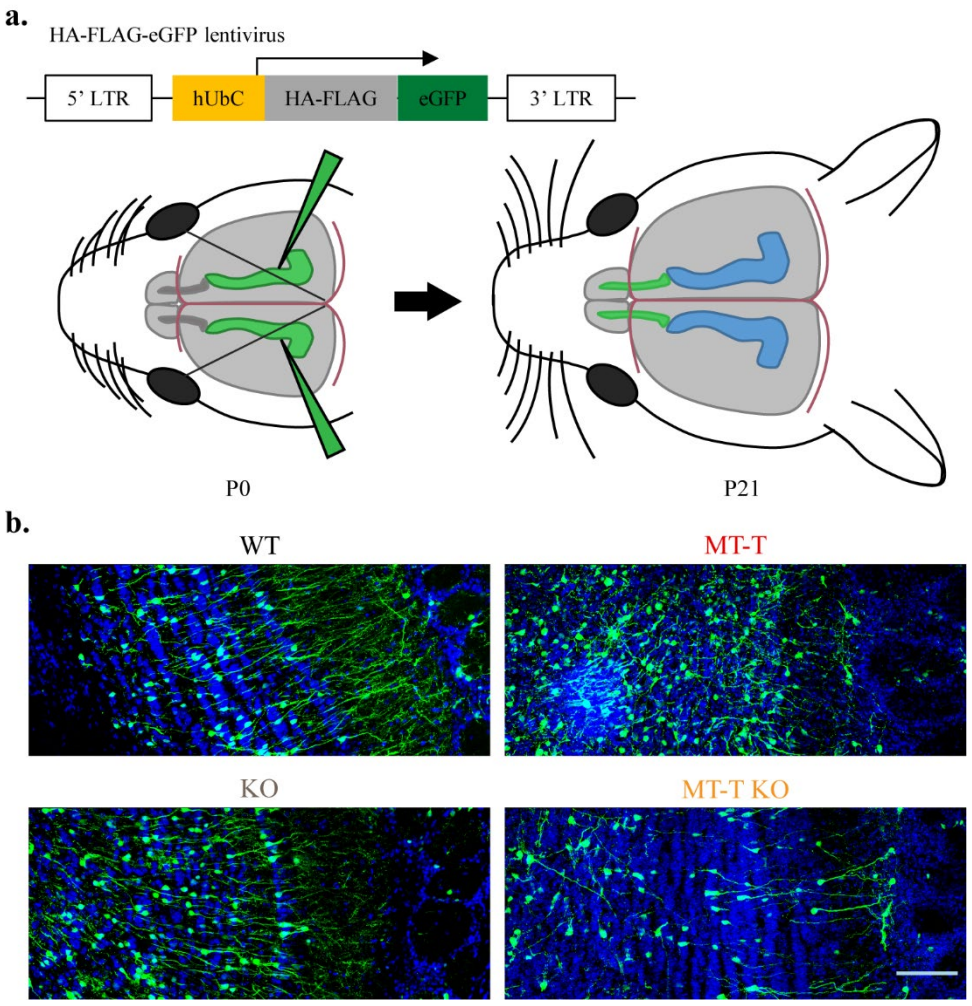

Figure 2.6: Intraventricular injection schematic to fluorescently-label newborn GCs.
(a) Lentivirus encoding HA-FLAG-eGFP under a human ubiquitin promoter is injected into both lateral ventricles of P0 pups to label progenitors lining the SVZ. As GCs are born, they migrate through the rostral migratory stream and populate the OB.
(b) Representative images of eGFP-labelled GCs in the OB of transgenic animals imaged at P21. Scale bar is 100 μm.

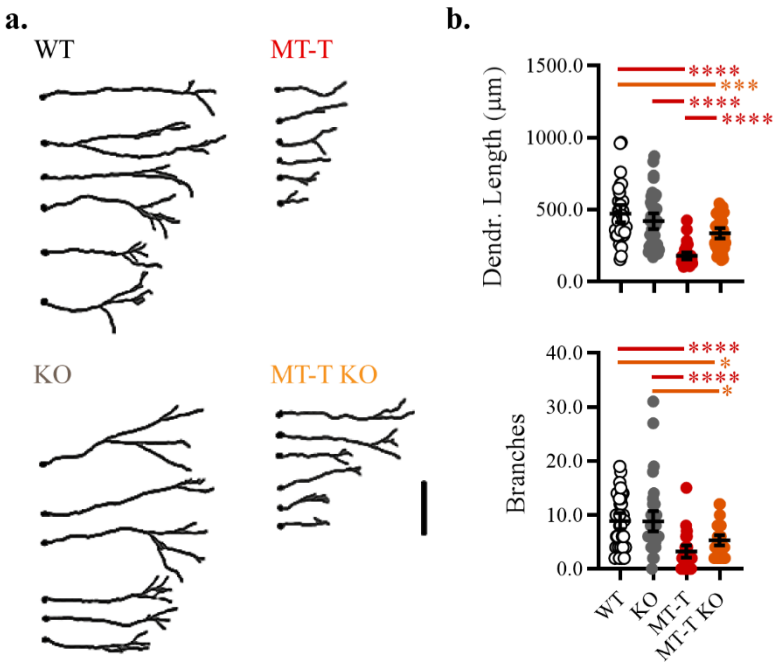

Figure 2.7: GCs in MT-T KO mice have longer dendrites than MT-T yet remain immature. (a) Representative reconstructions of GC apical dendrites. Scale bar is 100 µm. (b) Quantifications of the length and number of branches per apical dendrite demonstrate MT-T KO GCs have longer dendrites than MT-T but have simple branching patterns. 4 animals/genotype. Bar and error represent mean with 95% CI. Length: WT (40): 472.7, 412.6-532.7; KO (43): 420.2, 364.8-475.5; MT-T (34): 179, 154.7-203.3; MT-T KO (40): 336, 300.2-371.8. WT vs MT-T $p < 0.0001$, WT vs MT-T KO $p = 0.0004$, KO vs MT-T $p < 0.0001$, KO vs MT-T KO $p < 0.0001$. Branches: WT: 8.88, 7.39-10.36; KO: 8.81, 6.95-10.68; MT-T: 3.21, 2.08-4.33; and MT-T KO: 5.30, 4.36-6.25. WT vs MT-T $p < 0.0001$, WT vs MT-T KO $p = 0.0026$, KO vs MT-T $p < 0.0001$, KO vs MT-T KO $p = 0.0026$. One-way ANOVA followed by Tukey's multiple comparisons test. *$p < 0.05$, **$p < 0.01$, ***$p < 0.001$, ****$p < 0.0001$.

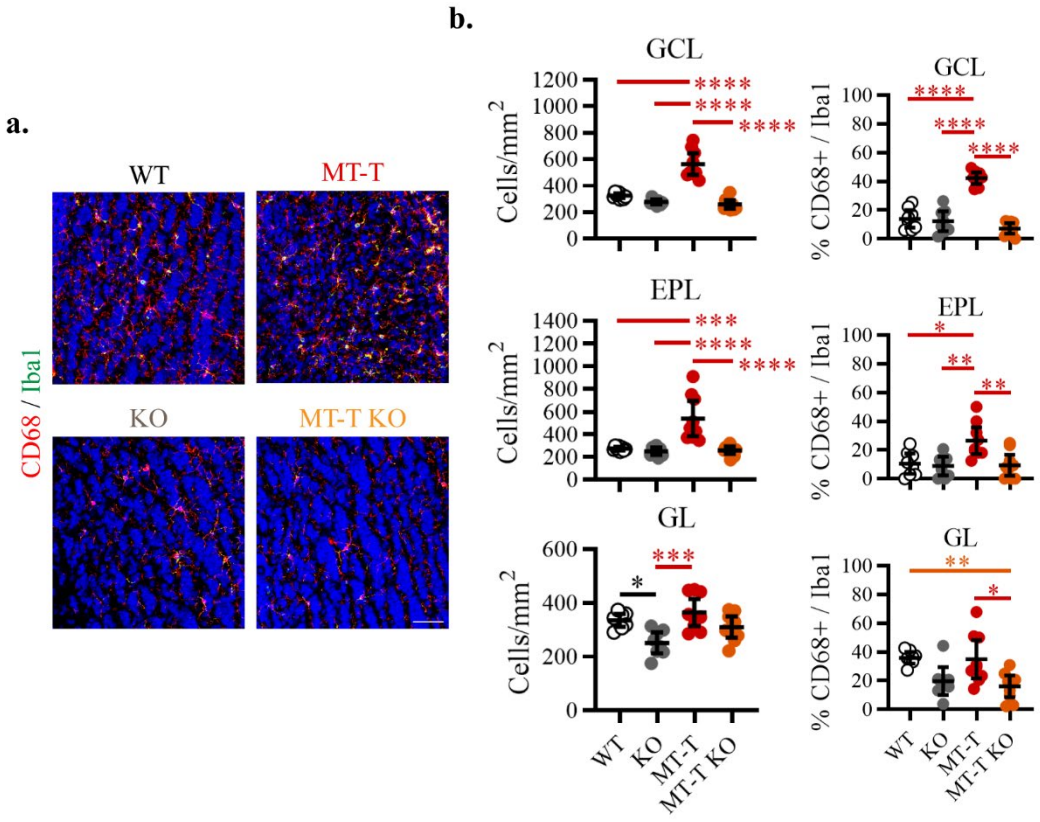

Figure 2.8: Microglia are recruited and active in MT-T OBs.
(a) Representative images of microglia stained for Iba1 and CD68 in the GCL of transgenic mice. Scale bar is 50 µm.
(b) Quantifications of microglia in different layers of the OB reveal microglia are specifically more active and dense in the GCL and EPL of MT-T animals. Bar and error represent mean with 95% CI. 3 animals/genotype, 2-3 slices/animal. Iba1-GCL: WT (8): 325.9, 308.7-343.1; KO (8): 279.4, 260.8-298; MT-T (9): 565, 482.8-647.2; MT-T KO (9): 259.2, 226.7-291.7. WT vs MT-T $p < 0.0001$, KO vs MT-T $p < 0.0001$, MT-T vs MT-T KO $p < 0.0001$. Iba1-EPL: WT: 275, 260-290; KO: 250.9, 218.4-283.3; MT-T: 539.7, 385.3-694; MT-T KO: 261.3, 227.6-294.9. WT vs MT-T $p = 0.0001$, KO vs MT-T $p < 0.0001$, MT-T vs MT-T KO $p < 0.0001$. Iba1-GL: WT: 335.5, 311.9-359.2; KO: 251.6, 212.2-291; MT-T: 364.7, 314-415.4; MT-T KO: 310.6, 271.1-350.2. WT vs KO $p = 0.0123$, KO vs MT-T $p = 0.0004$. CD68-GCL: WT: 13.98, 7.88-20.08; KO: 12.34, 5.38-19.3; MT-T: 42.3, 38.21-46.28; MT-T KO: 7.31, 3.66-10.96. WT vs MT-T $p < 0.0001$, KO vs MT-T $p < 0.0001$, MT-T vs MT-T KO $p < 0.0001$. CD68-EPL: WT: 10.49, 3.35-17.64; KO: 8.96, 2.44-15.48; MT-T: 26.48, 17.13-35.83; MT-T KO: 9.47, 2.14-16.8. WT vs MT-T $p = 0.0104$, KO vs MT-T $p = 0.0045$, MT-T vs MT-T KO $p = 0.0045$. CD68-GL: WT: 35.99, 31.95-40.03; KO: 19.74, 10.11-29.37; MT-T: 35.03, 21.62-48.44; MT-T KO: 16.15, 8.63-23.68. WT vs MT-T KO $p = 0.0095$, MT-T vs MT-T KO $p = 0.0112$. One-way ANOVA followed by Tukey's multiple comparisons test. *$p < 0.05$, **$p < 0.01$, ***$p < 0.001$, ****$p < 0.0001$.

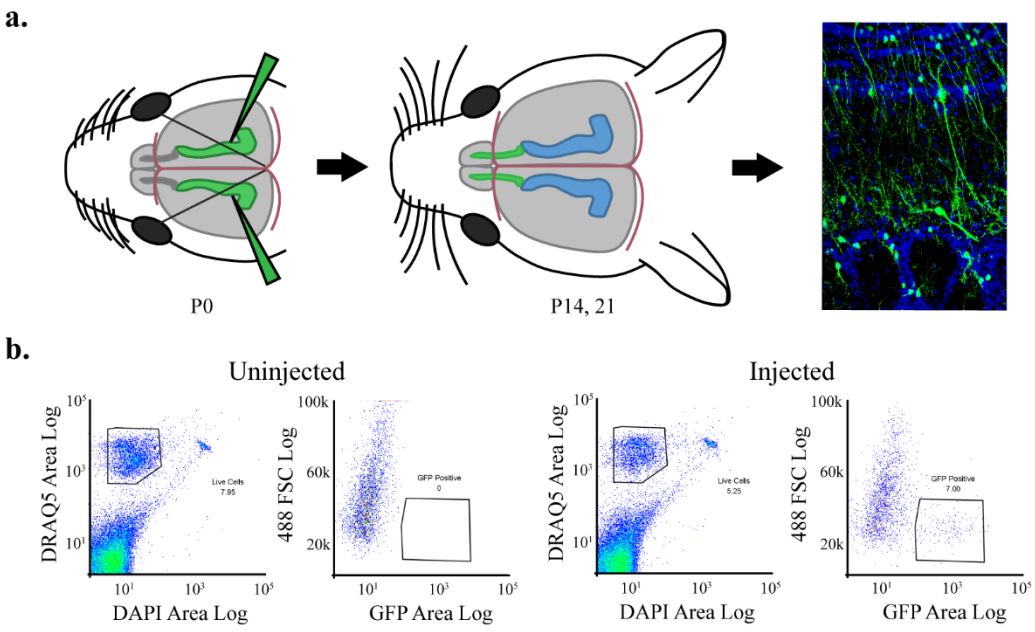

Figure 2.9: Schematic for GC isolation through intraventricular injection and FACS.
(a) Newborn GCs are labeled by injecting HA-FLAG-eGFP encoding lentivirus into the lateral ventricles of P0 pups and collected by dissection at either P14 or P21.
(b) FACS paradigm of dissociated OB samples to first isolate DAPI-/DRAQ5 positive cells (live cells) and then eGFP+ labeled cells (GFP Positive). Uninjected controls were used to draw sorting gates to isolate only eGFP+ cells. 40,000 events plotted/sample.

Table 2.1: Metadata of GC populations for RNA-Seq. Table of experimental information related to FACS, RNA extraction, cDNA library preparation, and sequencing depth for each sample.

sample name	genotype	biological replicate	age	sex	collection date	# of cells	pg/cell (RNA)	input RNA (ng)	input cDNA (ng)	mapped reads
WT.1.21	WT	1	21	M	4/29/2016	16455	5.08	2	7	27373748
WT.2.21	WT	2	21	F	5/5/2016	8942	5.82	2	7	36205237
WT.3.21	WT	3	21	M	6/10/2016	9946	1.62	2	7	36972623
KO.1.21	KO	1	21	M	4/29/2016	19199	3.03	2	7	31299038
KO.2.21	KO	2	21	F	5/11/2016	9220	1.85	2	7	44614265
KO.3.21	KO	3	21	F	6/14/2016	5317	1.54	2	7	41015516
MTT.1.21	MT-T	1	21	F	5/11/2016	6368	1.65	2	7	43901680
MTT.2.21	MT-T	2	21	F	5/31/2016	9081	1.74	2	7	36373291
MTT.3.21	MT-T	3	21	F	6/10/2016	5925	3.25	2	7	31402916
MTKO.1.21	MT-T KO	1	21	M	5/3/2016	8037	2.69	2	7	38610172
MTKO.2.21	MT-T KO	2	21	M	5/31/2016	23703	0.93	2	7	33355651
MTKO.3.21	MT-T KO	3	21	M	6/10/2016	8648	1.74	2	7	40183935
WT.1.14	WT	1	14	M	6/28/2016	8041	0.89	2	7	42742694
WT.2.14	WT	2	14	F	7/8/2016	16570	2.34	2	7	31130154
WT.3.14	WT	3	14	M	7/12/2016	13802	1.08	2	7	39874743
KO.1.14	KO	1	14	M	7/12/2016	14383	1.57	2	7	45923430
KO.2.14	KO	2	14	M	7/12/2016	5954	0.72	2	7	41651976
KO.3.14	KO	3	14	F	7/19/2016	4609	0.6	2	7	39691387
MTT.1.14	MT-T	1	14	M	7/8/2016	6363	1.84	2	7	57897798
MTT.2.14	MT-T	2	14	F	7/12/2016	6123	1.16	2	7	44638141
MTT.3.14	MT-T	3	14	F	7/12/2016	7679	1.2	2	7	41819786
MTKO.1.14	MT-T KO	1	14	M	7/12/2016	9272	0.77	2	7	47438257
MTKO.2.14	MT-T KO	2	14	M	7/12/2016	6365	0.68	2	7	36906783
MTKO.3.14	MT-T KO	3	14	M	7/8/2016	26345	1.69	2	7	39551592
					avg.	**10681.13**	**1.90**			**39607283.88**
					std. dev.	**5910.79**	**1.31**			**6460884.67**

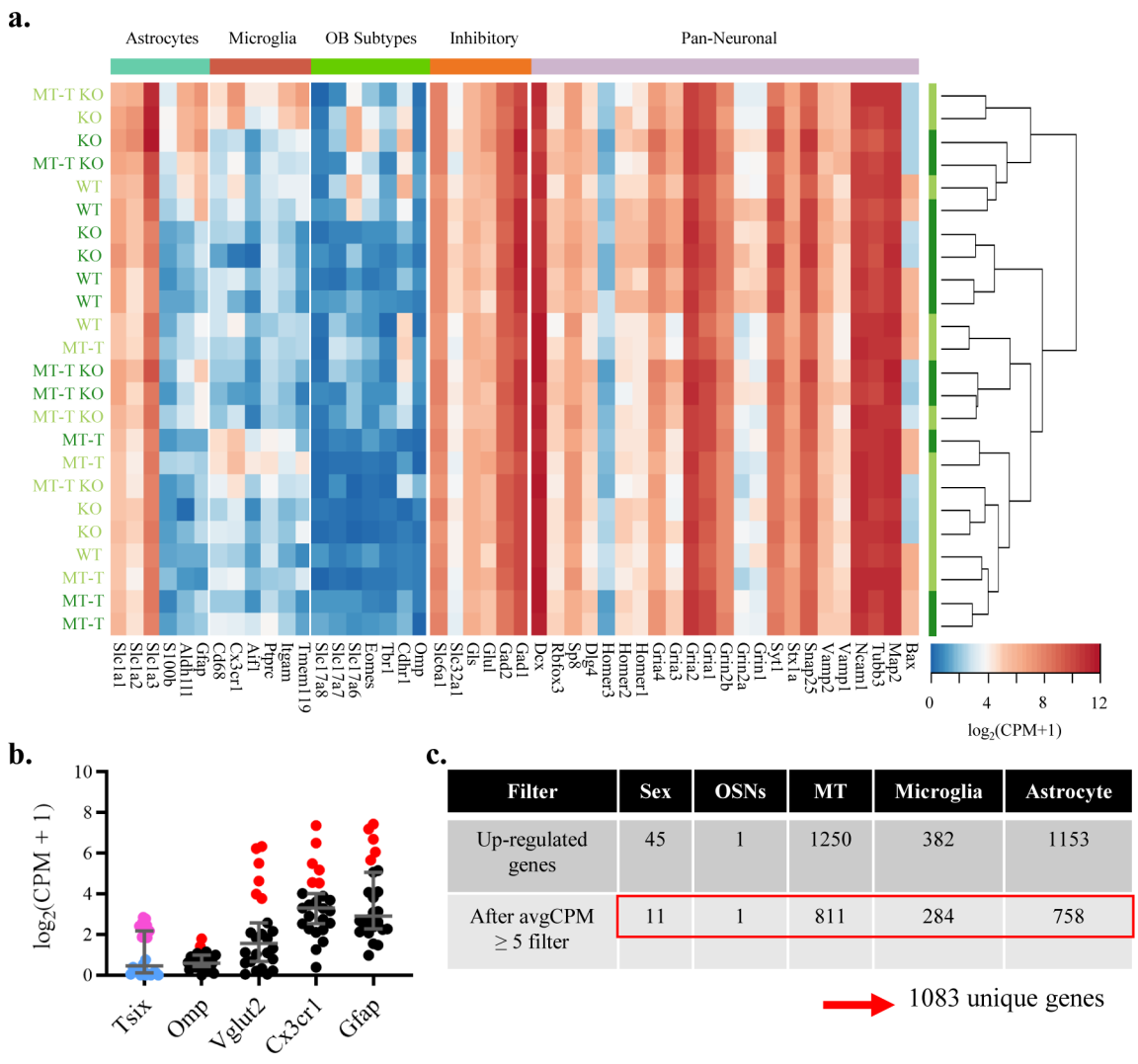

Filter	Sex	OSNs	MT	Microglia	Astrocyte
Up-regulated genes	45	1	1250	382	1153
After avgCPM ≥ 5 filter	11	1	811	284	758

Figure 2.10: Validation of RNA-Seq samples and identification of contaminating gene sets.
(a) Heatmap depicting normalized counts for expected genes in GCs and other OB cellular subtypes. Red indicates high normalized counts, whereas white or blue indicates below the filter threshold (CPM = 5). Hierarchical clustering of samples helps identify samples with similar sets of contaminating genes.
(b) Quantifications of expression values for highly expressed genes for each contaminating subtype. Bars and errors represent median with 95% CI. Tsix: 0.46, 0.12-2.18; Omp: 0.59, 0.43-0.99; VGlut2: 1.57, 0.68-2.58; Cx3cr1: 3.31, 2.53-4.02; Gfap: 2.91, 2.28-5.06. Red indicates samples higher than 95% CI. Blue indicates male and pink indicates female samples. 3 animals/genotype.
(c) Numbers of genes differentially expressed in samples identified with a contaminating gene subtype. Overlap comparison of all genes identified 1083 unique genes, which were removed for downstream analyses.

a.

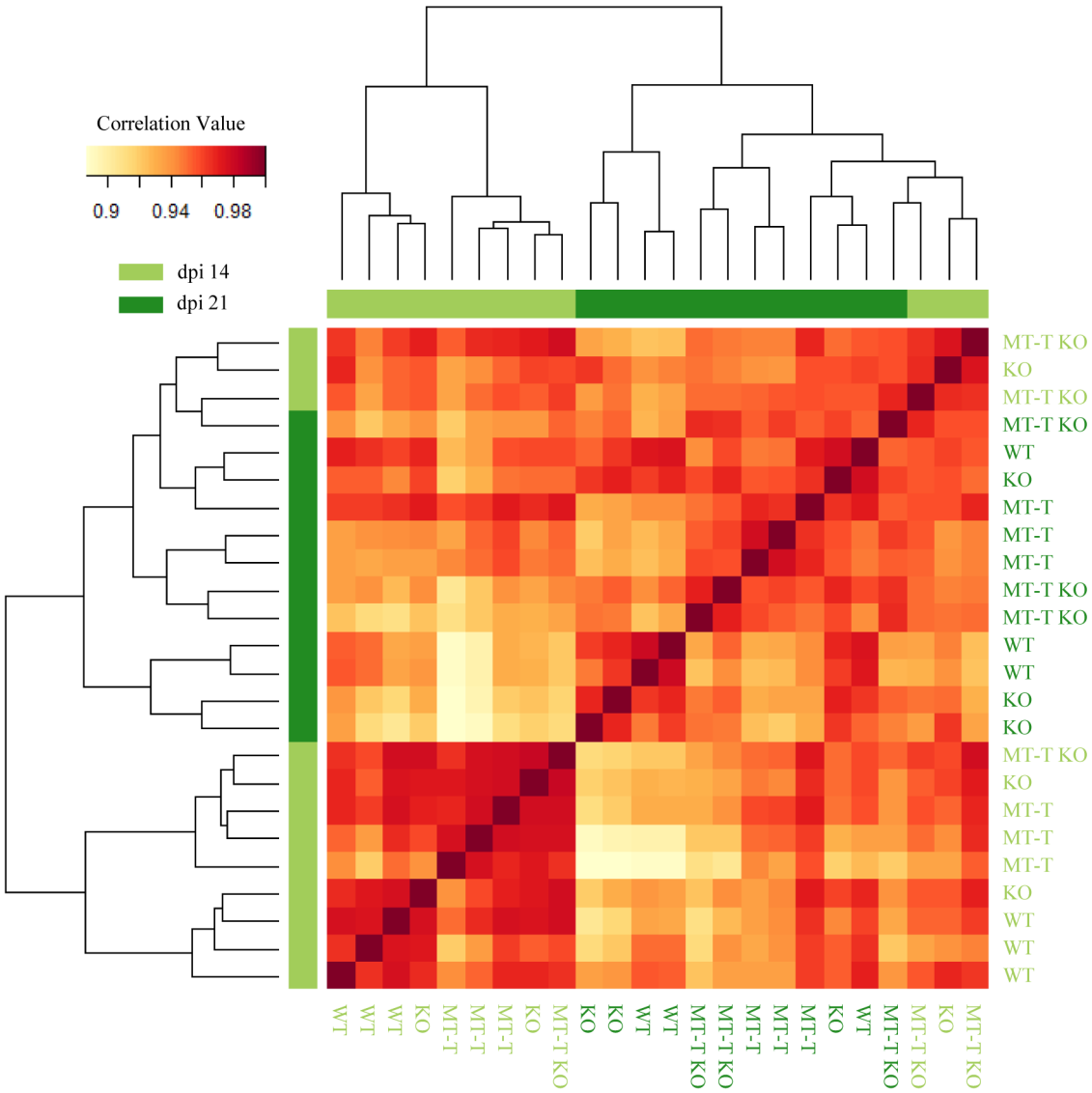

Figure 2.11: Correlation clustering separates GC samples by time point.
(a) Heatmap of correlation values with hierarchical clustering of related samples shows dpi 21 and dpi 14 samples mostly segregate. Red depicts stronger correlation values, light green shows dpi 14 samples and dark green labels dpi 21.

Figure 2.12: Principal Component Analysis generates four distinct clusters.
(a) Three-dimensional representation of top 3 PCs (PC1 31.45%; PC2 16.49%; PC3 9.4%) generated from PCA performed on filtered gene list separates samples into four main clusters. Large spheres represent centroid of individual samples.
(b) One-dimension plots of individual component PCs shows segregation of individual samples by each PC. PC1 shows separation based on time point. Dpi 14 samples are plotted over the axis and dpi 21 are under as indicated for PC1.
(c) Enriched GO-terms determined by Panther implicate cell migration and neuronal signaling processes for PC1 and PC3. Input gene lists contained the top 200 genes contributing to the positive side of the PC (green) and top 200 to the negative side (red). Data are presented as fold enrichment and the numbers listed are the total genes found in each GO-term as well as the significance value.

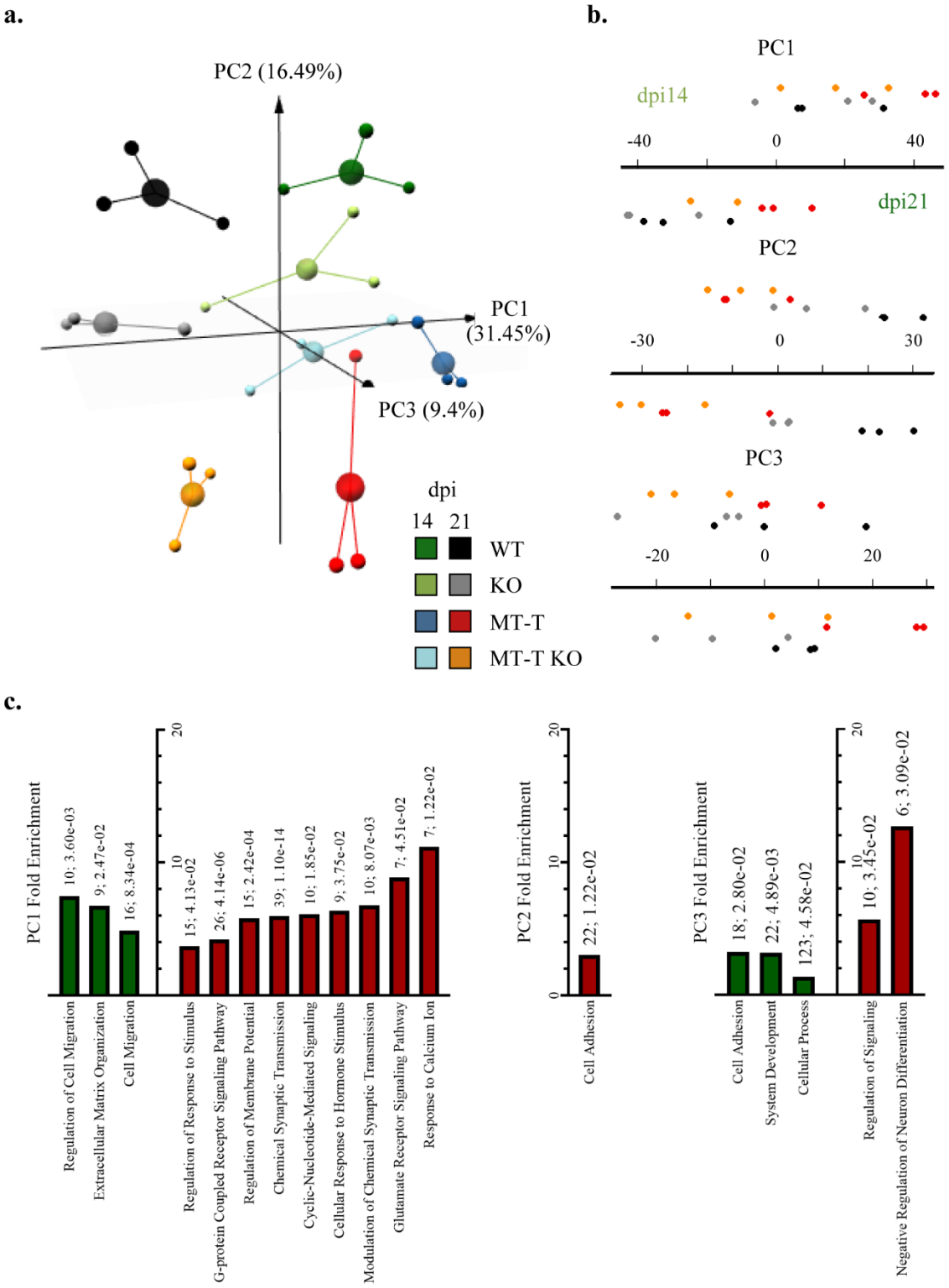
a.
PC2 (16.49%)
PC1
(31.45%)
PC3 (9.4%)
dpi
14 21
WT
KO
MT-T
MT-T KO
b.
PC1
dpi14
-40
0
40
dpi21
PC2
-30
0
30
PC3
-20
0
20
c.
PC1 Fold Enrichment
10; 3.60e-03
9; 2.47e-02
16; 8.34e-04
15; 4.13e-02
26; 4.14e-06
15; 2.42e-04
39; 1.10e-14
10; 1.85e-02
9; 3.75e-02
10; 8.07e-03
7; 4.51e-02
7; 1.22e-02
Regulation of Cell Migration
Extracellular Matrix Organization
Cell Migration
Regulation of Response to Stimulus
G-protein Coupled Receptor Signaling Pathway
Regulation of Membrane Potential
Chemical Synaptic Transmission
Cyclic-Nucleotide-Mediated Signaling
Cellular Response to Hormone Stimulus
Modulation of Chemical Synaptic Transmission
Glutamate Receptor Signaling Pathway
Response to Calcium Ion
PC2 Fold Enrichment
22; 1.22e-02
Cell Adhesion
PC3 Fold Enrichment
18; 2.80e-02
22; 4.89e-03
123; 4.58e-02
10; 3.45e-02
6; 3.09e-02
Cell Adhesion
System Development
Cellular Process
Regulation of Signaling
Negative Regulation of Neuron Differentiation

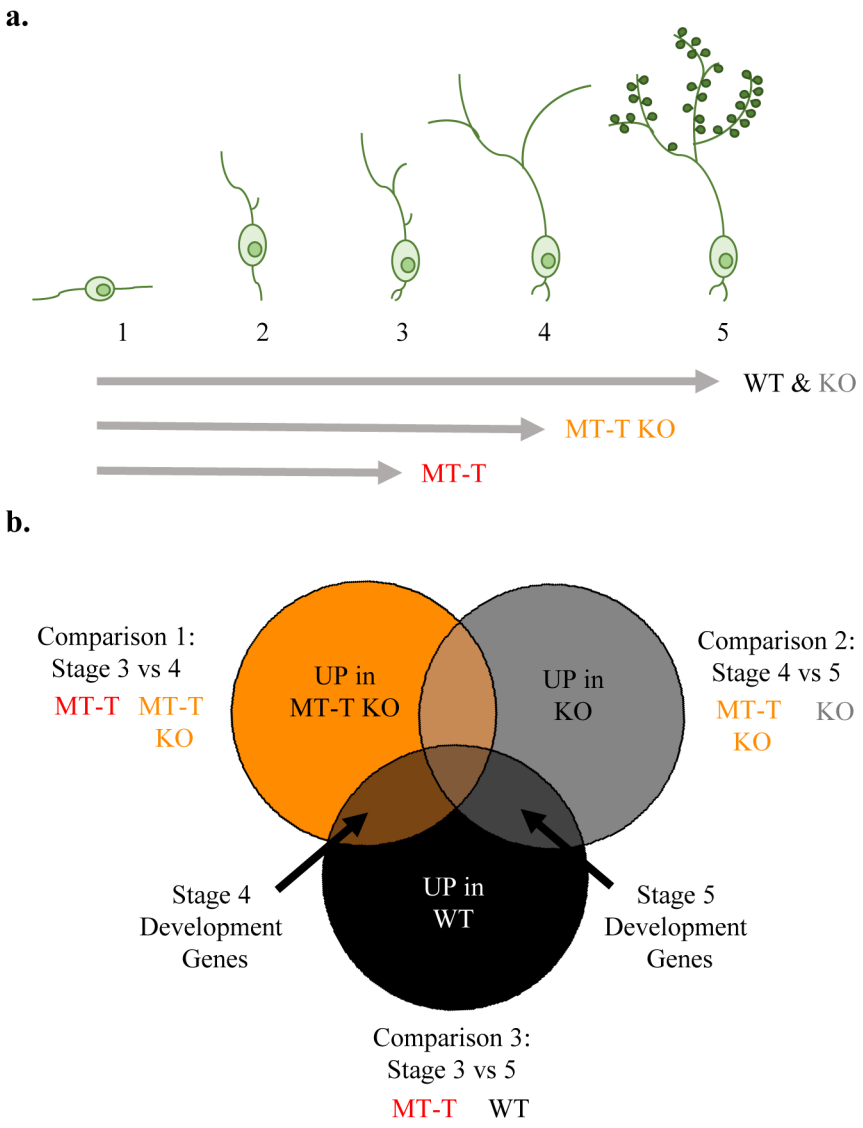

Figure 2.13: Model of GC development and overlap comparison analysis.
(a) Schematic of five described stages of GC development based on morphological features. Arrows and labels indicate hypothetical checkpoints where each genotype may pause in the absence of MT activity.
(b) Diagram of differential gene expression analyses for overlap analysis to identify checkpoint relevant gene sets.

Figure 2.14: Differential expression analysis implicates genes involved in GC developmental stages.
(a) Volcano plots depict differentially expressed genes. The blue dashed line indicates significance (p=0.05) and colored dots indicate in which genotype the gene is up-regulated. Listed numbers detail the number of significant genes on each side of the volcano.
(b) Overlap comparisons of genes up-regulated in more "mature" GC phenotypes for each comparison. These numbers are larger at dpi 21 as GCs reach more mature developmental stages.

a.

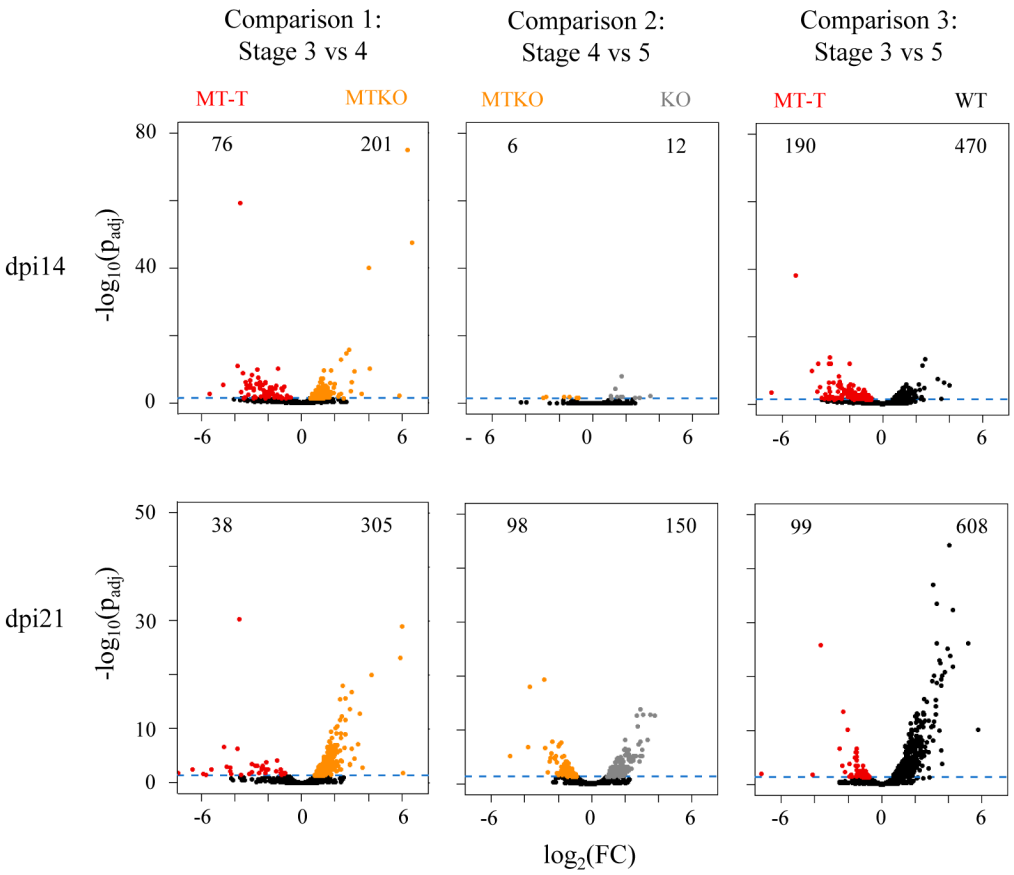
Comparison 1:
Stage 3 vs 4
Comparison 2:
Stage 4 vs 5
Comparison 3:
Stage 3 vs 5
MT-T
MTKO
MTKO
KO
MT-T
WT
dpi14
dpi21
-log10(padj)
76
201
6
12
190
470
38
305
98
150
99
608
log2(FC)

b.

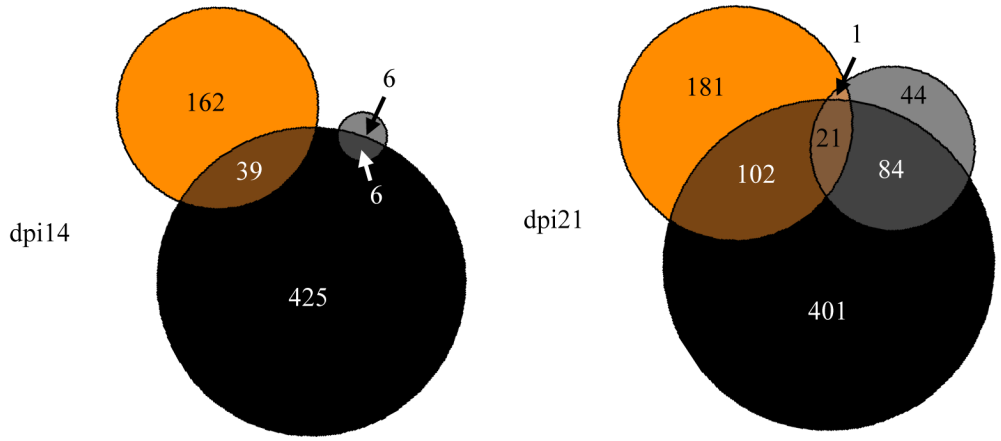
dpi14
162
39
6
6
425
dpi21
181
1
44
21
102
84
401

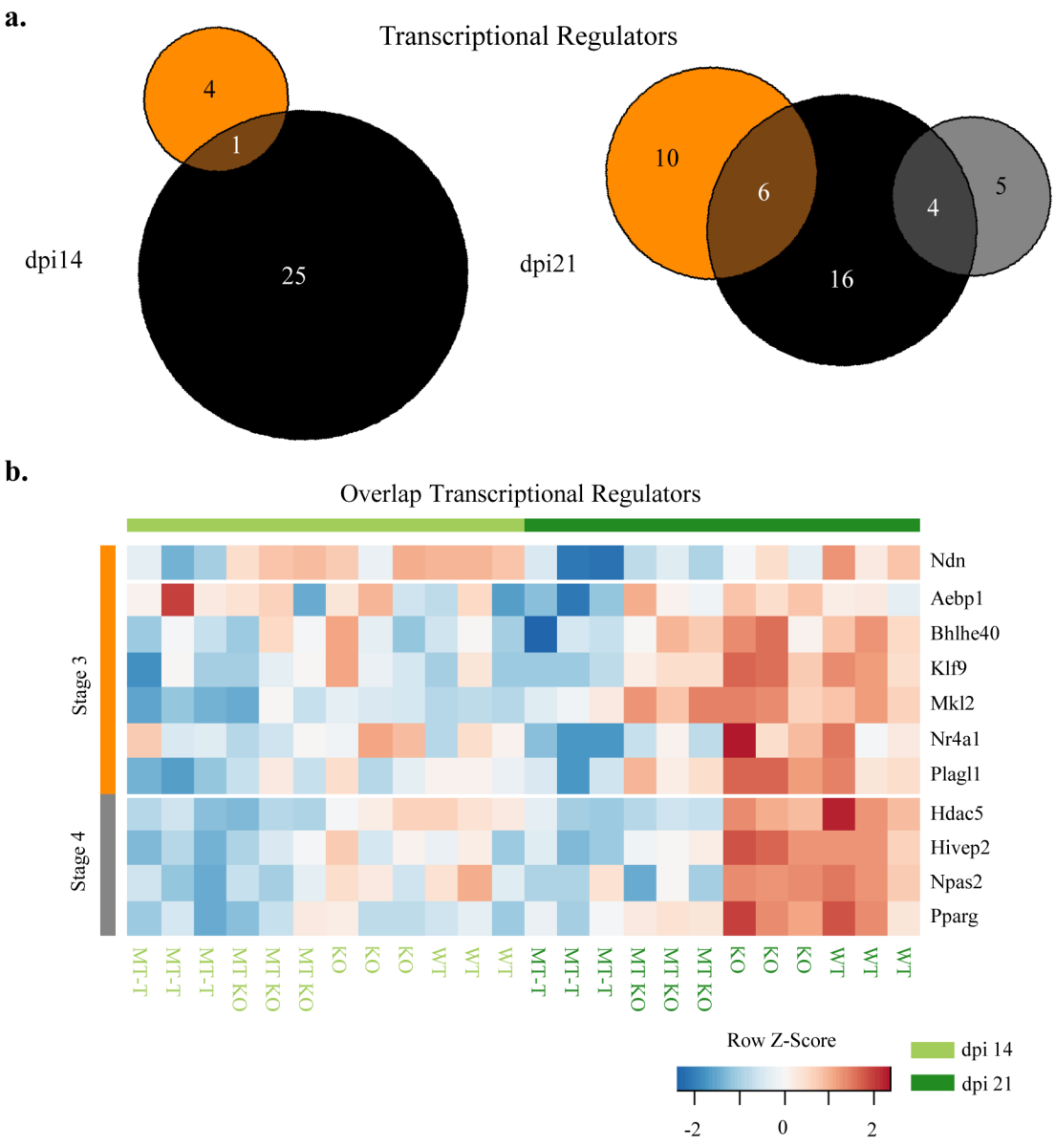

Figure 2.15: Identification of putative transcriptional regulators driving GC development.
(a) Overlap comparisons of transcriptional regulators from each comparison identified using a GO-term search.
(b) Heatmap of 11 overlapping transcriptional regulators showing comparative Z-scores across each sample. Red depicts higher Z-Score, which correlates to higher expression levels. Samples are organized by genotype and time point.

a.

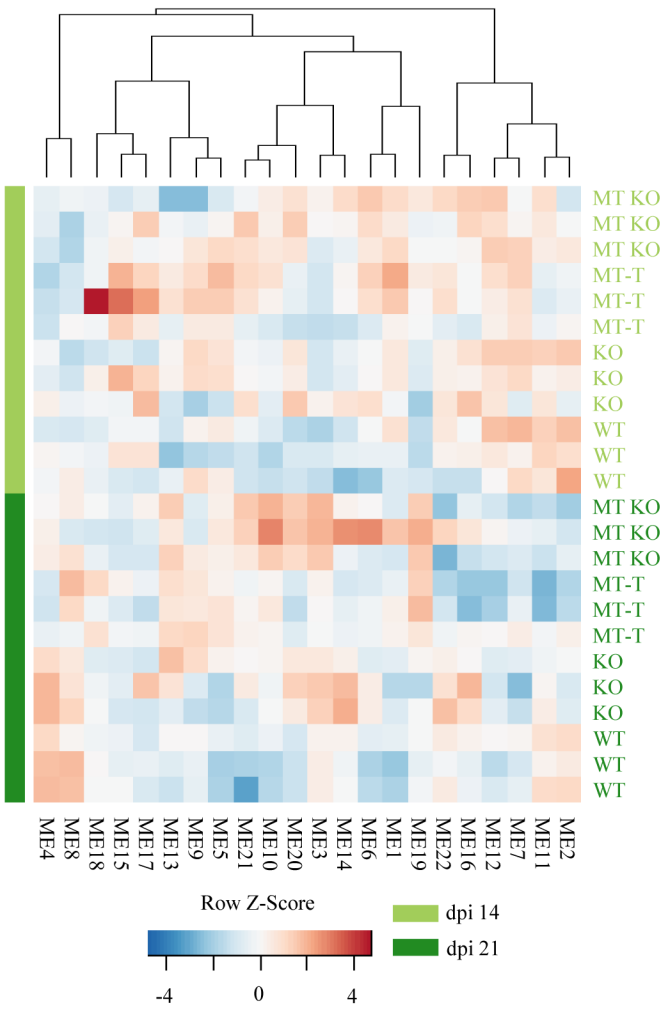

b.

ME	Gene #	Hub Genes
1	3055	Adh5, Cct3, Commd3, Atpif1, Nif3l1
2	2056	Mier2, Tmem183a, Anapc2, Dbn1, Chmp7
3	891	Faim2, Dpp10, Zbtb38, Scn2a1, Clstn3
4	880	Cckbr, Inpp5j, Pde2a, Hivep2, Pcdhgc5
5	834	Nfx1, Akap8, Ewsr1, Smpd4, Gtf3c2
6	408	Sar1b, Ankrd46, Tm2d2, Morf4l2, Aip
7	349	Brd3, Crmp1, Atat1, Pafah1b3, Nedd4l
8	340	AW822073, Pkhd1, Ttn, Gm38248, Gm37985
9	264	Fnbp4, Paxbp1, Dgat1, Gpc2, Mir124a-1hg
10	261	1500004A13Rik, Bbs4, Fbxo25, Armcx1, Zfp949
11	217	Oaz1, Rabac1, Mrpl43, Scg3, Txndc15
12	147	Mrpl52, Ap2s1, Romo1, 2700094K13Rik, Mrpl28
13	142	Srsf5, Snx32, Ddb2, Dpp7, Ino80dos
14	140	Atp6v1e1, Atp6v1d, Atp6ap2, Eno1, Prepl
15	125	Pcolce, Hcar1, Itih2, Col1a2, Serping1
16	69	1110001J03Rik, Ndufs7, Comt, Mdh2, Atp5a1
17	50	Cpq, Anxa5, Elovl1, Tcn2, Prelp
18	49	Gbp8, C3, Ccl8, Serpina3f, Gbp4
19	43	Abca8a, Frmd7, Cldn1, Grm8, Kif2a
20	41	Gm15545, Gm6394, Mcee, Ftl2-ps, Gm20746
21	40	Trim26, Tprkb, Tmem138, 2810001G20Rik, Tti2
22	37	Mgst3, Ndufb5, Tax1bp1, Fkbp3, Cycs

Figure 2.16: WGCNA builds phenotypically-relevant modules.
(a) Heatmap of 22 module eigengenes (ME) built by WGCNA showing comparative Z-scores across each sample. MEs show a variety of expression patterns including time-dependent and MT-activity dependent patterns. Red depicts higher Z-Score, which correlates to higher expression levels. Light green bars depict dpi 14 samples and dark green labels dpi 21.
(b) Table including the number of genes in each module as well as the 5 hub genes driving the formation of each module.

a.

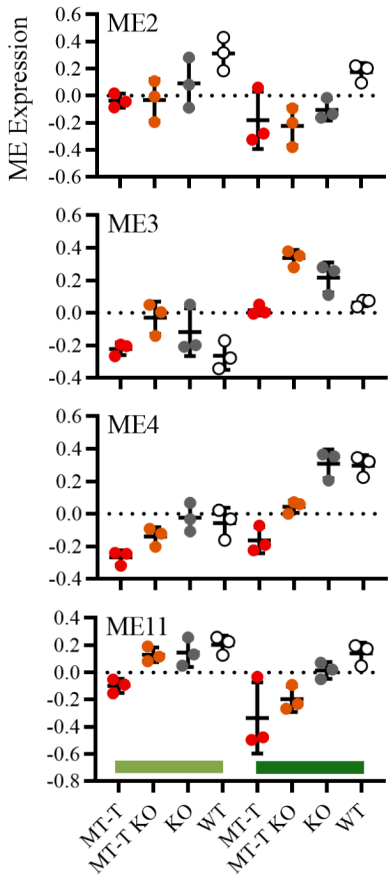

b.

Module	Hub Genes	GO-term
ME2	Mier2	Protein Folding (5.13E-03)
2056	Tmem183a	Proteolysis Involved in Cellular Protein Catabolic Process (5.00E-02)
	Anapc2	Intracellular Protein Transport (2.96E-03)
	Dbn1	Organelle Organization (2.23E-02)
	Chmp7	Transcription, DNA-templated (3.73E-03)
ME3	Faim2	Response to Calcium Ion (1.24E-02)
891	Dpp10	Glutamate Receptor Signaling (1.00E-02)
	Zbtb38	Cell Surface Receptor Signaling Pathway Involved in Cell-Cell Signaling (4.31E-03)
	Scn2a1	Synaptic Vesicle Exocytosis (3.44E-02)
	Clstn3	Modulation of Chemical Synaptic Transmission (2.22E-05)
ME4	Cckbr	Regulation of Exocytosis (3.38E-04)
880	Inpp5j	Synaptic Vesicle Exocytosis (4.24E-02)
	Pde2a	Organic Hydroxy Compound Transport (8.03E-03)
	Hivep2	Vesicle Fusion to Plasma Membrane (5.23E-04)
	Pcdhgc5	Signal Transduction (9.80E-03)
ME11	Oaz1	N/A
217	Rabac1	
	Mrpl43	
	Scg3	
	Txnde15	

Figure 2.17: Gene modules regulating GC development and maturation.
(a) Quantification of ME expression implicates 4 MEs with elevated expression in WT or KO GCs compared to MT-T. ME2, 4, and 5 show higher expression in WT compared to MT-T and MT-T KO, while ME 3 has elevated expression in MT-T KO. Light green bars depict dpi 14 samples and dark green labels dpi 21. 3 samples/genotype. Bars and error represent mean with SD. ME2: dpi 14 MT-T: -0.04 ± 0.05; MT-T KO; -0.03 ± 0.15; KO: 0.09 ± 0.19; WT: 0.31 ± 0.12; dpi 21 MT-T: -0.18 ± 0.21; MT-T KO: -0.22 ± 0.14; KO: -0.10 ± 0.08; WT: 0.17 ± 0.07. ME3: dpi 14 MT-T: -0.22 ± 0.04; MT-T KO: -0.03 ± 0.10; KO: -0.12 ± 0.15; WT: -0.26 ± 0.09; dpi 21 MT-T: 0.12 ± 0.03; MT-T KO: 0.34 ± 0.05; KO: 0.22 ± 0.09; WT: .06 ± 0.02. ME4: dpi 14 MT-T: -0.27 ± 0.04; MT-T KO: -0.14 ± 0.06; KO: -0.02 ± 0.09; WT: 0.06 ± 0.09; dpi 21 MT-T: -0.16 ± 0.08; MT-T KO: 0.04 ± 0.04; KO: 0.31 ± 0.09; WT: 0.30 ± 0.06. ME11: dpi 14 MT-T: -0.10 ± 0.05; MT-T KO: 0.13 ± 0.06; KO: 0.15 ± 0.11; WT: 0.20 ± 0.07; dpi 21 MT-T: -0.34 ± 0.26; MT-T KO: -0.20 ± 0.09; KO: 0.01 ± 0.06; WT: 0.14 ± 0.08.
(b) Table including the number of genes in each module, the 5 hub genes, and enriched GO-terms identified by Panther from the full module gene list.

References

Abraham, N.M., Egger, V., Shimshek, D.R., Renden, R., Fukunaga, I., Sprengel, R., Seeburg, P.H., Klugmann, M., Margrie, T.W., Schaefer, A.T., and Kuner, T. (2010). Synaptic inhibition in the olfactory bulb accelerates odor discrimination in mice. Neuron 65(3): 399–411.

Adnani, L, Langevin, L.M., Gautier, E., Dixit, R., Parsons, K., Li, S., Kaushik, G., Wilkinson, G., Wilson, R., Childs, S., Nguyen, M.D., Journot, L., Dehay, C., and Shuurmans, C. (2015). Zac1 regulates the differentiation and migration of neocortical neurons via Pac1. Journal of Neuroscience 35 (39): 13430–13447.

Alonso, M., Lepousez, G., Sebastien, W., Bardy, C., Gabellec, M.M., Torquet, N., and Lledo, P.M. (2012). Activation of adult-born neurons facilitates learning and memory. Nature Neuroscience 15(6): 897–904.

Anders, S., Pyl, P.T., and Huber, W. (2015). HTSeq—a Python framework to work with high-throughput sequencing data. Bioinformatics 31(2): 166–169.

Andrieu, D., Meziane, H., Marly, F., Angelats, C., Fernandez, P.A., and Muscatelli, F. (2006). Sensory deficits in Necdin deficient mice result from a loss of sensory neurons correlated with an increase of developmental programmed cell death. BMC Developmental Biology 6:56.

Antón-Bolaños, N., Sempere-Ferràndez, A., Guillamón-Vivancos, T., Martini, F.J., Pérez-Saiz, L., Gezelius, H., Filipchuk, A., Valdeolmillos, M., and López-Bendito, G. (2019). Prenatal activity from thalamic neurons governs the emergence of functional cortical maps in mice. Science 364(6444), 987–990.

Belluscio, L., Lodovichi, C., Feinstein, P., Mombaerts, P., and Katz, L.C. (2002). Odorant receptors instruct functional circuitry in the mouse olfactory bulb. Nature 419(6904): 296–300.

Besnard, A., Langberg, T., Levinson, S., Chu, D., Vicidomini, C., Scobie, K.N., Dwork, A.J., Arango, V., Rosoklija, G.B., Mann, J.J., Hen, R., Leonardo, E.D., Boldrini, M., and Sahay, A. (2018). Targeting Kruppel-like factor 9 in excitatory neurons protects against chronic stress-induced impairments in dendritic spines and fear responses. Cell Reports 23(11): 3183–3196.

Boland, M.J., Hazen, J.L., Nazor, K.L., Rodriguez, A.R., Gifford, W., Martin, G., Kupriyanov, S., and Baldwin, K.K. (2009). Adult mice generated from induced pluripotent stem cells. Nature 461(7260): 91–94.

Bolger, A.M., Lohse, M., and Usadel, B. (2014). Trimmomatic: a flexible trimmer for Illumina sequence data. Bioinformatics 30(15): 2114–20.

Bozza, T., Feinstein, P., Zheng, C., and Mombaerts, P. (2002). Odorant receptor expression defines functional units in the mouse olfactory system. Journal of Neuroscience 22(8): 3033–3043.

Breton-Provencher, V., Lemasson, M., Peralta III, M.R., and Saghatelyan, A. (2009). Interneurons produced in adulthood are required for the normal functioning of the olfactory bulb network and for the execution of selected olfactory behaviors. Journal of Neuroscience 29(48): 15245–15257.

Breton-Provencher, V., Coté, D., and Saghatelyan, A. (2014). Activity of the principal cells of the olfactory bulb promotes a structural dynamic on the distal dendrites of immature adult-born granule cells via activation of NMDA receptors. Journal of Neuroscience 34(5): 1748–1759.

Breton-Provencher, V., Bakhshetyan, K., Hardy, D., Bammann, R.R., Cavarretta, F., Snapyan, M., Côté, D., Migliore, M., and Saghatelyan, A. (2016). Principal cell activity induces spine relocation of adult-born interneurons in the olfactory bulb. Nature Communications 7: 12659.

Carleton, A., Petreanu, L.T., Lansford, R., Alvarez-Buylla, A., and Lledo, P.M. (2003). Becoming a new neuron in the adult olfactory bulb. Nature Neuroscience 6(5): 507–518.

Carlson, G.C., Shipley, M.T., and Keller, A. (2000). Long-lasting depolarizations in mitral cells of the rat olfactory bulb. Journal of Neuroscience 20(5): 2011–2021.

Carulli, D., Foscarin, S., and Rossi, F. (2011). Activity-dependent plasticity and gene expression modifications in the adult CNS. Frontiers in Molecular Neuroscience 4: 50.

Cecchi, G. A., Petreanu, L. T., Alvarez-Buylla, A. and Magnasco, M. O. (2001). Unsupervised learning and adaptation in a model of adult neurogenesis. Journal of Computational Neuroscience 11(2): 175–182.

Chaput, M.A., Buonviso, N., and Berthommier, F. (1992). Temporal patterns in spontaneous and odour-evoked mitral cell discharges recorded in anaesthetized freely breathing animals. European Journal of Neuroscience 4(9): 813–822.

Chen, W.R., and Shepherd, G.M. (1997). Membrane and synaptic properties of mitral cells in slices of rat olfactory bulb. Brain Research 745(1): 189–196.

Chen, Y., Wang, Y., Ertürk, A., Kallop, D., Jiang, Z., Weimer, R.M., Kaminker, J., and Sheng, M. (2014). Activity-induced Nr4a1 regulates spine density and distribution pattern of excitatory synapses in pyramidal neurons. Neuron 2(16): 431–443.

Chung, S.H., Marzban, H., Aldinger, K., Dixit, R., Millen, K., Schuurmans, C., and Hawkes, R. (2011). Zac1 plays a key role in the development of specific neuronal subsets in the mouse cerebellum. Neural Development 6: 25.

Dahlen, J.E., Jimenez, D.A., Gerkin, R.C., and Urban, N.N. (2011). Morphological analysis of activity-reduced adult-born neurons in the mouse olfactory bulb. Frontiers in Neuroscience 5:66.

DeBruyne, J.P., Weaver, D.R., and Reppert, S.M. (2007) Clock and Npas2 have overlapping roles in the suprachiasmatic circadian clock. Nature Neuroscience 10(5): 543–545.

Dobin, A., Davis, C.A., Schlesinger, F., Drenkow, J., Zaleski, C., Jha, S., Batut, P., Chaisson, M., and Gingeras, T.R. (2013). STAR: ultrafast universal RNA-seq aligner. Bioinformatics 29(1): 15–21.

Doetsch, F., and Alvarez-Buylla, A. (1996). Network of tangential pathways for neuronal migration in adult mammalian brain. PNAS 93(25): 14895–14900.

Gogos, J.A., Osborne, J., Nemes, A., Mendelsohn, M., and Axel, R. (2000). Genetic ablation and restoration of the olfactory topographic map. Cell 103(4): 609–620.

Graham, F.L., and van der Eb, A.J. (1973). A new technique for the assay of infectivity of human adenovirus 5 DNA. Virology 52(2): 456–467.

Hamilton, K.A., Wang, Y., Raefsky, S.M., Berkowitz, S., Spangler, R., Suire, C.N., Camandola, S., Lipsky, R.H., and Mattson, M.P. (2018) Mice lacking the transcriptional regulator Bhlhe40 have enhanced neuronal excitability and impaired synaptic plasticity in the hippocampus. PLoS One 13(5): e0196223.

Huaiyu, M., Muruganujan, A., Ebert, D., Huang, X., and Thomas, P.D. (2018). PANTHER version 14: more genomes, a new PANTHER GO-slim and improvements in enrichment analysis tools. Nucleic Acids Research 47(D1): 419–426.

James, K.N. (2013). Static and dynamic aspects of olfactory processing circuits. University of California, San Diego: PhD dissertation.

Kaneda, M., Sakagami, H., Hida, Y., Ohtsuka, T., Satou, N., Ishibashi, Y., Fukuchi, M., Krysiak, A., Ishikawa, M., Ihara, D., Kalita, K., and Tabuchi, A. (2018). Synaptic localisation of SRF coactivators, Mkl1 and Mkl2, and their role in dendritic spine morphology. Scientific Reports 8; 727.

Knudson, C.M., Tung, K.S., Tourtellotte, W.G., Brown, G.A., and Korsmeyer, S.J. (1995). Bax-deficient mice with lymphoid hyperplasia and male germ cell death. Science 270(5233): 96–99.

Kurita, M., Kuwajima, T., Nishimura, I., and Yoshikawa, K. (2006). Necdin downregulates Cdc2 expression to attenuate neuronal apoptosis. Journal of Neuroscience 26(46): 12003–12013.

Kuwajima, T., Nishimura, I., and Yoshikawa, K. (2006). Necdin promotes GABAergic neuron differentiation in cooperation with Dlx homeodomain proteins. Journal of Neuroscience 26(20): 5383–5392.

Langfelder, P., and Horvath, S. (2008). WGCNA: an R package for weighted correlation network analysis. BMC Bioinformatics 9:559.

Ledderose, J., Dieter, S., and Schwarz, M.K. (2013). Maturation of postnatally generated olfactory bulb granule cells depends on functional γ-protocadherin expression. Scientific Reports 3: 1514.

Leighton, A.H., and Lohmann, C. (2016). The wiring of developing sensory circuits - from patterned spontaneous activity to synaptic plasticity mechanisms. Frontiers in Neural Circuits 10: 71.

Li, Q., and Barres, B.A. (2018). Microglia and macrophages in brain homeostasis and disease. Nature Reviews Immunology 18(4): 225–242.

Lledo, P.M., and Valley, M. (2016). Adult olfactory bulb neurogenesis. Cold Spring Harbor Perspectives in Biology 8(8): a018945.

Love, M.I., Huber, W., and Anders, S. (2014). Moderated estimation of fold change and dispersion for RNA-seq data with DESeq2. Genome Biology 15(12): 550.

Luo, J., Chen, X., Pan, Y.W., Lu, S., Xia, Z., and Storm, D.R. (2015). The type 3 adenylyl cyclase is required for the survival and maturation of newly generated granule cells in the olfactory bulb. PLoS One 10(3): e0122057.

Majdalawieh, A., and Ro, H.S. (2010). Regulation of IκBα function and NF-κB signaling: Aebp1 is a novel proinflammatory mediator in macrophages. Mediators of Inflammation 2010: 823821.

McLean, J.H., and Shipley, M.T. (1988) Postmitotic, postmigrational expression of tyrosine hydroxylase in olfactory bulb dopaminergic neurons. Journal of Neuroscience 8(10): 3658–3669.

Moore, D.R., and Kitzes, L.M. (1985). Projections from the cochlear nucleus to the inferior colliculus in normal and neonatally cochlea-ablated gerbils. Journal of Comparative Neurology 240(2): 180–195.

Najbauer, J., and Leon, M. (1995). Olfactory experience modulates apoptosis in the developing olfactory bulb. Brain Research 674(1995): 245–251.

Nakao, A., Miyazaki, N., Ohira, K., Hagihara, H., Takagi, T., Usuda, N., Ishii, S., Murata, K., and Miyakawa, T. (2017). Immature morphological properties in subcellular-scale structures in the dentate gyrus of Schnurri-2 knockout mice: a model for schizophrenia and intellectual disability. Molecular Brain 10: 60.

Nicoll, R.A. (1969). Inhibitory mechanisms in the rabbit olfactory bulb: dendrodendritic mechanisms. Brain Research 14(1): 157–172.

Nissant, A., Bardy, C., Katagiri, H., Murray, K., and Lledo, P.M. (2009). Adult neurogenesis promotes synaptic plasticity in the olfactory bulb. Nature Neuroscience 12(6): 728–730.

Pan ,Y., and Monje, M. (2020). Activity shapes neural circuit form and function: a historical perspective. Journal of Neuroscience 40(5): 944–954.

Perego, C., Fumagalli, S., De Simoni, M.G. (2011). Temporal pattern of expression and colocalization of microglia/macrophage phenotype markers following brain ischemic injury in mice. Journal of Neuroinflammation 8:174.

Petreanu, L., and Alvarez-Buylla, A. (2002). Maturation and death of adult-born olfactory bulb granule neurons: role of olfaction. Journal of Neuroscience 22(14): 6106–6113.

Rall, W., Shepherd, G.M., Reese, T.S., and Brightman, M.W. (1966). Dendrodendritic synaptic pathway for inhibition in the olfactory bulb. Experimental Neurology 14(1): 44–56.

Rosenberg, S.S., and Spitzer, N.C. (2011). Calcium signaling in neuronal development. Cold Spring Harbor Perspectives in Biology 3(10): a004259.

Saghatelyan, A., Roux, P., Migliore, M., Rochefort, C., Desmaisons, D., Charneau, P., Shepherd, G.M., and Lledo, P.M. (2005). Activity-dependent adjustments of the inhibitory network in the olfactory bulb following early postnatal deprivation. Neuron 46(1): 103–116.

Sando III, R., Gounko, N., Pieraut, S., Liao, L., Yates III, J. and Maximov, A. (2012). Hdac4 governs a transcriptional program essential for synaptic plasticity and memory. Cell 151(4): 821–834.

Schneider, S.P., and Scott, J.W. (1983). Orthodromic response properties of rat olfactory bulb mitral and tufted cells correlate with their projection patterns. Journal of Neurophysiology 50(2): 358–378.

Schoppa, N.E., and Westbrook, G.L. (2001). Glomerulus-specific synchronization of mitral cells in the olfactory bulb. Neuron 31(4): 639–651.

Scott, J.W. (1981). Electrophysiological identification of mitral and tufted cells and distributions of their axons in olfactory system of the rat. Journal of Neurophysiology 46(5): 918–931.

Shatz, C.J., and Stryker, M.P. (1988). Prenatal tetrodotoxin infusion blocks segregation of retinogeniculate afferents. Science 242(4875): 87–89.

Shijo, M., Honda, H., Suzuki, S.O., Hamasaki, H., Hokama, M., Abolhassani, N., Nakabeppu, Y., Ninomiya, T., Kitazono, T., Iwaki, T. (2018). Association of adipocyte enhancer-binding protein 1 with Alzheimer's disease pathology in human hippocampi. Brain Pathology 28(1): 58–71.

Sohal, V.S., and Rubenstein, J.L.R. (2019). Excitation-inhibition as a framework for investigating mechanisms in neuropsychiatric disorders. Molecular Psychiatry 24(11): 1248–1257.

Sowa, M.E., Bennett, E.J., Gygi, S.P., and Harper, J.W. (2009). Defining the human deubiquitinating enzyme interaction landscape. Cell 138(2): 389–403.

Sretavan, D.W., Shatz, C.J., and Stryker, M.P. (1988). Modification of retinal ganglion cell axon morphology by prenatal infusion of tetrodotoxin. Nature 336(6198): 468–471.

Srivastava, S., Engels, H., Schanze, I., Cremer, K., Wieland, T., Menzel, Schubach, M., Biskup, S., Kreiß, M., Endele, S., Strom, T.M., Wieczorek, D., Zenker, M., Gupta, S., Cohen, J., Zink, A.M., and Naidu, S. (2015). Loss-of-function variants in Hivep2 are a cause of intellectual disability. European Journal of Human Genetics 24: 556–561.

Tan, J., Savinger, A., Ma, M., and Luo, M. (2010). Odor information processing by the olfactory bulb analyzed in gene-targeted mice. Neuron 65(6): 912–926.

Taniguchi, M., Carreira, M.B., Cooper, Y.A., Bobadilla, A.C., Heinsbroek, J.A., Koike, N., Larson, E.B., Balmuth, E.A., Hughes, B.W., Penrod, R.D., Kumar, J., Smith, L.N., Guzman, D., Takahashi, J.S., Kim, T.K., Kalivas, P.W., Self, D.W., Lin, Y., and Cowan, C.W. (2017). Hdac5 and its target gene, Npas4, function in the nucleus accumbens to regulate cocaine-conditioned behaviors. Neuron 96(1): 130–144.

Tepe, B., Hill, M.C., Pekarek, B.T., Hunt, P.J., Martin, T.J., Martin, J.F., and Arenkiel, B.R. (2018). Single-cell RNA-seq of mouse olfactory bulb reveals cellular heterogeneity and activity-dependent molecular census of adult-born neurons. Cell Reports 25(10): 2689–2703.

Tseng, C.S., Chao, H.W., Huang, H.S., and Huang, Y.S. (2017). Olfactory-experience and developmental-stage-dependent control of CPEB4 regulates c-*Fos* mRNA translation for granule cell survival. Cell Reports 21(8): 2264–2276.

Tsunemoto, R., Lee, S., Szũcs, A., Chubukov, P., Sokolova, I., Blanchard, J.W., Eade, K.T., Bruggemann, J., Wu, C., Torkamani, A., Sanna, P.P., and Baldwin, K.K. (2018) Diverse reprogramming codes for neuronal identity. Nature 557(7705): 375–380

Verhage, M., Maia, A.S., Plomp, J.J., Brussaard, A.B., Heeroma, J.H., Vermeer, H., Toonen, R.F., Hammer, R.E., van den Berg, T.K., Missler, M., Geuze, H.J., and Südhof, T.C. (2000). Synaptic assembly of the brain in the absence of neurotransmitter secretion. Science 287(5454): 864–869.

Warden, A., Truitt, J., Merriman, M., Ponomareva, O., Jameson, K., Ferguson, L.B., Mayfield, R.D., and Harris, R.A. (2016). Localization of PPAR isotypes in the adult mouse and human brain. Scientific Reports 6: 27618.

West, A.E., CHen, W.G., Dalva, M., Dolmetsch, R.E., Kornhauser, J.M., Shaywitz, A.J., Takasu, M.A., Tao, X., and Greenberg, M.E. (2001). Calcium regulation of neuronal gene expression. PNAS 98(20): 11024–11031.

Whitman, M.C., and Greer, C.A. (2007). Synaptic integration of adult-generated olfactory bulb granule cells: basal axodendritic centrifugal input precedes apical dendrodendritic local circuits. Journal of Neuroscience 27(37): 9951–9961.

Yang, Y., Coleman, M., Zhang, L., Zheng, X., and Yue, Z. (2013). Autophagy in axonal and dendritic development. Trends in Neuroscience 36(7): 418–428.

Yap, E.L., and Greenberg, M.E. (2018). Activity-regulated transcription: bridging the gap between neural activity and behavior. Neuron 100(2): 330–348.

Yoshihara, S., Takahashi, H., Nishimura, N., Kinoshita, M., Asahina, R., Kitsuki, M., Tatsumi, K., Furukawa-Hibi, Y., Hirai, H., Nagai, T., Yamada, K., and Tsuboi, A. (2014). Npas4 regulates Mdm2 and thus Dcx in experience-dependent dendritic spine development of newborn olfactory bulb interneurons. Cell Reports 8(3): 843–857.

Young, J.M., Friedman, C., Williams, E.M., Ross, J.A., Tonnes-Priddy, L., and Trask, B.J. (2002). Different evolutionary processes shaped the mouse and human olfactory receptor gene families. Human Molecular Genetics 11(5): 535–546.

Yu, C.R., Power, J., Barnea, G., O'Donnell, S., Brown, H.E.V., Osborne, J., Axel, R., and Gogos, J.A. (2004). Spontaneous neural activity is required for the establishment and maintenance of the olfactory sensory map. Neuron 42(4): 553–566.

Zhang, B., and Horvath, S. (2005). A general framework for weighted gene co-expression network analysis. Statistical Applications in Genetics and Molecular Biology 4(1).

Zhang, X., and Firestein, S. (2002). The olfactory receptor gene superfamily of the mouse. Nature Neuroscience 5(2): 124–133.

Zhou, S., and Yu, Y. (2018). Synaptic E-I balance underlies efficient neural coding. Frontiers in Neuroscience 12: 46.

Zhu, Y., Huang, M., Bushong, E., Phan, S., Uytiepo, M., Beutter, E., Boemer, D., Tsui, K., Ellisman, M., and Maximov, A. (2019). Class IIa Hdacs regulate learning and memory through dynamic experience-dependent repression of transcription. Nature Communications 10(1): 3469.

Chapter 3: Interspecies brain complementation in rat-mouse chimeras

Summary:

Evolution has sculpted brain development to enable the precise assembly of diverse cellular subtypes into neural circuits with species-specific functions. The extent to which neurons can recognize and engage with unfamiliar forms of information though is poorly understood. Here we have tested the flexibility of neurons from species separated by ~12-24 million years of evolution to contribute to neural circuits by injecting rat pluripotent stem cells into mouse blastocysts to produce mice harboring rat neurons. These interspecies rat-mouse brain complementation experiments show that rat neurons contribute broadly to the mouse brain and reprogram their developmental timeline to match that of their host. Light-activation of rat neurons drives responses in mouse cells demonstrating their functional integration into mouse circuits. In animals with specific neuronal subtypes genetically-eliminated, we identify species barriers to full reconstitution, which can be surmounted using an alternative, genetic-silencing approach. Furthermore, information from rat sensory neurons travels through multiple synapses to shape cortical activity. By quantifying the neural circuits to which neurons of other species can and cannot contribute, and clarifying the rules by which they integrate, these studies establish interspecies chimeras as a method to understand mechanisms of neuronal circuit development and plasticity that will inform transplantation efforts in regenerative medicine.

Introduction:

Brain development is a complex process where neurons must balance intrinsic, genetic programs with extrinsic, environmental cues in order to build diverse and intricate neuronal circuits. Early experiments utilized grafting methods to transplant differentiating neural tissues and model development in intact organisms (Balaban et al., 1988; Constantine-Paton et al., 1975). More recently, transplant studies focus on pluripotent stem cell (PSC)-derived neurons and organoids (Espuny-Camacho et al., 2013; Falkner et al., 2016; Mansour et al. 2018). Whereas these methods help assess the flexibility within developing neurons by maintaining relevant spatial cues, they require already differentiated cells or tissues, and are inherently injury models that activate the host system's immune response unless immune-deficient animals are used. Reductionist approaches to model specification and development *in vitro* using cultured neurons, PSC-derived neurons, or PSC-derived brain organoids are readily accessible to genetic-modifications but lack the physiological environmental cues crucial for instructing neuronal maturation and circuit patterning (Pacitti et al., 2019). Finally, transgenic animals allow for investigating gene-specific mechanisms of brain development but are laborious to build, limited to genes that do not disrupt systems crucial for embryo survival, and do not recapitulate the complexities of nervous system disorders in higher-order species (Buchsbaum et al., 2019). Therefore, an alternative system is needed to probe the genetic mechanisms of neuronal development across diverse species within a fully intact, whole-brain system.

Blastocyst complementation has recently been adapted to build a system to study forebrain development in mice (Chang et al., 2018). This system showed that selective ablation of cell populations might be useful to produce subtype-selective brain chimeras through blastocyst complementation rather than injury-inducing, late-stage transplantation. Furthermore,

using PSCs generated through either induced pluripotency (iPSC) or derivation from embryos (ESC), which both may be readily genetically altered, enables the systematic dissection of processes underlying neuronal development and circuit formation. An interspecies blastocyst complementation approach challenges naive PSCs to balance unfamiliar exogenous signals with internally driven genetic programs in order to develop with a foreign host blastocyst into functional neural circuits starting from the earliest stages of embryogenesis. This interspecies approach is of consequence to efforts in regenerative medicine because it may provide a means to investigate the development and function of neurons from less accessible species within a whole-brain system. Others have generated interspecies chimeras with contribution throughout the entire organism including the pancreas, thymus, heart, lungs, and liver (Isotani et al., 2010; Isotani et al., 2016; Kobayashi et al., 2010; Wu et al., 2017), but whether species-specific differences such as division rate, cell size, and receptor diversity pose barriers to functional reconstitution of different neural circuits has not been addressed. To this end, we sought to establish interspecies chimeras as a system to study neuronal development and circuit formation.

Results:

Interspecies chimeras show diverse rat neuronal contribution

Rodent interspecies chimeric models generated from blastocyst complementation contribute to tissues throughout the entire organism, including, to an unknown scale, the brain (Isotani et al., 2010; Isotani et al., 2016; Kobayashi et al., 2010; Wu et al., 2017). Rat brains are larger than mouse with more cells per region, neurites that travel longer distances, and potentially different ratios of cells in regions evolved for distinct functions. Here, to enable the quantitative assessment of rat cells in the mouse brain, we initially employed rat ESCs

engineered to express the orange fluorescent protein, Kusabira Orange (KsO) (Wu et al., 2017). We injected 16-20 of these cells into early-stage mouse blastocysts, which were then transplanted into foster mouse mothers to complete their development (Figure 3.1a). In WT mice, we observed varying degrees of contribution, identified by the expression of KsO, throughout most tissues including the brain (Figure 3.1b). Chimeras with brain contribution showed non-symmetric, bilateral contribution to various brain regions including the OBs, piriform cortex (PCx), multiple neocortical areas, hippocampus (Hipp), caudoputamen (CP), and cerebellum (CB) (Figure 3.2a). Within these brain regions with rat contribution, diverse neuronal subtypes formed characteristic morphological dendritic branching patterns and cell layer organizations indicating rat neurons become specified within chimeric brains (Figure 3.2b). Importantly, brain contribution can also be observed with iPSCs, described later.

Six chimeras with high brain contribution were selected for whole-brain imaging and three-dimensional reconstruction to determine where rat neurons either consistently or rarely contribute. Surprisingly, these analyses showed only 31 measured regions did not show contribution in any of the imaged brains (31/838, 3.70%), and the remaining regions showed averaged complementation levels ranging from 0.01% to 87.12% through the stochastic nature of contribution. Cortical areas, hippocampus, and cerebellum showed relatively robust rat cell density whereas olfactory areas, many cortical nuclei, midbrain, and hindbrain regions had less than 5% on average (Figures 3.3a and b). Although the source of KsO signal could originate from cell types in the brain besides neurons including microglia, glia, pericytes, and vascular endothelial cells, these data indicate rat cells are involved in the vast majority of neural circuits.

Rat neurons reprogram their developmental timing to the mouse environment

A main evolutionary distinction between rat and mouse is the timing of their brain development and lifespan, with rat gestation and brain development lagging behind the mouse by up to two days (Semple et al., 2013). Functional reconstitution of diverse species would likely require that cells adapt to the developmental timeline of the host species. However, decades of interspecies transplantation experiments have shown that in most contexts, implanted cells maintain their own species-defined developmental timing despite maturing in an accelerated host environment (Espuny-Camacho et al., 2013; Espuny-Camacho et al., 2018; Falkner et al., 2016; Linaro et al., 2019). Here, we wished to determine whether rat cells developing in tandem with mouse cells from the earliest stages of embryogenesis would be able to interpret extracellular cues or maintain a rigid internal developmental clock. To test this, we birth-dated rat neurons using BrdU and EdU injections (Figure 3.4a).

Cortical regions are built by radial migration from the ventricular zone such that early-born neurons are located in deep layers and late-born neurons migrate further to build superficial layers (Greig et al., 2013; Molyneaux et al., 2007). Cortical neurons also identify and express genes dependent on their layer. Thus, we can imagine three outcomes occurring in chimeras (Figure 3.4b). A transplantation model would predict internal mechanisms dominate, so rat neurons will develop slower and migrate further than mouse neurons born at the same time. Despite being in more superficial layers, the gene expression of rat neurons would be intrinsically determined by their birth-date (model 1). Alternatively, their gene expression may be shaped by their microenvironment so that their layer identity would change to match that of neighboring mouse neurons born at later times (model 2). In the third model, rat neurons interpret extracellular cues and thus adopt the timing and migration of the mouse host

environment, express matching cortical layer genes, and otherwise mimic mouse neurons. We observed temporal reprogramming of rat neurons in multiple cortical regions based on their layering (Figures 3.5a and b). These findings are consistent in non-cortical regions, where the proportion of rat neurons labelled at each time point matches mouse neurons by birth-date (Figures 3.6a and b).

Although cortical neurons layer by birth-date appropriately, their gene expression may not match that of the surrounding mouse neurons. We stained for Ctip2, a protein selectively expressed in early-born, deep cortical layers, and found rat neurons express the appropriate layer-specific marker (Figures 3.7a and b). There is a superficial shift (~30 μm) for rat neurons that may indicate slight rigidity in their intrinsic genetic programs. Together with the birth-dating experiments though, these findings suggest rat neurons largely reprogram their developmental timeline to match their mouse host.

Rat neurons functionally integrate with mouse neurons

The central function of a neuron is to communicate within neural circuits by interpreting incoming information and transmitting output signals to downstream targets. However the neurons of different species might be expected to differ in the surface adhesion proteins necessary to recognize synaptic partners and form appropriate connections. To determine whether rat neurons can functionally communicate with mouse neurons in chimeric brains, we generated new rat iPSCs engineered to express the hChR2(H134R)-eYFP variant of channelrhodopsin (Figure 3.8a) (Zhang et al., 2007). Rat iPSC subclones were screened by eYFP expression, genotyped to verify they belonged to the *Rattus norvegicus* species (Figure 3.8b) and stained for pluripotency proteins (Figure 3.8c). Generating these new labelled lines provides us a

tool to visually identify rat neurons, selectively activate them using blue light in derived chimeras, and record synaptic responses in targeted neurons.

Four integrated rat iPSC lines were injected into WT mouse blastocysts, and one (SD riPSC 9.3) yielded chimeras based on eYFP expression. Acute slices containing the hippocampus and cortex were collected from SD riPSC 9.3 chimeras for electrophysiology recordings (Figure 3.9a). Recordings from hippocampal and cortical pyramidal neurons showed EPSPs in rat neurons 5-15 ms after light-stimulation that were blocked by AMPA and NMDA glutamate receptor antagonists (Figures 3.9b and c). Importantly, the rapid depolarization in a negative control, eYFP-positive rat neuron was unaffected. Furthermore, only the eYFP-positive rat neuron could be driven to fire action potentials by light-stimulation (data not shown). Interestingly, in all ten recorded rat neurons, we did not observe any light-activated IPSPs. Together, these findings indicate rat neurons overcome species-specific barriers to form functional synapses with mouse neurons.

Precise targeting by rat neurons in chimeric brains

In order to reliably transmit downstream signals, neurons must project their axons to the correct location and form specific connections. Rat circuits differ from mouse in that rat neurons are larger and project their neurites longer distances. The stereotyped anatomical structures of the olfactory system offer a unique system for investigating axonal pathfinding and targeting. OSNs in the peripheral olfactory epithelium (OE) continuously turnover during an animal's lifetime but are able to target their axons to precisely located glomeruli in the OB depending on their stochastic choice of one in over 1200 genetically encoded odorant receptors (Young et al., 2002; Zhang et al., 2002). This spatial map must be preserved by each new cohort of OSNs and is

relatively conserved across animals of the same species (Belluscio et al., 2002; Bozza et al., 2002; Gogos et al., 2000). However, the rat olfactory system differs slightly from the mouse in that the rat genome encodes ~100 more odorant receptors than the mouse, creating a different and more complex glomerular map (Zhang et al., 2007).

We sought to use the olfactory system to test whether rat cells specify into OSNs that can navigate axons to form specific glomerular targets in the mouse OB. The OE in early postnatal chimeras revealed mature rat OSNs that express the selective marker, OMP (Figure 3.10a). In some sections, rat sustentacular cells and OSNs formed column-like clusters implicating rat progenitor cells may form along the basement membrane of the OE (Figure 3.10b). Additionally, bundles of axon fibers were visible emanating from these clusters and directed toward the OB. In OB images, we observed rat axonal fibers originating from the ONL innervating and forming round glomerular structures (Figure 3.11a). We were also able to observe rat glomeruli in a two-year-old chimera, indicating these rat glomeruli are stable structures in the mouse brain (Figure 3.11b). Surprisingly, none of the glomerular structures showed innervation by rat MT neuronal dendrites, the synaptic targets for OSNs. Rat cells comprised other neuronal subtypes in the OB (inhibitory GCs and periglomerular neurons), but MT neurons were noticeably absent.

Based on the difference in the odorant receptor repertoire between rats and mice, we might expect unique rat receptors and glomeruli to form in chimeras. In mice engineered to express a rat odorant receptor in place of a mouse receptor, those OSNs will form unique glomeruli rather than mixing with glomeruli of closely related odorant receptors (Belluscio et al., 2002; Bozza et al., 2002). To determine if rat OSNs form unique or mixed glomeruli in our chimeras, we counted glomeruli from serial OB sections of young animals with unilateral OSN complementation (Figure 3.11c). OBs with rat glomeruli had significantly more total glomeruli

than OBs without, indicating a portion of the rat glomeruli were in addition to the normal mouse glomerular map (Figure 3.11d). These results suggest rat OSNs may have access to and express odorant receptors encoded to their genome that are not normally found within the mouse.

Rat complementation in transgenic mouse blastocysts

One main goal of interspecies complementation is to engineer systems in which only specific neuronal subtypes or regions are replaced with another species in order to isolate and dissect mechanisms of neuronal development and circuit formation. A means to accomplish this was recently reported in mouse-mouse brain chimeras where genetically-encoded diphtheria toxin (DTA) was expressed in precursor cells resulting in an ablated forebrain (Chang et al., 2018). Here, we wished to determine whether expressing DTA in maturing OSNs would enable functional reconstitution of the mouse olfactory system. The gene *Omp* is well-established to selectively activate OSNs through Cre-Lox recombination (James, 2013). To test for functional reconstitution of OSNs, we thus generated *Omp*-selective DTA (OMP-DTA) blastocysts for rat-mouse blastocyst complementation (Figure 3.12a).

First, we validated whether the DTA approach successfully ablates mouse OSNs. Counting OMP-positive OSNs in the OE of young OMP-DTA mice showed a near complete absence of mature OSNs by P5 (Figures 3.13a and b). Similarly, in the OB of P5 OMP-DTA mice, OMP staining was minimal in the ONL with no visible glomeruli (Figure 3.14a). Furthermore, the overall size of the OB was decreased partly due to the decreased area in the GL (Figure 3.14b). In aged animals though, a small number of misshapen glomeruli were observed, yet the OB remains significantly smaller in every layer than in WT (Figures 3.14a and b). Olfactory-based suckling and feeding behaviors were also impacted by partial OSN ablation.

OMP-DTA pups had a high mortality rate within the first day following birth (Figure 3.15a), and those animals that survived were significantly smaller than their WT littermates (Figures 3.15b and c). Although OSN ablation is not complete, the OB circuit is severely degenerated in OMP-DTA mice which can be used to test for functional reconstitution.

Viable, transgenic chimeras were successfully generated using rat DAC2 ESCs in OMP-DTA mouse blastocysts and were screened for rat glomerular structures. In rat OSN-complemented, OMP-DTA mice these rat structures were significantly smaller and more disorganized than WT mouse glomeruli (Figure 3.16a and B). The number and ratio of rat glomeruli within the OB was unchanged in OMP-DTA chimeras (Figure 3.17c) compared to WT chimeras indicating contribution was not enhanced in the DTA transgenic background. One explanation for these observations may be that rat OSNs require the structure and cues from mouse OSNs in order to navigate to the OB and form robust glomeruli. Alternatively, the DTA model system is similar to transplantation and injury models where there are increased levels of neuronal death and microglial-immune responses, which may create an environment that is harmful to the survival of rat OSNs.

To overcome these potential blockades, we reasoned that it might be possible to silence neurons rather than kill them. To accomplish this, we employed tetanus toxin (TeNT), which has been used to study the role activity plays in neuronal circuit development (Zhang et al., 2008). Rather than ablating, TeNT silences neurons by blocking synaptic vesicular release while leaving circuits structurally intact. Using this system, we set out to determine whether rat OSN complementation is promoted in chimeras generated with *Omp*-selective TeNT blastocysts (OMP-TeNT), where mouse OSNs are silenced rather than ablated (Figure 3.12a). Rat DAC2 ESCs were injected into OMP-TeNT mouse blastocysts to produce viable, transgenic chimeras,

and four chimeras presented round, well-defined rat glomeruli. In rat OSN-complemented, OMP-TeNT chimeras, we observed the size of rat glomeruli was enhanced such that there was no difference between rat and mouse glomeruli (Figure 3.16a and b). In fact, rat glomeruli in OMP-TeNT chimeras were larger than in WT or OMP-DTA chimeras, but the overall ratio was unchanged (Figure 3.17c). Therefore, we find the TeNT system, where structural mouse circuit integrity is maintained, is preferred to the DTA approach in order to model functional reconstitution in interspecies chimeras.

Finally, we wanted to address whether mouse circuits can interpret information gathered by rat sensory neurons. In the OB, inhibitory periglomerular neurons surrounding glomeruli receive direct input from OSNs and express tyrosine hydroxylase (TH) in an activity-dependent manner (McLean et al., 1988). Using OSN-compromised transgenic chimeras, we observed TH expression was significantly increased in rat glomeruli compared to neighboring mouse glomeruli only for OMP-TeNT chimeras (Figures 3.17a and b). Positive expression in all backgrounds indicated rat glomeruli were functional, but the elevation in the TeNT background suggests rat glomeruli replace mouse glomeruli for olfactory processing in these chimeras.

Olfactory information is transmitted to primary cortical processing regions, including the piriform cortex (PC), through excitatory MT neurons, which are the single output neuronal subtype in the OB (Schneider et al., 1983; Scott 1981). Ablating or silencing OSNs decreases PC network activity (Franks et al., 2005; James, 2013; Kim et al., 2006). Therefore, the PC can be used as a direct readout of OSN activity (Stettler et al., 2009). To determine whether rat OSN information is communicated to cortical processing regions, we assessed immediate early gene expression in the PC of chimeras with unilateral OSN-complementation. Rat OSN complementation significantly increased cFos expression in both OMP-DTA and OMP-TeNT

chimeras, whereas Egr1 expression was only increased in the latter (Figures 3.18a and b). This increase was not reflected in WT chimeras, likely because mouse OSNs remain functionally intact and able to communicate with downstream circuits. These data demonstrate sensory information from rat OSNs in the periphery is interpreted and relayed by mouse neurons throughout the olfactory system and may be more robust in the TeNT system.

The ultimate goal of sensory neurons is to drive behavior in response to relevant environmental stimuli. To test whether rat OSNs shape olfactory perception, aged transgenic chimeras were assayed using the buried cookie test (Figure 3.19a). OMP-DTA and OMP-TeNT transgenic mice were less likely and significantly slower at locating the buried reward than WT mice (Figure 3.19b). WT and OMP-DTA chimeras showed improved response rates and times, but this could not be directly linked to rat OSN complementation. These observations indicate mouse circuits are flexible to interpret signals from foreign neurons and rat neurons are capable of shaping mouse behavior, but in order to better understand these influences, more chimeras would need to be generated and tested.

Discussion:

Here we establish rat cells are capable of generating diverse neuronal subtypes that contribute throughout the vast majority of brain regions within blastocyst-complementation derived, rat-mouse interspecies chimeras. The birthdate and maturation of these rat neurons are largely shaped by the mouse host environment. Furthermore, rat neurons demonstrate precise axonal targeting and synaptic specificity such that they integrate with mouse neurons to shape neuronal circuit activity. These results establish blastocyst-complemented interspecies chimeras

as a model system to study neuronal specification and development and provide insights into the rules governing neuronal circuit formation relevant for regenerative medicine.

Development and diversification of rat neurons

The majority of transplantation and grafting studies rely on introducing fully or partially differentiated cells and tissues into a host organism (Balaban et al., 1988; Constantine-Paton et al., 1975; Espuny-Camacho et al., 2013; Falkner et al., 2016; Mansour et al. 2018). Alternatively, blastocyst complementation uses naive, unbiased PSCs that can differentiate into any, and all tissues of the new organism (Boland et al., 2009; Chen et al., 1993). For xenogeneic complementation, the injected stem cells are challenged to translate signals from and communicate with foreign host cells beginning at the earliest stages of development. Is the host environment able to constrain cells to contribute to only certain tissues and cellular subtypes? Or are they free to specialize into any, and all subtypes encoded by their genome?

Other studies in interspecies chimeras demonstrated complementation to a large diversity of somatic tissues, including the pancreas, thymus, heart, lungs, and liver, as well as to germ cells (Isotani et al., 2010; Isotani et al., 2016; Kobayashi et al., 2010; Wu et al., 2017). Our findings extend these results by characterizing where cells contribute within chimeric brains. Rat neurons were seen populating the vast majority of brain regions and differentiating into specialized neuronal and non-neuronal subtypes. These findings indicate rat neurons are able to interpret extracellular cues in the mouse brain required for successful specification, migration, and integration. It remains unclear however, whether these subtypes constitute the entire repertoire of cellular subtypes found throughout the mouse brain, and how closely rat neurons relate to mouse neurons of the same subtype within the same region.

The developmental timing of cells is in part driven by intrinsic mechanisms. Human neural progenitors grafted into the cortex of immune-deficient mice have been shown to differentiate into neurons across all layers of motor and visual cortex but require a full nine months to mature (Espuny-Camacho et al., 2013; Espuny-Camacho et al., 2018; Falkner et al., 2016; Linaro et al., 2019). Differentiation studies *in vitro* also report intrinsically-determined developmental timelines for iPSC/ESC-derived cell types (Barry et al., 2018; Gaspard et al., 2008; Shen et al., 2006). In contrast, our birth-dating experiments showed rat neurons are shaped by extracellular cues to reprogram their developmental timing of brain organogenesis to that of their mouse host.

Jun et al. (2017) observed rat cells are flexible and could contribute to the gallbladder in interspecies chimeras, an organ not developed in rats but present in mice. Interestingly, the Nakauchi laboratory conducted a series of experiments showing the size of a complemented pancreas is dependent on the host blastocyst (Kobayashi et al., 2010; Yamaguchi et al., 2017). Evidently, the host organism environment dramatically shapes the fate of blastocyst-injected cells. Identifying which, if any, subtypes rat neurons cannot form in mouse brains would aid in understanding the constraints on this flexibility. In our studies, we observed the potential absence of rat contribution to early-born neuronal populations including MT neurons in the OB. These findings indicate there may be some barriers to rat neuronal specification and development and warrants further experimentation.

Alternatively, it is intriguing to speculate whether there are any rat-specific subtypes added in chimeric brains. An interesting region to investigate would be the OE, where the rat genome encodes ~1300 odorant receptors compared to ~1200 in the mouse genome (Zhang et al., 2007). Our analyses identified ~240 rat glomeruli in WT chimeras indicating non-

overlapping odorant receptors with the mouse. Are these rat-specific or a random sampling of all odorant receptors? Future studies, including large-scale single-cell RNA-Seq experiments and in-depth analysis of individual circuits will surely provide insight to these questions.

Formation of functional neuronal circuits

Neurons are unique cells in that they generate long-range, elaborate axonal projections in order to communicate with postsynaptic targets. Grafting and blastocyst complementation experiments using species-matched tissues observed robust, on-target innervation from donor cell populations (Chang et al., 2018; Constantine-Paton et al., 1975). Efforts using grafts or transplants in mixed species systems found similar results, but in cases with human iPSC-derived organoids, there is limited integration (Balaban et al., 1988; Espuny-Camacho et al., 2013; Falkner et al., 2016; Mansour et al. 2018). Using the olfactory system as a model, we found rat OSNs direct their axons to appropriate targets in the mouse brain and form specialized, glomerular structures. Rat OSNs are in part instructed by mouse OSNs as evidenced by the deterioration of glomerular size in OMP-DTA chimeras and their enhancement in OMP-TeNT. Given the recent findings in the forebrain using mouse-mouse complementation with DTA animals, we were surprised rat complementation was impaired in DTA chimeras (Chang et al., 2018). These findings suggest to us that while rat neurons may be disadvantaged to mouse neurons in competitive, WT environments, their development and maturation is hindered in the absence of structural guidance cues provided by related mouse neuronal subtypes. Therefore, future interspecies complementation studies may consider using a TeNT based system in order to create a cellular niche.

Our electrophysiology and immediate early gene experiments indicate rat neurons are able to communicate to mouse neurons and circuits, and thus drive brain-wide activity. Are these signals strong and coherent enough to shape perception? And are mouse neural circuits capable of interpreting this information? Our behavior experiments indicate rat neurons shape mouse behavior, but were unfortunately too underpowered to answer whether specific neuronal subtypes shape perception. The system as it stands needs to be optimized in order to increase the efficiency of derived chimeras with rat OSNs for detailed behavioral analysis. Future experiments using whole OB imaging to characterize the number, identity, and location of rat glomeruli within the mouse OB may shed light on what complementation thresholds exist for functional olfactory reconstitution.

There is precedent though, that transplanted tissues and grafted neurons are able to functionally interpret, as well as shape and direct behavioral output (Balaban et al., 1988; Constantine-Paton et al., 1975; Elliott et al., 2015; Falkner et al. 2016; Linaro et al., 2019). In fact, the quail-chick experiments demonstrated transplanting specific regions of the developing neural tube transfers species-dependent crowing behaviors to chimeric birds (Balaban et al., 1988). We can imagine, given further optimizations, this system could be used to test whether rat-mouse chimeras are endowed with rat-specific behaviors dependent on the complementation of relevant neuronal subtypes.

How could we optimize this system for future studies? The first hurdle is to optimize the efficiency of generating chimeras. One method would be to use PSCs in a primed state that matches the temporal state of the mouse embryo, which has been shown to work with human iPSCs (Wu et al., 2015). Another method would be to shape the fate trajectory of injected cells. Either a temporal overexpression approach, similar to directed-differentiation experiments, to

push cells into specific neuronal lineage, or a knockout approach to restrict them to certain fates may be a viable option to generate chimeras with only neuronal contribution. The rules for complementation are likely to be different for each neural circuit though. Experiments in the Vanderhaeghen laboratory showed neuronal transplantation efficiency and integration varies dramatically across different cortical regions (Espuny-Camacho et al., 2019). If we could learn the rules of how to direct or select for certain neuronal subtypes, this approach would provide an efficient means to study the development and function of difficult to access neuronal subtypes, including human neurons, within an intact nervous system.

Acknowledgements:

Chapter 3, in part, is currently being prepared for submission for publication of the material. Throesch, B.T., Wu, J., Castaneda, R.M., Hartzell, A., Sakurai, M., Rodriguez, A.R., Martin, G., Lippi, G., Osten, P., Kupriyanov, S., Belmonte, J.C.I., and Baldwin, K.K. The dissertation author was the primary investigator and author of this paper.

Materials and methods:

Mouse strains

CD1 animals were used for surrogate mothers, birth-dating experiments, and to generate MEF feeders. *Omp*-IRES-Cre (Eggan et al., 2004) mice were generated by Kristin Baldwin in the Axel laboratory. The TeNT-GFP mouse strain was described in chapter 2. ROSA-DTA (DTA) mice were originally generated by Richard M. Locksley (Voehringer et al., 2008) and ordered from The Jackson Laboratory (Stock # 009669). All lines were bred as homozygous or

crossed with C57BL/6J mice from The Scripps Research Institute breeding colony to generate heterozygotes.

All animal experiments were conducted in accordance with the protocols approved by the IACUC of The Scripps Research Institute and NIH guidelines for animal use.

Genomic PCR:

Genomic DNA was extracted from tail tip samples using the REDExtract-N-Amp Tissue PCR kit (Sigma-Aldrich XNAT-100RXN). PCRs were performed using the REDExtract-N-Amp PCR Readymix (Sigma-Aldrich R4775).

The following primers were used for genotyping:

Omp WT Forward: 5' – TGT ATT TCC TCA TCA CCT TTG GCG – 3'

Omp WT Reverse: 5' – GGT CAG TCT CTT ATC TCT CAG TCC CG– 3'

For species genotyping, Genomic DNA was extracted from cell pellets using the DNeasy Blood and Tissue kit (Qiagen 69504). PCRs were performed using the Platinum PCR SuperMix High-Fidelity kit.

The following primers were used:

Omp Mouse Forward: 5' – CCT GAC AGG GGC TAT GAC AGA GTG – 3'

Omp Rat Forward: 5' – GGC AGT ATG CGG TTG GAT CAA TCA G – 3'

Omp Common Reverse: 5' – CCT GGT CCA GAA CCA GCG GC – 3'

Blastocyst complementation and embryo transfer:

DAC2 and DAC8 cells lines were generated previously and provided by the Ying laboratory (Li et al., 2008). Rat iPSC lines were generated as described in the "Rat iPSC reprogramming and culturing" section. To prepare for blastocyst injection, rat PSCs were cultured in 10-cm^2 MEF-coated plates until approximately 70-80% confluent (culturing conditions and media described in "Rat iPSC reprogramming and culturing"). The cells were washed twice with dPBS (Gibco 14910), then trypsinized for 4 minutes in TrypLE Express (Gibco 12604013) at 37°C. After incubation, 10 ml of iPSC media was added to the plate and a single cell suspension was made via manual pipetting. The 10-cm^2 plate was placed back in the 37°C incubator for 30 min and then the cell suspension was gently transferred to a new plate to separate MEFs from rat cells. This process was repeated again to further isolate rat cells, and then the rat cell suspension was transferred to a 15 ml conical tube and spun at 1000 rpm for 30 sec. The solution was removed to leave the cell pellet undisturbed and spun for an additional 2 min at 1000 rpm. The remaining supernatant was removed, and then the cell pellet was resuspended in 150 ul of FHM medium (CytoSpring F1103) to create a single cell solution. The cells were stored on ice for injection.

Female mice were super-ovulated by intraperitoneal injections of 5 U of pregnant mare serum gonadotropin (PMSG, ProSpec-Tany TechnoGene HOR-272), followed by 5 U of human chorionic gonadotropin (hCG, Sigma-Aldrich C1063) 47 hr later, and were then mated with stud males. Morulae were collected from the oviducts at 2.5 days post coitum and cultured overnight in KSOMaa medium (CytoSpring KO113) to the blastocyst stage. Single-cell suspensions of rat PSCs were added to a drop of FHM medium on the injection slide, containing the blastocysts to be injected. Individual cells were collected into a 20 μm ID injection micropipette and 16-20

cells were introduced into the blastocoel. After microinjection, the blastocysts were cultured in KSOMaa medium for at least 1 hr until embryo transfer. Injected blastocysts were surgically transferred to the uterine horns of pseudopregnant CD1 recipient mice at E2.5.

Whole-brain imaging:

Animals were transcardially perfused as described below ("Tissue preparation, IHC, and ICC). After post-fixing brains overnight in 4% PFA, samples went through brain clearing, imaging, and registration methods as previously described (Kim et al., 2017).

Tissue preparation, IHC, and ICC:

Mice P21 and older were transcardially perfused as described in chapter 2. Brains with OBs attached and the OE were dissected from the skull and placed in 4% PFA solution overnight at 4°C. For mice P10 and younger, animals were briefly anesthetized, decapitated, and the entire head fixed in 4% PFA solution overnight at 4°C. The following day, brains were washed and stored in dPBS at 4°C.

Vibratome sections were prepared as described in chapter 2. For cryostat sections, samples were submerged in 30% sucrose (Acros Organics 41976-0010) in dPBS at 4°C and left overnight or until the tissue sank to the bottom of the tube. OE samples from mice P21 and older were incubated in 0.5 M EDTA solution, pH 8.0 (Invitrogen 15575020) for 1 hr at room temperature to decalcify before dehydrating in 30% sucrose. Dehydrated samples were then embedded in Tissue-Tek O.C.T. (Sakura 4583), rapidly frozen in a bath of 70% ethanol and dry ice, and stored at -80 °C. Before sectioning, O.C.T. blocks were moved to -20°C for 1 hr. Using a Leica CM3050 S, 30 μm sections were collected onto Fisherbrand Superfrost Plus slides

(Fisher Scientific 12-550-15) and allowed to air dry for 1 hr. Slides were either immediately stained or stored at -80°C for later use.

IHC of free-floating vibratome sections followed the same protocol as in chapter 2. To stain cryosections on slides, the same solutions and timings were used with a few additions. Slices were removed from -80°C and brought to room temperature for ~30 min. In cases of antigen retrieval (AR), slides were submerged in sodium citrate buffer (Sigma Aldrich C9999) warmed to ~85-90°C on a hot plate for 20 min, then subsequently washed twice in fresh dPBS for 5 min per wash. Without antigen retrieval, slides were washed twice in fresh dPBS to rehydrate samples and remove residual O.C.T. Cryosections were left to air dry briefly (~10 min) in order to draw a hydrophobic barrier using an ImmEdge Pen (Vector Laboratories H-4000) before continuing with the staining protocol.

Cells in culture were rinsed once with dPBS and then briefly fixed using 4% PFA in dPBS for 10 min at room temperature. After a wash with dPBS, cells were ready for ICC or stored in dPBS at 4°C. For ICC, the same process was followed as for vibratome sections except samples were not agitated and primary antibodies were used 1:250.

Primary antibodies used:

KsO (rabbit, MBL PM051M) - IHC

NeuN (mouse, Millipore MAB377) - IHC

BrdU (mouse, BD Pharmigen 555627) - IHC (HCl treatment)

Ctip2 (rat, Abcam ab18465) - IHC (AR)

Oct4 (mouse, SCBT sc-5279) - ICC

Sox2 (mouse, SCBT sc-365823) - ICC

SSEA1 (mouse, SCBT sc-21702) - ICC

Nanog (goat, R&D Systems AF2729) - ICC

OMP (goat, Wako 544-10001) - IHC (AR)

VGluT2 (guinea pig, Millipore Sigma AB2251-1) - IHC

cFos (rabbit, CST 2250S) - IHC

Secondary antibodies used:

mouse, Alexa Fluor 647 (donkey, Invitrogen A31571)

goat, Alexa Fluor 555 (donkey, Invitrogen A32816)

Confocal imaging, image processing, and analysis:

All images were acquired on a Nikon A1 confocal microscope as large-image z-stacks. Analysis was performed using Nikon NIS-Elements. To calculate the location of Ctip2, an arc was drawn to mark the border between cortex and corpus callosum. Neurons were manually identified, sorted by KsO double staining, and their shortest distance to the marked border measured. The area and location of each OB layer was calculated the same as detailed in chapter 2. Glomeruli in P10 animals were manually counted across 32 serial sections by identifying circular spaces in the GL devoid of DAPI staining. For glomerular area in older animals, borders were drawn for each glomerulus using DAPI as a guide and sorted by KsO expression. The OE was defined using DAPI as the region between the lumen and lamina propria and layer 2 of PCx as the dense band of nuclei. Cell counts (OMP, Egr1, cFos) were done manually in respective neuronal layers. For TH intensity, glomeruli were outlined and the integrated density calculated using Fiji (Schindelin et al., 2012).

Dual-pulse birth-dating, staining, and analysis:

Pregnant surrogates were given intraperitoneal injections delivering 50 mg/kg of BrdU (Life Technologies B23151) at E12.5 and 50 mg/kg of EdU (Life Technologies A10044) at either E13.5 or E14.5 to label neurons in developing CD1 chimera embryos. Reconstituted as 10 mg/ml (BrdU) and 5 mg/ml (EdU) in dPBS, this equated to 200 µl and 400 µl injections, respectively, for a 40 g mouse. Chimeras were delivered naturally and once they reached 4 wks old, brains were harvested for IHC as described above.

For BrdU-EdU double staining, these modifications were made following the initial IHC blocking step. Free-floating slices were pre-stained by adding the KsO antibody diluted 1:500 in blocking buffer overnight at 4°C. Slices were washed three times with dPBS-T for 5 min each then fixed again with 4% PFA solution for 15 min at room temperature. After washing once with dPBS-T, a preheated 1N HCl solution was added to sections to incubate for 30 min at 37°C. To neutralize, 0.1 M sodium borate buffer pH 8.5 was added at room temperature for 10 min. Slices were washed twice with dPBS-T for 10 min each, blocked with blocking buffer for 1 hr, and stained overnight at 4°C with BrdU and KsO primary antibodies diluted 1:500 in blocking buffer. The subsequent day, slices underwent secondary antibody staining as described previously and were then mounted onto slides and allowed to air dry for 15 min at room temperature. To identify EdU-labeled cells, the Click-iT EdU Cell Proliferation Kit for Imaging (Invitrogen C10340) was used, and the manufacturer's instructions were followed starting with step 4.1 except dPBS-T was substituted for 3% BSA in PBS, slides were incubated with the reaction cocktail for 1 hr, and slides were stained for DAPI in dPBS-T for 1 hr. For NeuN-EdU double staining, slices were first stained for KsO and NeuN following described methods. After

secondary staining, slices were mounted onto slides and the EdU reaction protocol was followed as described above.

NeuN-EdU analysis in cortical regions followed the same methods as for Ctip2 expression. For BrdU-EdU double staining, EdU+ and BrdU+/EdU- labelled cells were manually identified and sorted by KsO expression. Cell densities were normalized to an average density of DAPI+ (mouse) cells or the density of KsO+ (rat) cells present in corresponding regions. Average DAPI+ densities were generated by counting the area ~250 DAPI+ occupy across 8 samples.

Lentiviral constructs and production:

The Syn-hChR2(H134R)-eYFP lentiviral plasmid (Addgene #20945) was generated in the laboratory of K. Deisseroth (Zhang, F., et al., 2007). The rtTAM2.2 cassette (rtTA) was generated in the laboratory of S. Ho (Go et al., 2002) and cloned into a lentiviral transfer plasmid by the K. Baldwin laboratory (Boland et al., 2009). Doxycycline (dox)-inducible lentiviral reprogramming factors encoding mouse cDNAs for Oct4, Sox2, c-Myc, and Klf4 were generated previously in the laboratory of K. Baldwin (Boland et al., 2009). The generation and harvest of lentivirus was described in chapter 2. Lentivirus was directly used after harvest and not ultracentrifuged.

Mouse embryonic fibroblast generation:

Wild-type CD1 matings were setup and checked for plugs. A positive plug was considered day E0.5. Embryos were harvested on day E13.5 and dissected to remove the head, limbs, internal organs, and spinal column. The remaining tissue was sliced into small pieces and

dissociated into single-cells by incubating with 0.25% trypsin-EDTA (Gibco 25200056) for 20 min at 37°C. To stop the digestion, HEK/MEF media was added to the suspension and centrifuged at 200 *g* for 5 min. Pelleted cells were resuspended in HEK/MEF media and seeded on 0.1% gelatin-coated (EMD Millipore ES-006-B) tissue culture flasks. Fibroblasts were grown to confluence and passaged four times with 0.25% trypsin-EDTA before inactivating. To inactivate MEFs, 1 μg/ml mitomycin-c (STEMCELL Technologies 73272) in HEK/MEF media was added to confluent cells and incubated overnight. MEFs were washed three times with dPBS, passaged with trypsin, and either seeded at a density of $1x10^5$ cells/cm^2 on 0.1% gelatin-coated flasks as feeders or stored at -80°C in freezing media (HEK/MEF media + 20% DMSO (Fisher Scientific BP231-100)).

Rat iPSC reprogramming and culturing:

Rat embryonic fibroblasts (REFs) from WT Sprague-Dawley rats were obtained from ATCC (CRL-1213) and cultured the same as MEFs. To reprogram REFs into iPSCs, the Wu et al. (2017) protocol was followed with minor modifications. Briefly, $2.5x10^5$ REFs were plated into a well of a 0.1% gelatin-coated 6-well tissue culture dish. Freshly harvested lentivirus carrying dox-inducible reprogramming factors (Oct4, Sox2, c-Myc, and Klf4) and rtTA were added to the REFs 24 hr later and left to incubate overnight (day 0). Virus was replaced with fresh HEK/MEF media the next morning (day 1) and 5 μg/ml dox (Sigma-Aldrich D9891) in DMSO was added to infected REFs the subsequent day (day 2). On day 4 of reprogramming, REFs were passaged and $5x10^5$ cells were plated onto inactivated-MEFs in 10-cm^2 tissue culture dishes with fresh media including dox. Half the media was removed on day 5 and replaced with iPSC media including dox (N2B27 basal medium (1:1 DMEM/F12 (Gibco 11330032), N2

supplement (Gibco 17502048): Neurobasal A (Gibco 10888022), B27 supplement minus vitamin A (Gibco 12587010)), 100 μM β-mercaptoethanol (Gibco 21985023), 10 ng/mL mouse LIF (STEMCELL Technologies 78056), 3 μM CHIR99021 (STEMCELL Technologies 72052), 1 μM PD0325901 (STEMCELL Technologies 72182)). Reprogramming cells were fed every other day with iPSC media containing dox until day 7, when they were fed every day. By days 9-10, small colonies began to form and around day 13, they were ready to manually pick. Using a P100 plastic pipette tip, colonies were detached from the 10-cm^2 dish and mechanically broken into small pieces before transferring to individual wells of a 24-well tissue culture dish with MEF feeders. Cells were weaned off of dox once they were established in new wells, and validated by staining for pluripotency markers (Sox2, Oct4, SSEA1, Nanog) and species-specific genotyping.

To maintain colonies, cells were fed every day and passaged as single cells every 2-3 days. To passage, iPSC media was removed and replaced with the minimal amount of TrypLE Express to cover the cells. After incubating at room temperature for 5 min, fresh iPSC media was sprayed into the well to detach cells. TrypLE was diluted with iPSC media 1:10 and the cell suspension centrifuged at 200 *g* for 5 min. The cell pellet was resuspended as single cells in fresh iPSC media and sparsely seeded on MEF feeders.

Lentiviral-integrated iPSC subclones:

To generate iPSC lines expressing hChR2(H134R)-eYFP, iPSCs were first separated from inactivated-MEFs by culturing on Matrigel-coated (Corning 354277) tissue culture flasks for 3 passages. HEK/MEF media containing live lentivirus carrying the Syn-hChR2(H134R)-eYFP cassette was added on top of the cells 24 hr after the third passage and left overnight. The

following day, lentivirus was removed, iPSCs were washed twice with dPBS, passaged, and then seeded at $5x10^5$ cells on inactivated-MEFs in 10-cm^2 tissue culture dishes. Three days after seeding, subclones were manually picked using fluorescence as a guide into 48-well tissue culture dishes. To validate successful integration of ChR2(H134R)-eYFP, cells were collected after two passages, DNA extracted using the DNeasy Blood and Tissue kit (Qiagen 69504), and a diagnostic PCR run using the following three primer sets specific for ChR2:

ChR2 Forward 1: 5' – GGA TTG AAT CTC GCG GCA CG – 3'

ChR2 Reverse 1: 5' – GTT GCC ATG GCG CTG GTA GC – 3'

ChR2 Forward 2: 5' – GCG TCC TGA GCG TCT ATG GC – 3'

ChR2 Reverse 2: 5' – GCT TGC CGG TGG TGC AGA TG – 3'

ChR2 Forward 3: 5' – GTT CAT CTG CAC CAC CGG CA – 3'

ChR2 Reverse 3: 5' – GCA CGC TGC CGT CCT CGA TG – 3'

Acute slice electrophysiology, recording, and analysis:

WT chimeras were generated using hChR2(H134R)-eYFP integrated iPSC subclone #9.3 and used from 2-6 wks of age for experiments. To isolate slices containing the Hipp and cortex, animals were anesthetized briefly with isoflurane (Henry Schein 1311758) then decapitated. The skin and skull were removed to expose the brain, which was rapidly dissected out and placed in ice-cold sucrose cutting solution (100 mM Sucrose (Sigma-Aldrich S0389), 60 mM NaCl (Sigma-Aldrich 793566), 26 mM $NaHCO_3$ (Sigma-Aldrich S6297), 20 mM D-Glucose (Sigma-Aldrich G6152), 1.25 mM NaH_2PO_4-H_2O (Sigma-Aldrich S9638), 2.5 mM KCl (Honeywell Research Chemicals 60121), 5 mM $MgCl_2$-$6H_2O$ (Honeywell Research Chemicals 63020), 1 mM $CaCl_2$ (Honeywell Research Chemicals 21114)) bubbled with 95% O_2/5% CO_2. Blocking

cuts were made to remove the CB and OBs, bisect the hemispheres, and orient the Hipp in the transverse plane. The blocked tissue was transferred to the slicing chamber of a Leica VT1200S vibratome containing cold, oxygenated sucrose cutting solution. Isolated 300 μm thick slices were transferred to a recovery chamber containing ACSF (127 mM NaCl, 25 mM $NaHCO_3$, 25 mM D-Glucose, 1.25 mM NaH_2PO_4-H_2O, 2.5 mM KCl, 2 mM $CaCl_2$, 1 mM $MgCl_2$-$6H_2O$) bubbled with 95% O_2/5% CO_2. Slices recovered for 30 min at 32°C and then were maintained at room temperature.

Slices were transferred to a recording chamber and perfused with oxygenated ACSF warmed to 31°C. Whole-cell current clamp recordings were obtained from eYFP-negative mouse or eYFP-positive rat neurons visualized using a Scientifica SliceScope fitted with a SciCamPro for infrared differential interference contrast (IR-DIC) and fluorescence optics. Patch pipettes (3-5 mΩ) were filled with potassium gluconate internal solution (130 mM K-gluconate (Sigma-Aldrich G4500), 11.5 mM Na_2-phosphocreatine (Sigma-Aldrich P7936), 10 mM HEPES (Sigma-Aldrich H3375), 3 mM $MgCl_2$, 3 mM Na_2-ATP (Sigma-Aldrich A2383), 0.2 mM Na-GTP (Sigma-Aldrich 51120), 0.2 mM EGTA (Sigma-Aldrich E4378), pH = 7.2, osmolarity = 307 mOsm). Current was applied to maintain cells at -70 mV and series resistance was monitored throughout recordings. Experiments were discarded if the holding current was greater than -300 pA, if the series resistance was greater than 25 MΩ, or if the series resistance changed by more than 20%. All recordings were acquired using a Multiclamp 700B amplifier and ScanImage software (Pologruto et al., 2003). Signals were sampled at 10 kHz and filtered at 6 kHz. Analysis was performed using IGOR Pro (WaveMetrics).

Light-evoked EPSPs were triggered by illumination with a blue LED in 2 ms epochs every 3 sec. LED intensity was set to the minimum necessary to evoke the maximum amplitude

EPSP. The average baseline EPSP was established with a minimum of 20 sweeps before adding glutamate receptor antagonists (10 μM NBQX (Tocris 0373) and 10 μM CPP (Tocris 0173)) to the bath to block synaptic currents. Responses were monitored as antagonists washed in, and once the EPSP was blocked (~3 min), a minimum of 20 sweeps were recorded. EPSP amplitudes were calculated by averaging the amplitude 0.5 ms before to 2 ms after the peak of the current.

Mouse behavior:

For the survival assay, *Omp*-IRES-Cre and DTA breeding pairs were setup and monitored for litters. At P0, pups were counted and tailed for genotyping. For the subsequent 4 days, litters were checked every morning and evening to count surviving pups and collect any carcasses for genotyping.

Chimeras and littermates P35 and older were used for the buried cookie assay. To pre-expose animals to the reward, an Oreo Mini (Nabisco) chocolate cookie wafer with the icing removed was placed in the home cage 4 or 5 days before testing. Only animals that ate the cookie within 24 hrs were used for further testing. The day before testing, animals were moved to a clean cage and food deprived overnight to increase motivation. For testing, clean static cages without a water port were filled with ~4 cm of fresh bedding and fitted with a clean filter top. Animals were habituated to a clean test cage for 10 min then returned to their home cage. Half an Oreo Mini with the filling removed was buried ~2 cm in a random corner of the test cage and then covered in bedding. Timing began once an animal was placed in the middle of the test cage and the lid replaced. Up to three animals were run at the same time. Each trial ran for a maximum of 15 min or until the animal located and actively interacted with the reward by either carrying it away or eating it. Animals that did not find the reward were shown the cookie and

assessed for motivation. If the animal did not interact with the unburied reward, they were excluded from analysis. Once the trial concluded, the animal was returned to their home cage for 5 min. The test cage was prepared for another trial by removing the reward, mixing the bedding throughout the cage, and then hiding the reward in a different corner. Each animal underwent 3 trials in the same test cage and then were returned to their home cage and provided food.

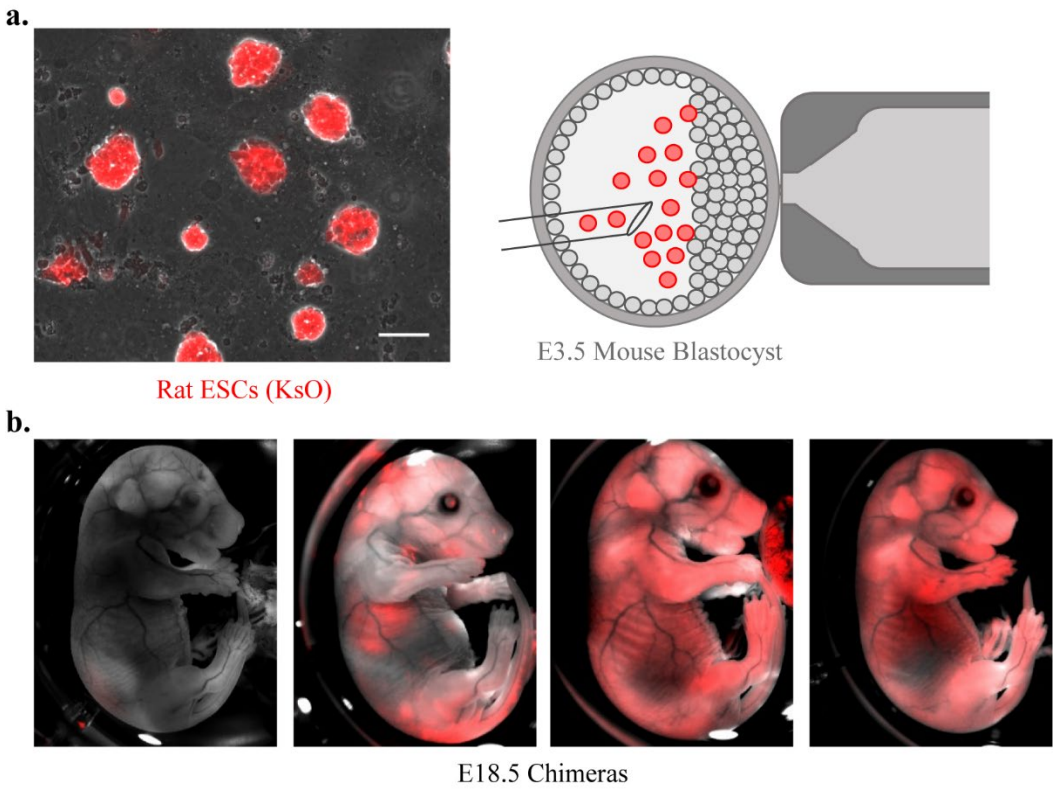

Figure 3.1: Rat-mouse interspecies chimeras are generated using blastocyst complementation.

(a) Schematic of blastocyst complementation. Rat ESCs labelled with KsO (left) are injected into early-stage mouse blastocysts (right) to generate rat-mouse interspecies chimeras. Scale bar is 100 μm.

(b) Rat ESC contribution is visible by KsO in E18.5 chimeras and shows stochastic contribution to mouse tissues.

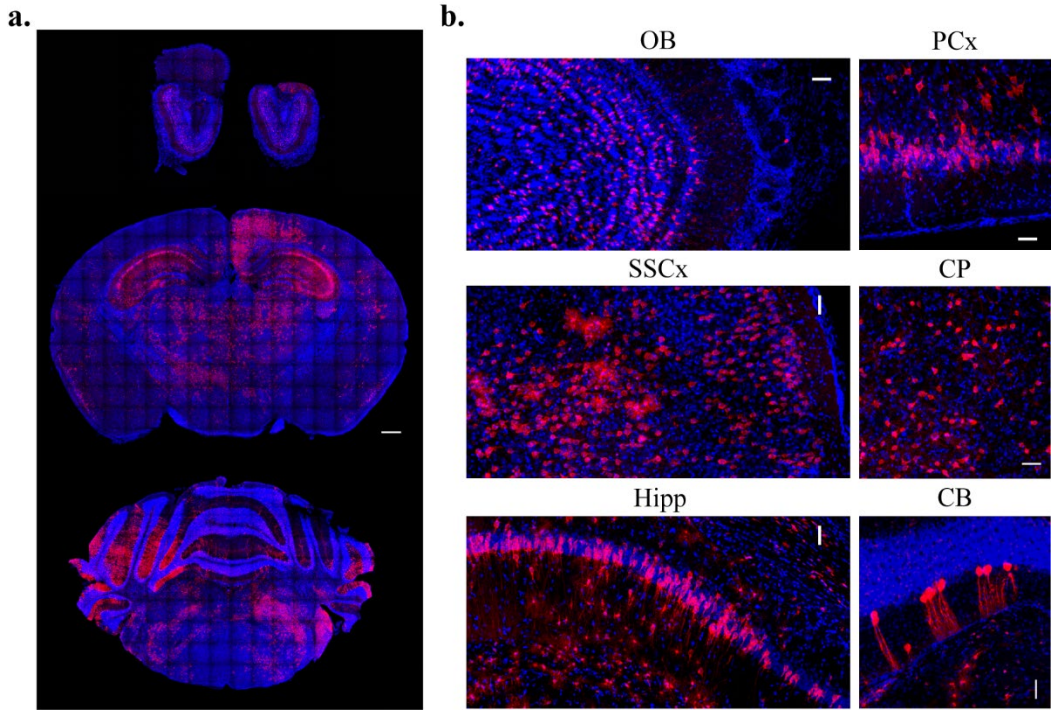

Figure 3.2: Rat cells contribute to diverse neural circuits and neuronal subtypes.
(a) Representative images from coronal brain slices of a 4-6 wk old chimera demonstrate broad, non-symmetric contribution of rat cells to diverse neural circuits. Scale bar is 500 μm.
(b) Zoomed in images reveal diverse cellular subtypes with characteristic neurite branching patterns and layer organization including GCs in the OB, purkinje neurons in the CB, medium spiny neurons in the CP, and pyramidal neurons in the PCx, SSCx, and Hipp. Scale bar is 50 μm.

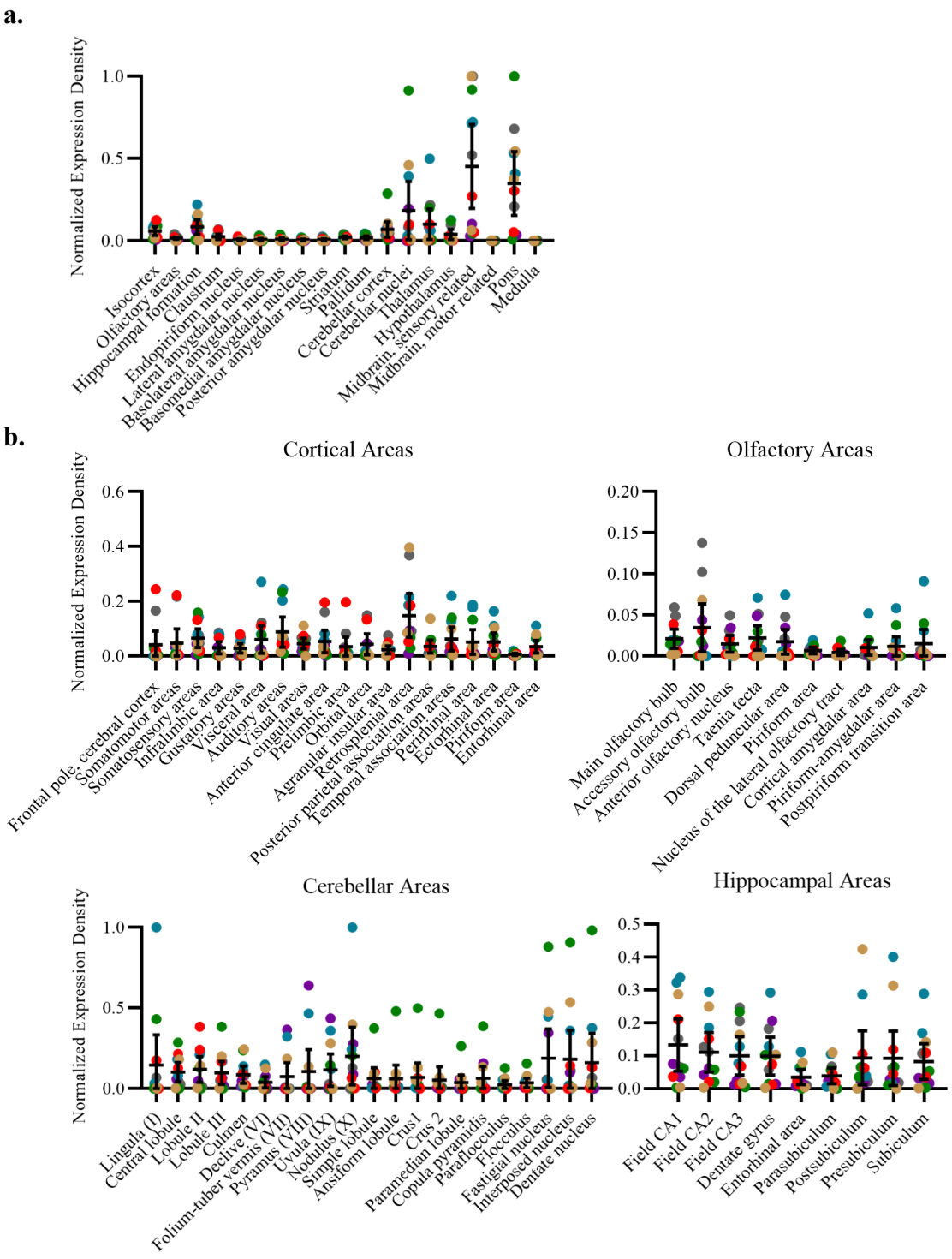

Figure 3.3: Whole-brain imaging reveals widespread rat contribution.
(a and b) Quantification of red pixels registered to a mouse brain atlas reveal rat cells contribute to most neural circuits. 6 animals. Each hemisphere is plotted individually, colored dots denote matching hemispheres. Bar and error represents mean with SD.

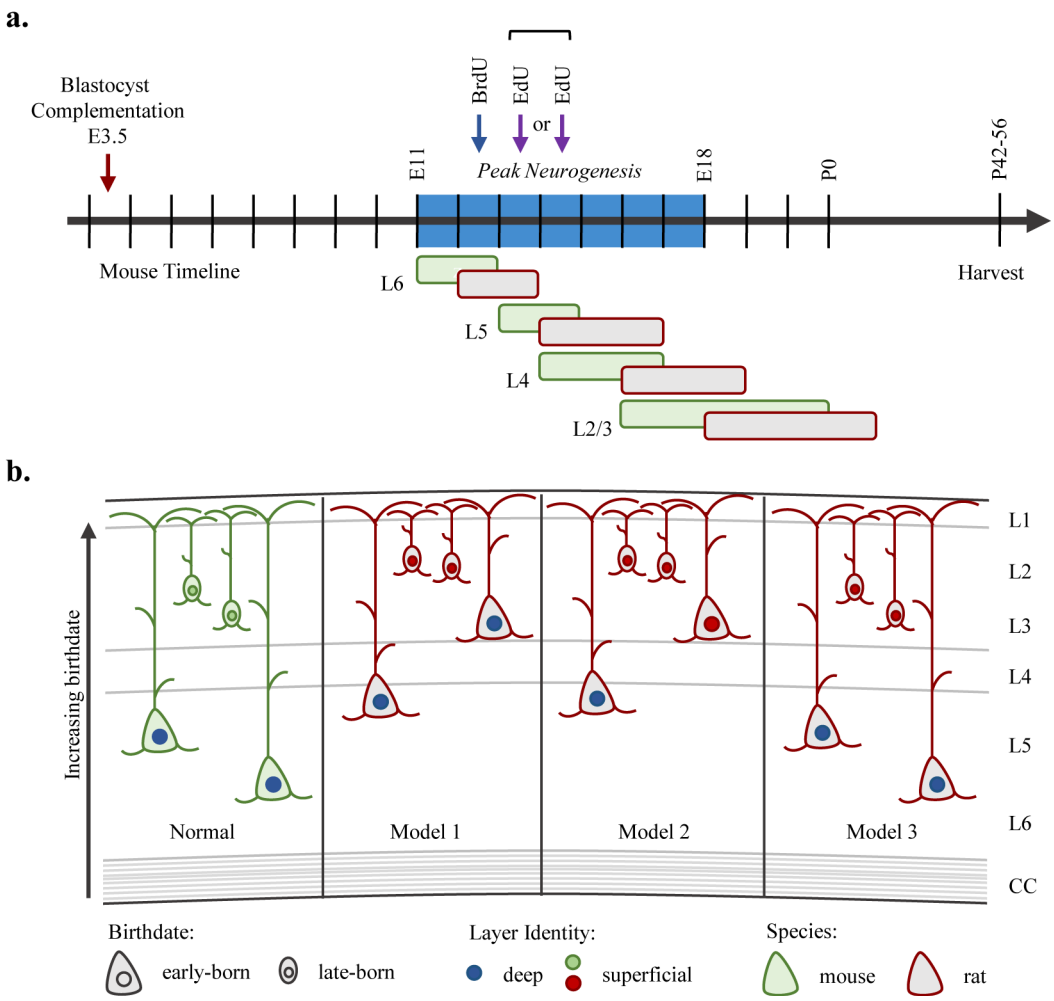

Figure 3.4: Birth-dating schematic and cortical layering model.
(a) Diagram of mouse developmental timeline depicting the peak of neurogenesis occurring between E11 and E18 in mice. Pregnant mouse mothers were injected with BrdU at E12.5 and EdU at either E13.5 or E14.5 to label different populations of neurons. Amongst other regions, corticogenesis in rats lags by one or two days behind the mouse, such that different populations of rat and mouse neurons may be labelled by BrdU/EdU injections.
(b) Model of corticogenesis illustrates potential models of rat cortical layering and maturation. Rat neurons were hypothesized to either maintain their intrinsic developmental timeline (Models 1 or 2) thus showing aberrant layering and identity, or to reprogram their timeline to match the mouse (Model 3).

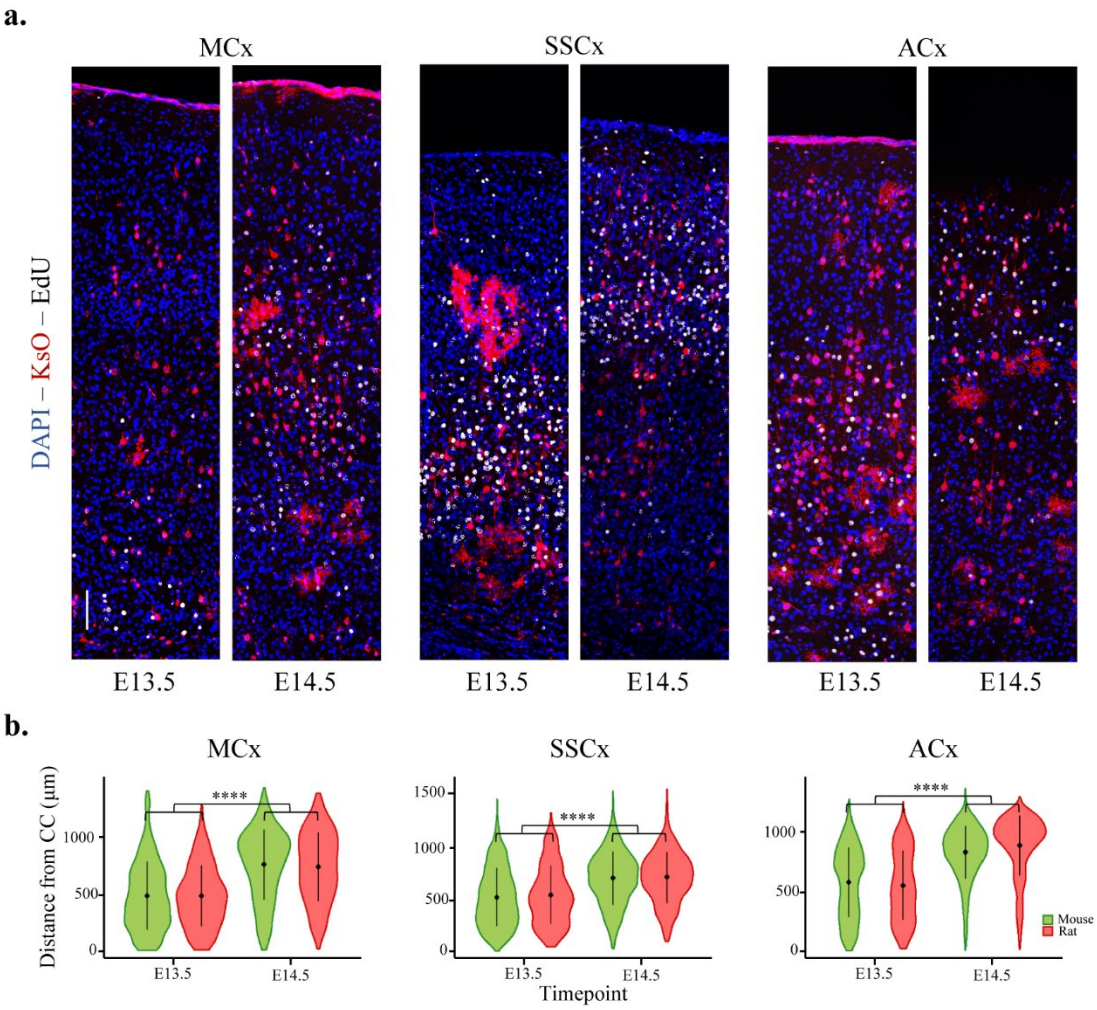

Figure 3.5: Cortical rat neurons reprogram their birthdate to match their mouse host.
(a) Representative images of EdU staining in different cortical regions of 4-6 wk old chimeric brains. Scale bar is 100 µm.
(b) Quantifications reveal rat neurons match the mouse neuronal timing for cortical layering. 3-4 animals/time point, 3 slices/animal. Bar and error represent mean with 2xSD. MCx: E13.5 mouse (3 animals, 2138 cells): 479.32 ± 298.17; rat (498 cells): 478.29 ± 267.79; E14.5 mouse (4 animals, 2961 cells): 751.25 ± 307.05; rat (387 cells): 733.43 ± 301.52. E13.5 mouse/rat vs E14.5 mouse/rat $p < 0.0001$. SSCx: E13.5 mouse (3 animals, 3600 cells): 518.30 ± 270.95; rat (644 cells): 539.74 ± 273.15; E14.5 mouse (4 animals, 5220 cells): 695.96 ± 249.25; rat (1072 cells): 702.90 ± 237.74. E13.5 mouse/rat vs E14.5 mouse/rat $p < 0.0001$. ACx: E13.5 mouse (3 animals, 2879 cells): 578.48 ± 293.05; rat (673 cells): 550.53 ± 290.26; E14.5 mouse (4 animals, 3568 cells): 827.51 ± 220.03; rat (506 cells): 887.18 ± 251.18. E13.5 mouse/rat vs E14.5 mouse/rat $p < 0.0001$. Two-way ANOVA followed by Tukey's multiple comparisons test. ****$p < 0.0001$.

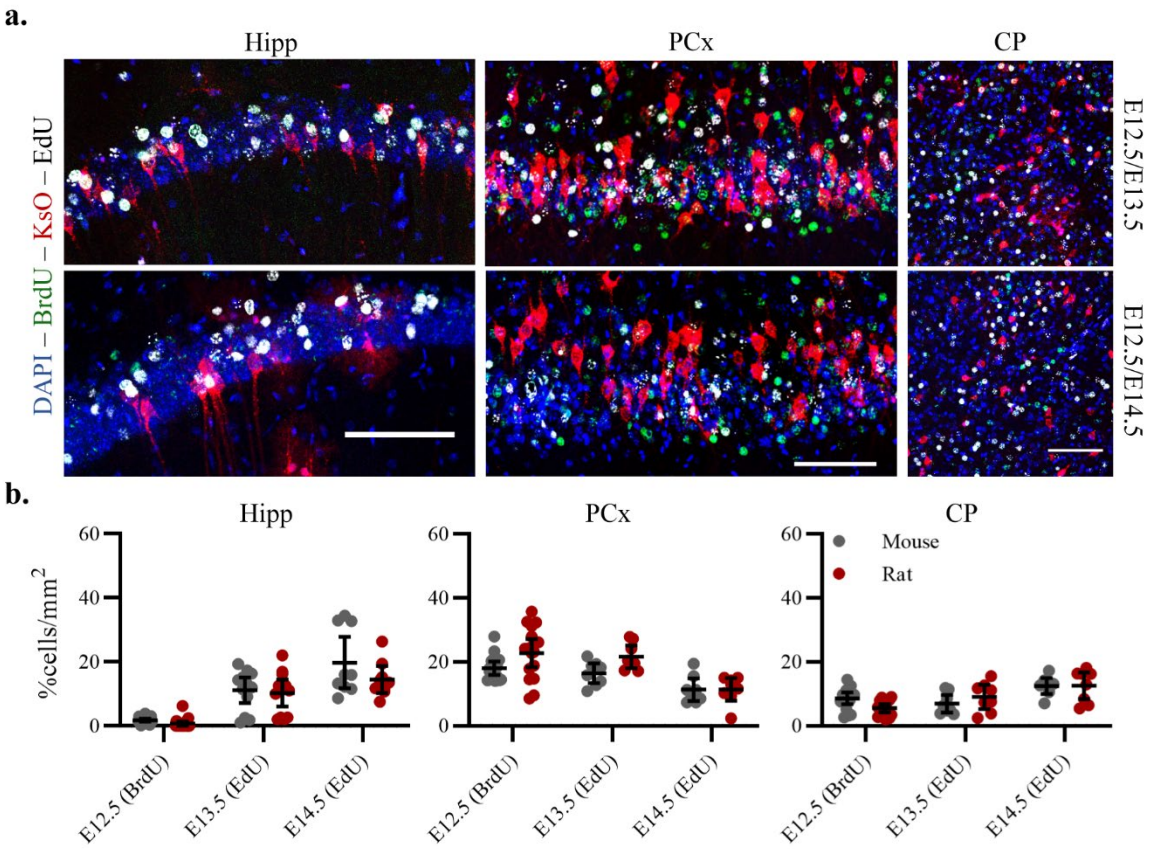

Figure 3.6: Rat neurons reprogram their birthdate brain-wide.
(a) Representative images of BrdU/EdU double staining in different brain regions of 4-6 wk old chimeric brains. Scale bar is 100 µm.
(b) Quantifications reveal rat neurons match the mouse neuronal timing for populating various brain regions. 2-7 animals/time point. Hipp 3 slices/animal, PCx and CP 4 slices/animal. Bar and error represent mean with 95% CI. Hipp: E12.5 mouse (7 animals): 1.80, 1.37-2.22; rat: 0.74, 0.09-1.40; E13.5 mouse (4 animals): 11.15, 7.18-15.12; rat: 10.25, 6.04-14.46; E14.5 mouse (3 animals): 19.76, 11.72-27.80; rat: 14.49, 10.25-18.74. PCx: E12.5 mouse (4 animals): 18.05, 15.99-20.12; rat: 22.77, 18.38-27.16; E13.5 mouse (2 animals): 16.44, 13.31-19.56; rat: 21.64, 18.08-25.19; E14.5 mouse (2 animals): 11.33, 7.79-14.87; rat: 11.39, 7.87-14.92. CP: E12.5 mouse (4 animals): 8.59, 6.78-10.41; rat: 5.52, 4.26-6.78; E13.5 mouse (2 animals): 6.91, 4.16-9.65; rat: 9.04, 5.26-12.82; E14.5 mouse (2 animals): 12.43, 9.93-14.93; rat: 12.53, 8.32-16.74. Mixed-effects analysis followed by Sidak's multiple comparisons test.

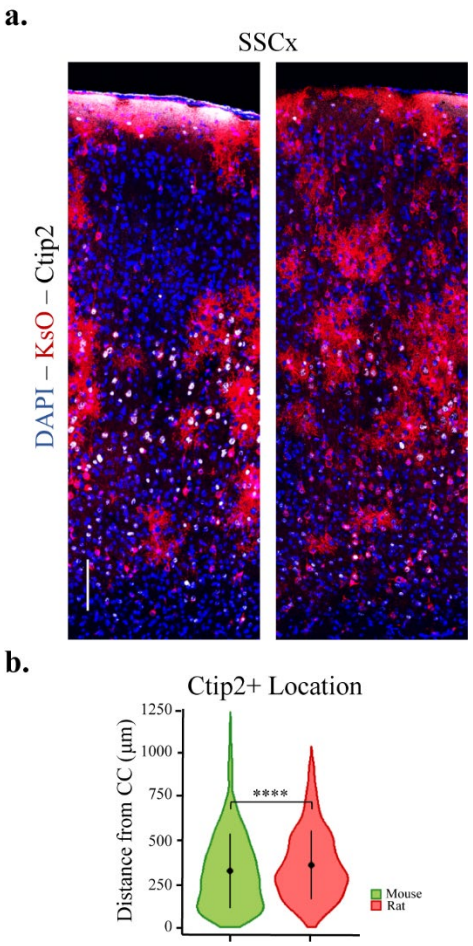

Figure 3.7: Rat neurons selectively express appropriate cortical layer genes.
(a) Representative images of Ctip2 staining in SSCx of 4-6 wk old chimeric brains. Scale bar is 100 µm.
(b) Quantification of the distance of Ctip2+ neurons from the CC of each species demonstrates rat neurons appropriately express cortical layer markers. 6 animals, 3 slices/animal. Dot and error represent mean with 2x SD. Mouse (3827 cells): 323.29 ± 211.20; Rat (971 cells): 357.46 ± 194.86. $p < 0.0001$. Unpaired, two-sided t-test. ****$p < 0.0001$.

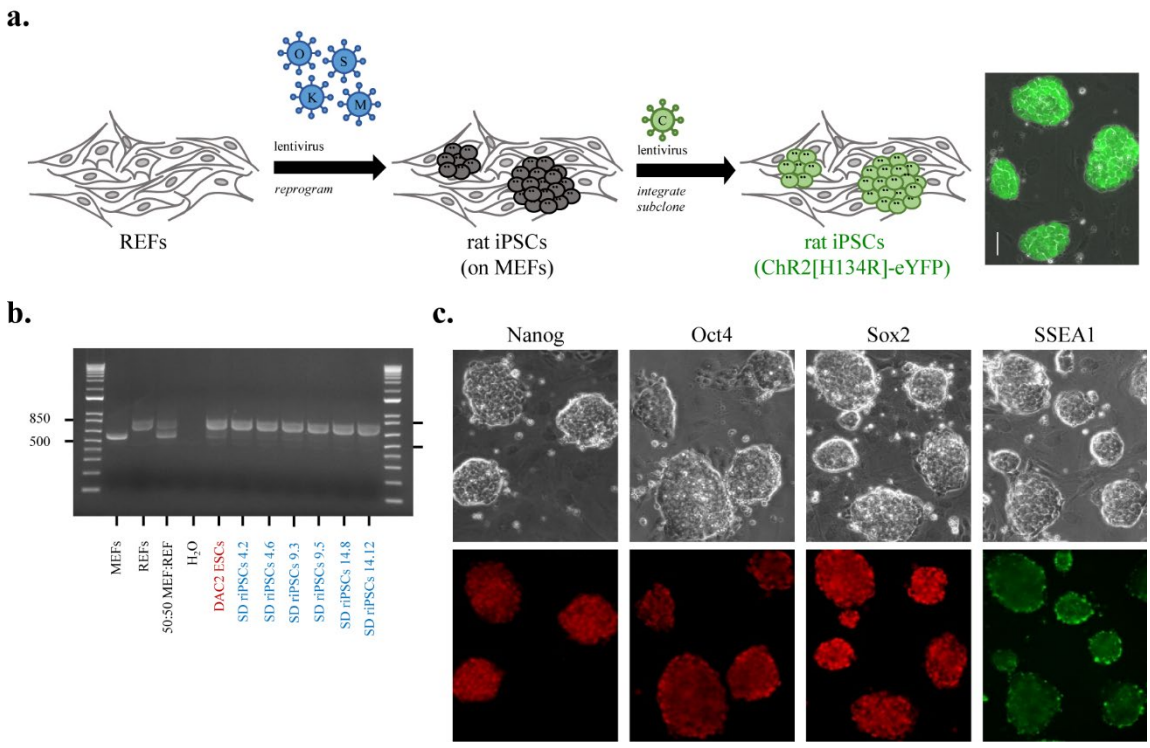

Figure 3.8: Generating rat iPSCs engineered to express channelrhodopsin.
(a) Schematic for generating rat iPSC subclones that express channelrhodopsin. REFs were reprogrammed with lentiviral vectors expressing Oct4, Sox2, Klf4, and c-Myc. Then a lentivirus encoding hChR2(H134R)-eYFP was integrated and sub clones were isolated based on the expression of eYFP. Scale bar is 50 μm.
(b) Agarose gel validates iPSC and ESC lines are rat and not mouse. Rat samples express ghost mouse bands due to feeder MEFs. Rat *Omp* band: 724 bp; Mouse *Omp* band: 580 bp.
(c) Staining validates rat iPSC sub clones express multiple pluripotency markers.

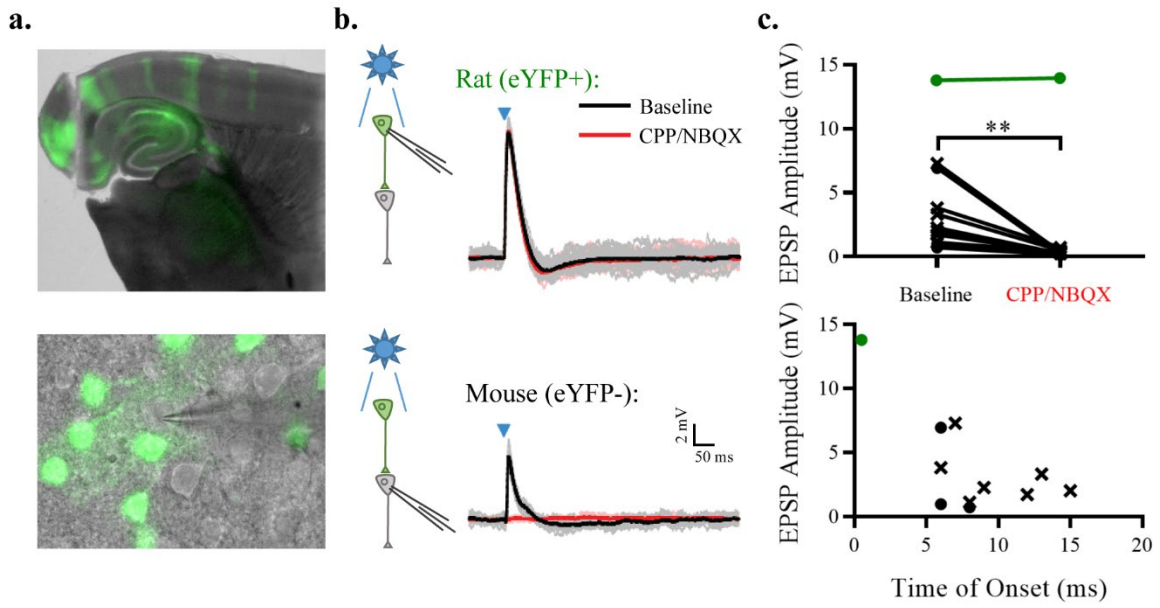

Figure 3.9: Rat neurons functionally innervate mouse neuronal targets.
(a) Acute transverse slice of 2-4 wk old chimera brain generated with SD riPSC 9.3 reveals rat columns in cortex and contribution throughout hippocampus (top). eYFP expression was used to guide a pipette (bottom) to eYFP+ rat or eYFP- mouse (shown) for patch-clamp electrophysiology recordings.
(b) Blue light was used to elicit electrical activity in eYFP+ rat cells. In rat cells, recorded activity may be directly caused by stimulation, whereas a signal in mouse neurons must be communicated from presynaptic rat neurons (left). Rat neurons showed a large depolarization upon blue light stimulation that did not change when AMPA and NMDA receptors were blocked with CPP and NBQX (top, right). Mouse neurons showed a smaller depolarization (EPSP) than rat neurons that was abolished by the addition of glutamate receptor antagonists (bottom, right). 20 individual traces for each condition are shown overlaid in bold with the average. Scale is 2 mV and 50 ms.
(c) Graphical quantification of the average EPSP amplitude for individual neurons demonstrates the EPSP in mouse neurons was significantly blocked by antagonists, whereas the depolarization was not altered in rat neurons (top). Furthermore, the response in mouse neurons appears delayed in comparison to direct stimulation in rat neurons (bottom). Green dots represent the rat cell, black marks are for mouse neurons, circles indicate hippocampal neuron, Xs indicate cortical neurons. Rat (1 cell): Baseline: 13.78, CPP/NBQX: 13.97; Mouse (10 cells): Baseline: 3.01, 1.31-4.71, CPP/NBQX: 0.32, 0.19-0.45. Mouse Baseline vs CPP/NBQX $p = 0.0056$. **$p < 0.01$.

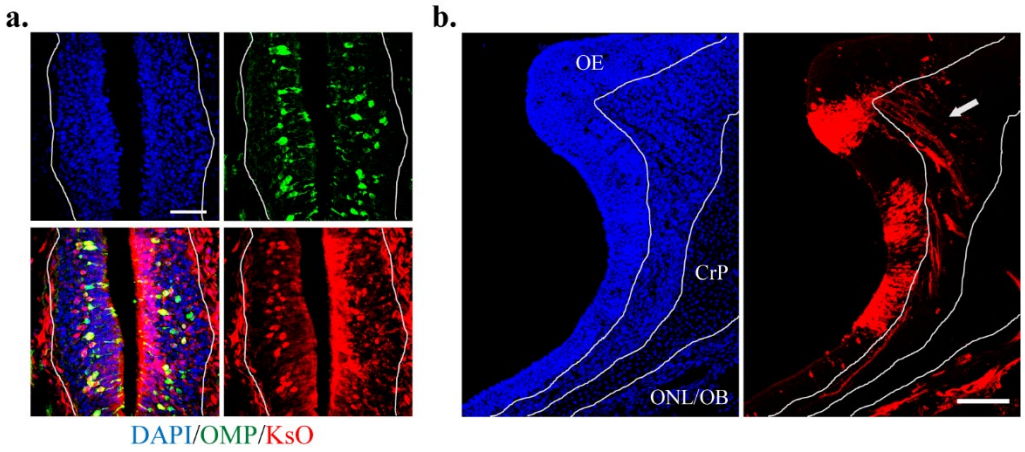

Figure 3.10: Rat complementation of OSNs in the mouse OE.
(a) Representative image of P0 chimera OE stained for OMP reveals rat OSNs develop and mature. Scale bar is 100 μm.
(b) Some sections show large columns of rat cells including OSNs with fibers directed toward the cribriform plate. Scale bar is 250 μm.

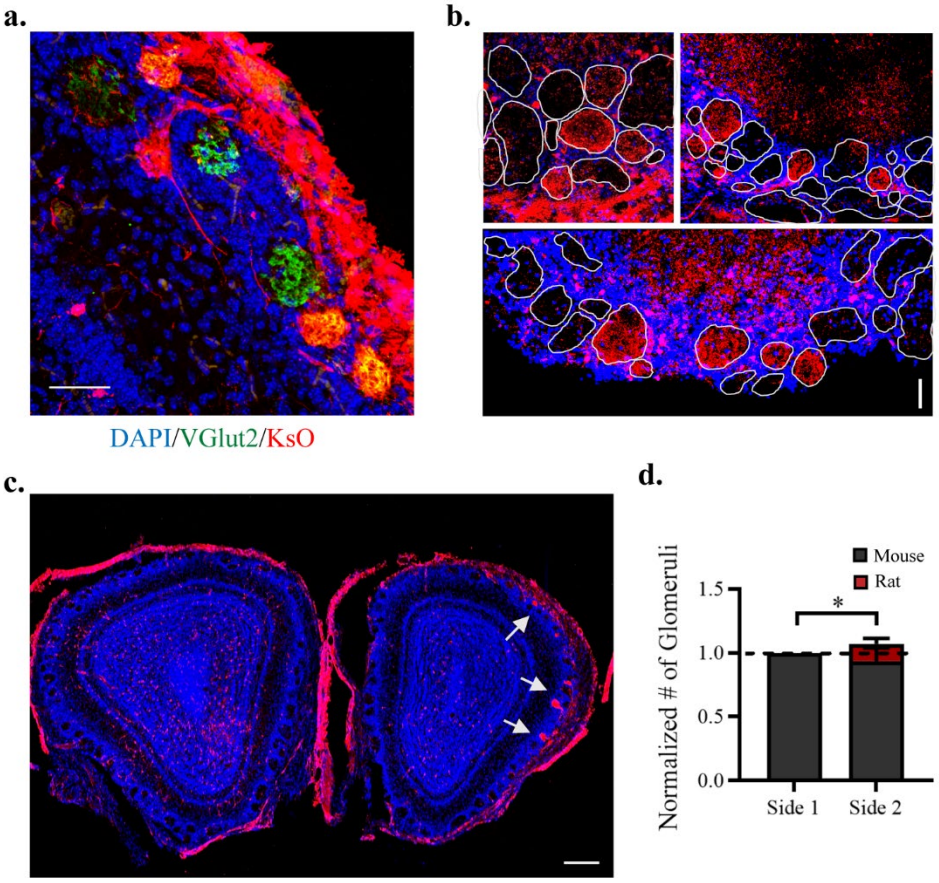

Figure 3.11: Rat OSNs target the mouse OB to form stable and distinct glomeruli.
(a) Representative image of a P10 OB stained for VGlut2 identifies glomerular structures built by rat axons. Scale bar is 50 μm.
(b) Images from a 2-yr-old chimera show rat glomeruli persist and are stable structures. Scale bar is 50 μm.
(c) Representative serial OB section demonstrates the unilateral formation of glomeruli in a P10 chimera. Scale bar is 250 μm.
(d) Graphical analysis of the number of glomeruli per hemisphere in chimeras with unilateral rat OSN contribution demonstrates rat glomeruli increase the total number of glomeruli in the mouse OB. 3 animals, 32 sections/animal. Side 2 was normalized to Side 1 for each animal. Bar and error is mean with 95% CI. Side 1: 1.00, 1.00-1.00; Mouse 1754 ± 108.9; Rat 0 ± 0; Side 2: 1.07, 0.97-1.18; Mouse 1640 ± 122.6; Rat 239.7 ± 14.57. Side 1 vs Side 2 $p = 0.0418$. Unpaired, two-sided t-test. *$p < 0.05$.

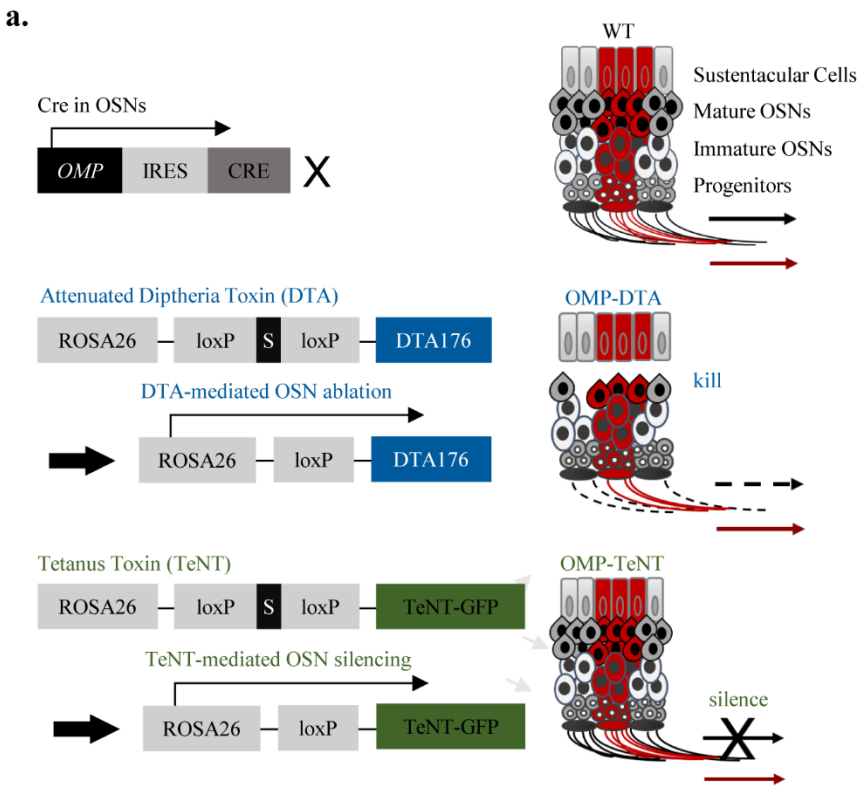

Figure 3.12: Genetic strategy to test for functional complementation in the mouse olfactory system.

(a) Cre is selectively co-expressed with Omp using IRES in OSNs. Crossing these mice with DTA mice causes the deletion of the stop codon to permit the expression of DTA in OSNs. This leads to ablation of mature OSNs and creates a structural and functional void for rat OSNs to fill (middle, right). Alternatively, crossing *OMP*-IRES-Cre mice with TeNT-GFP drives expression of TeNT in OSNs. This cross silences mature OSNs to create a functional void for rat OSNs but maintains structural integrity of the mouse OE (bottom, right).

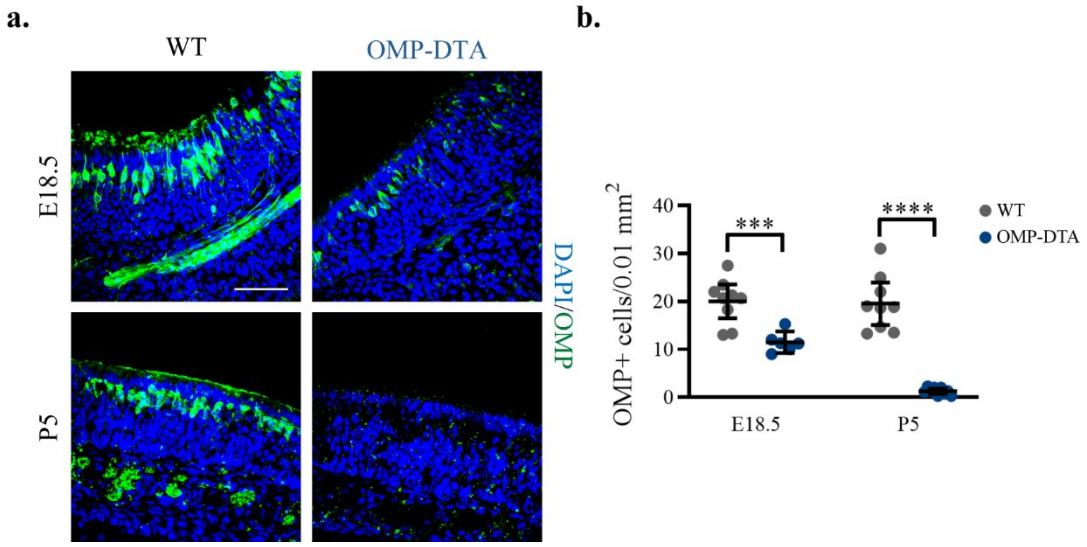

Figure 3.13: DTA expression successfully ablates OSNs in the mouse OE.
(a) Representative images of OE stained for OMP in WT and OMP-DTA animals reveal successful ablation of mature OSNs in P5 animals. Scale bar is 100 μm.
(b) Quantification of the density of OMP+ cells at E18.5 and P5 demonstrates a depletion of mature OSNs at both E18.5 and P5 in OMP-DTA animals. 2-3 animals/time point, 3 slices/animal. Bar and error represent mean with 95% CI. E18.5: WT (3 animals): 20.03, 16.47, 23.60; OMP-DTA (2 animals): 11.49, 9.21-13.76; P5: WT (3 animals): 19.55, 15.10-23.99; OMP-DTA (3 animals): 1.29, 0.73-1.85. E18.5 WT vs OMP-DTA $p = 0.0007$; P5 WT vs OMP-DTA $p < 0.0001$. Two-way ANOVA followed by Sidak's multiple comparisons test. ***$p < 0.001$, ****$p < 0.0001$.

Figure 3.14: OSN ablation is incomplete in aged animals but impacts OB architecture.
(a) Representative maximal coronal sections of WT and OMP-DTA OBs at P5 and P120+ highlight decreases in OMP-DTA OB size and organization. White rectangles denote insets shown below the corresponding whole OB image. Scale bar is 100 μm.
(b) Quantitative analysis demonstrate OMP-DTA OBs are smaller than WT at both P5 and P120+ mainly due to decreases in the GL and EPL. 4-5 animals/genotype, 3 slices/animal. Bar and error represent mean with 95% CI. Whole OB: P5: WT (5 animals): 2.13, 2.03-2.22; OMP-DTA (4 animals): 1.47, 1.32-1.63; P120+: WT (5 animals): 4.62, 4.44-4.80; OMP-DTA (5 animals): 2.53, 2.41-2.65. P5 WT vs OMP-DTA $p < 0.0001$; P120+ WT vs OMP-DTA $p < 0.0001$. GL: P5: WT: 0.59, 0.57-0.62; OMP-DTA: 0.22, 0.20-0.24; P120+: WT: 1.16, 1.09-1.23; OMP-DTA: 0.50, 0.43-0.57. P5 WT vs OMP-DTA $p < 0.0001$; P120+ WT vs OMP-DTA $p < 0.0001$. EPL: P5: WT: 0.53, 0.51-0.55; OMP-DTA: 0.32, 0.30-0.34; P120+: WT: 1.49, 1.42-1.55; OMP-DTA: 0.65, 0.58-0.73. P5 WT vs OMP-DTA $p < 0.0001$; P120+ WT vs OMP-DTA $p < 0.0001$. GCL: P5: WT: 1.01, 0.93-1.08; OMP-DTA: 0.93, 0.80-1.06; P120+: WT: 1.97, 1.82-2.11; OMP-DTA: 1.38, 1.31-1.46. P120+ WT vs OMP-DTA $p < 0.0001$. Glomeruli: P5: WT: 60.47, 57.42-63.51; OMP-DTA: 0, 0-0; P120+: WT: 96.58, 90.01-103.16; OMP-DTA: 16.73, 7.31-26.15. P5 WT vs OMP-DTA $p < 0.0001$; P120+ WT vs OMP-DTA $p < 0.0001$. Two-way ANOVA followed by Sidak's multiple comparisons test. ****$p < 0.0001$.

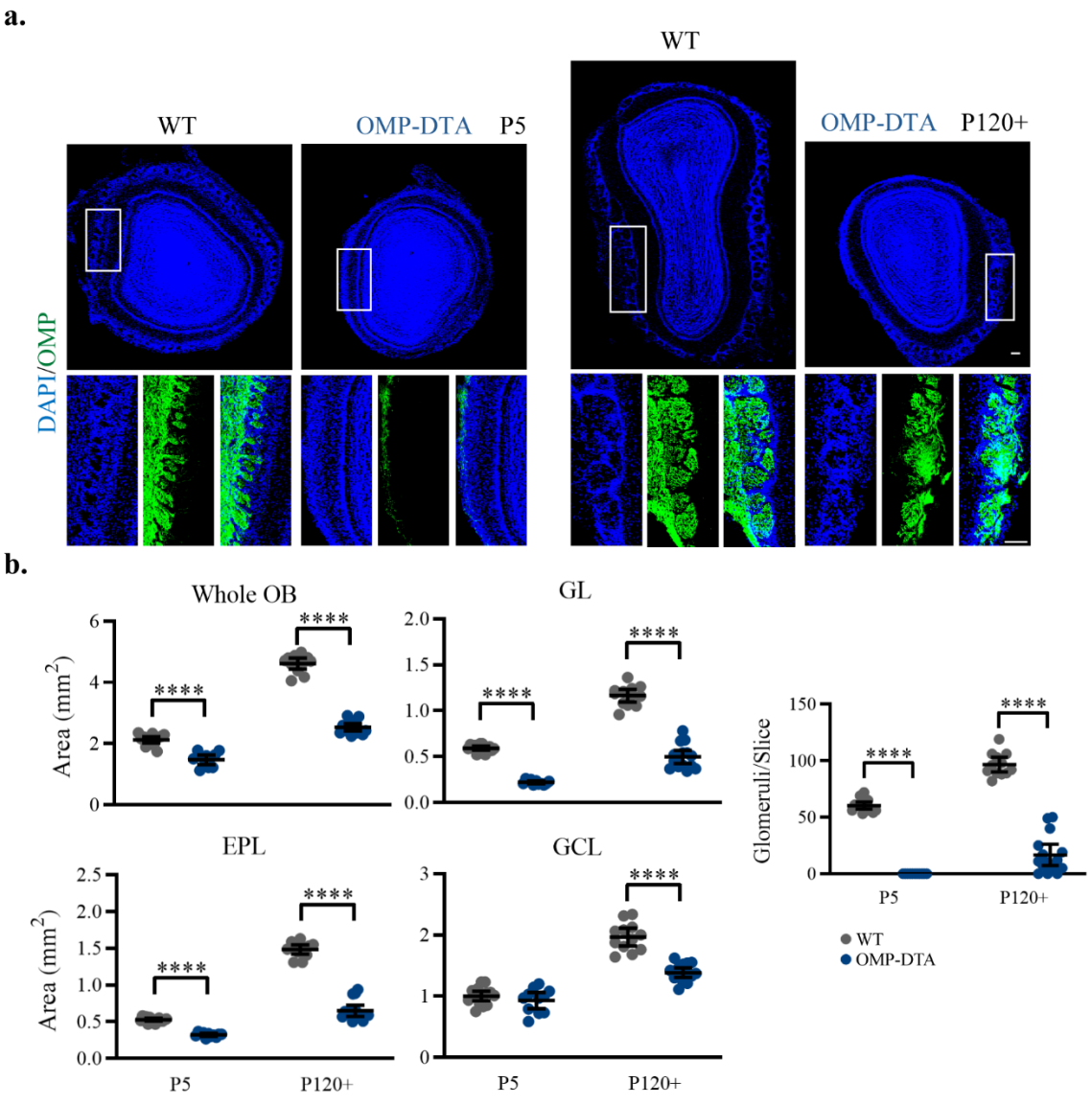
a.
WT
OMP-DTA P5
WT
OMP-DTA P120+
DAPI/OMP
b.
Whole OB
GL
EPL
GCL
Area (mm2)
Glomeruli/Slice
****
P5
P120+
WT
OMP-DTA

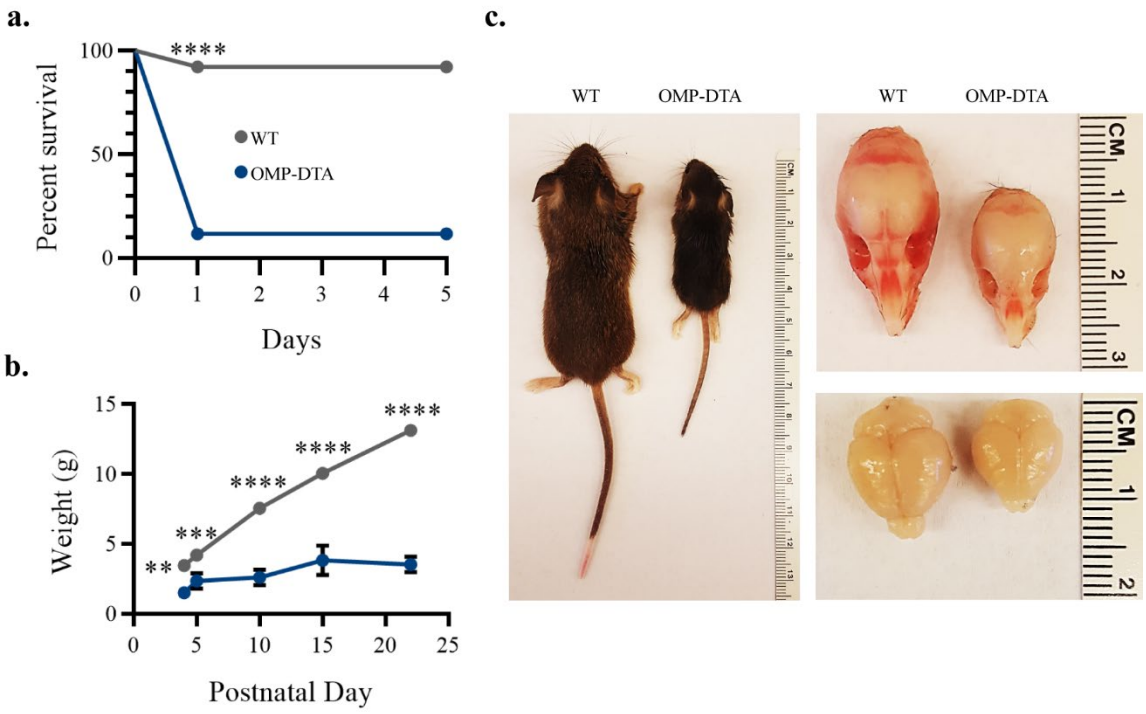

Figure 3.15: OSN ablation impacts animal survival and growth.
(a) Survival curves show OMP-DTA animals have a decreased survival rate within the first day of birth compared to WT littermates. 26 WT and 17 OMP-DTA animals, 4 litters. P0: 26 WT, 17 OMP-DTA; P1: 24 WT, 2 OMP-DTA; P2-P5: 24 WT, 2 OMP-DTA. WT vs OMP-DTA $p < 0.0001$. Mantel-Cox and Gehan-Breslow-Wilcoxon tests.
(b) Descriptive analysis of body weight shows OMP-DTA animals are significantly smaller than WT littermates as soon as 4 days following birth. 2-5 animals/genotype. Dots and error are mean with SD. P4: WT (3): 3.47 ± 0.15; OMP-DTA (2): 1.50 ± 0.14; P5: WT (3): 4.20 ± 0.23; OMP-DTA (5): 2.36 ± 0.57; P10: WT (3): 7.57 ± 0.29; OMP-DTA (2): 2.60 ± 0.57; P15: WT (3): 10.07 ± 0.21; OMP-DTA (2): 3.85 ± 1.06; P22: WT (3): 13.14 ± 0.09; OMP-DTA (2): 3.55 ± 0.57. P4 $p = 0.0015$. P5 $p = 0.001$, P10 $p < 0.0001$, P15 $p < 0.0001$, P22 $p < 0.0001$. Mixed-effects analysis with Sidak's multiple comparisons test. **$p < 0.01$, ***$p < 0.001$, ****$p < 0.0001$.
(c) Representative images of P21 animals highlight the difference in body size between WT and OMP-DTA animals.

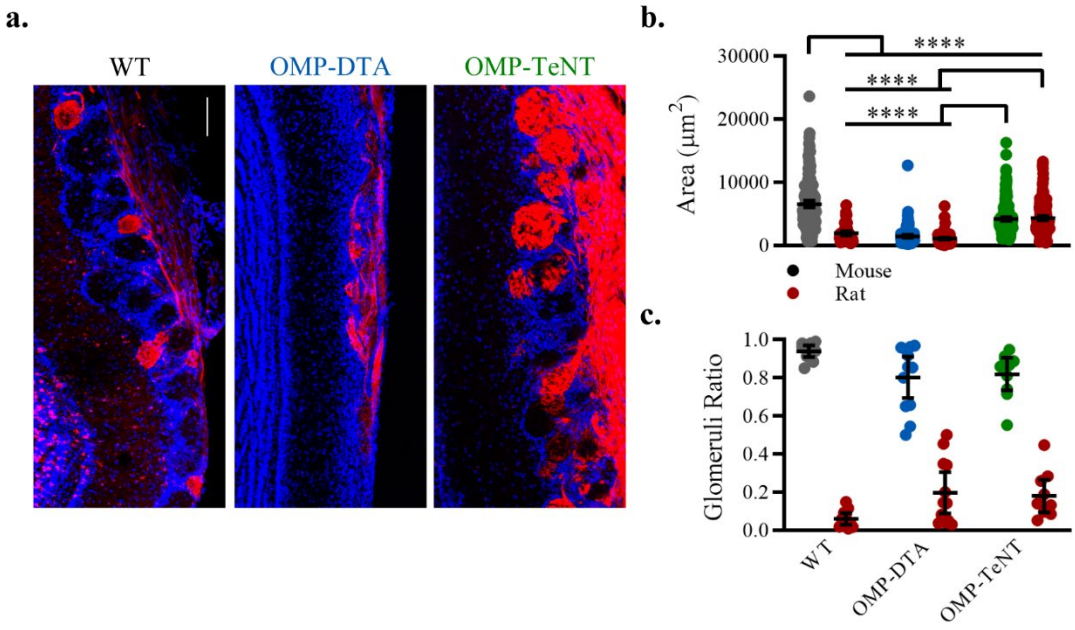

Figure 3.16: Rat OSN complementation is facilitated in OMP-TeNT mice.
(a) Representative images of OB sections reveals rat glomeruli form in all genetic backgrounds but appear to be larger in OMP-TeNT mice. Scale bar is 100 μm.
(b) Quantifications of glomerular area indicate rat glomeruli are largest in OMP-TeNT animals and only smaller than mouse in the WT background. 3-4 animals/genotype, 2-3 sections/animal. Bars and error represent mean with 95% CI. WT (4 animals): Mouse (191 glomeruli) 6547.66, 6011.03-7084.30; Rat (68): 1901.93, 1584.22-2219.64; OMP-DTA (4): Mouse (141): 1448.80, 1224.29-1673.31; Rat (145): 1085.60, 943.08-1228.12; OMP-TeNT (3): Mouse (260): 4157.82, 3861.22-4454.42; Rat (232): 4347.61, 3995.76-4699.47. WT mouse vs WT rat $p < 0.0001$, WT mouse vs OMP-DTA mouse $p < 0.0001$, WT mouse vs OMP-DTA rat $p < 0.0001$, WT mouse vs OMP-TeNT mouse $p < 0.0001$, WT mouse vs OMP-TeNT rat $p < 0.0001$, OMP-TeNT mouse vs WT rat $p < 0.0001$, OMP-TeNT mouse vs OMP-DTA mouse $p < 0.0001$, OMP-TeNT mouse vs OMP-DTA rat $p < 0.0001$, OMP-TeNT rat vs WT rat $p < 0.0001$, OMP-TeNT rat vs OMP-DTA mouse $p < 0.0001$, OMP-TeNT rat vs OMP-DTA rat $p < 0.0001$. Two-way ANOVA followed by Tukey's multiple comparisons test. ****$p < 0.0001$.
(c) The ratio of rat or mouse glomeruli does not change in any genotype. 3-4 animals/genotype, 2-3 sections/animal. Bars and error represent mean with 95% CI. WT (4 animals, 11 sections): mouse: 0.94, 0.91-0.97; rat: 0.06, 0.03-0.09; OMP-DTA (4, 12): mouse: 0.80, 0.69-0.91; rat: 0.20, 0.09-0.31; OMP-TeNT (3, 10): mouse: 0.82, 0.73-0.91; rat: 0.18, 0.10-0.27. Two-way ANOVA followed by Tukey's multiple comparisons test.

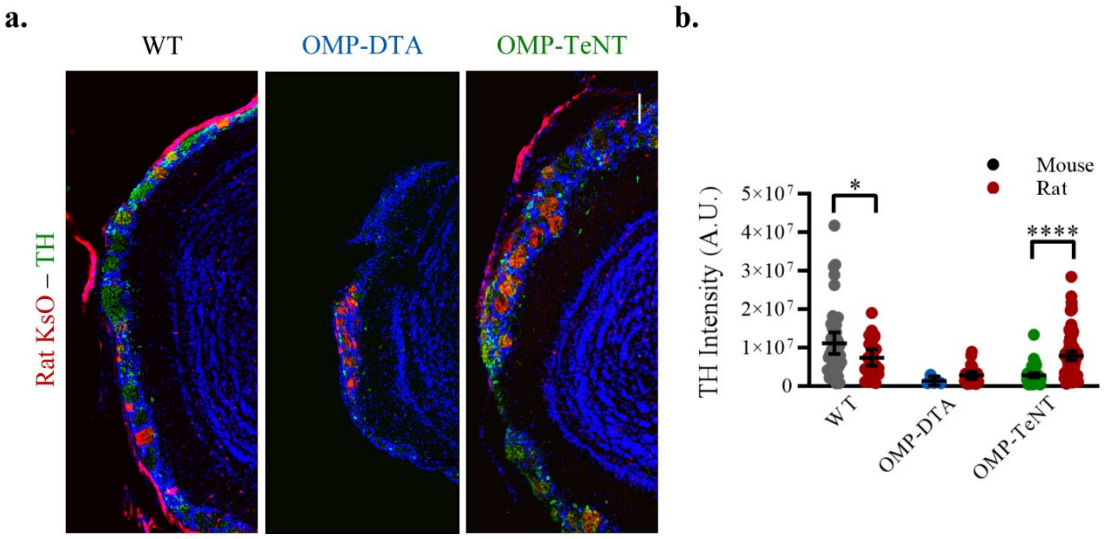

Figure 3.17: Rat OSN complementation in OMP-TeNT mice drives OB activity.
(a) Representative images of OB sections stained for the immediate early gene TH indicate rat glomeruli drive TH expression in innervating periglomerular neurons. Scale bar is 100 µm.
(b) Quantifications of TH intensity reveal rat glomeruli in OMP-TeNT OBs drive circuit activity, whereas mouse glomeruli may be preferred in WT. 1 animal/genotype, 3 sections/animal. Bars and error represent mean with 95% CI. WT: Mouse (44 glomeruli) 11.16e6, 8.39e6-13.92e6; Rat (23): 7.39e6, 5.26e6-9.52e6; OMP-DTA: Mouse (5): 1.34e6, 0.17e6-2.51e6; Rat (25): 2.76e6, 1.83e6-3.68e6; OMP-TeNT: Mouse (60): 2.81e6, 2.28e6-3.34e6; Rat (95): 7.86e6, 6.71e6-9.01e6. WT mouse vs WT rat $p = 0.0248$, OMP-TeNT mouse vs OMP-TeNT rat $p < 0.0001$. Two-way ANOVA followed by Sidak's multiple comparisons test. *$p < 0.05$, ****$p < 0.0001$.

Figure 3.18: Mouse PC activity is shaped by rat OSNs.
(a) Representative images of PC sections stained for the immediate early gene cFos show increased expression in hemispheres with rat OSN complementation. Scale bar is 100 μm.
(b) Quantifications of cFos staining density reveal rat OSNs drive PC activity in transgenic mice. 2 animals/genotype, 15 sections/animal. Bars and error represent mean with 95% CI. WT: Uncomplemented: 1.00, 0.67-1.33; OSN Complemented: 0.97, 0.69-1.25; OMP-DTA: Uncomplemented: 1.00, 0.89-1.11; OSN Complemented: 2.09, 1.72-2.46; OMP-TeNT: Uncomplemented: 1.00, 0.84-1.17; OSN Complemented: 1.53, 1.33-1.73. OMP-DTA Uncomplemented vs OMP-DTA OSN Complemented $p < 0.0001$, OMP-TeNT Uncomplemented vs OMP-TeNT OSN Complemented $p = 0.0079$. Two-way ANOVA followed by Sidak's multiple comparisons test.
(c) Representative images of PC sections stained for the immediate early gene Egr1 show altered expression with rat OSN complementation. Scale bar is 100 μm.
(d) Quantifications of Egr1 staining density corroborate cFos results in OMP-TeNT chimeras. 2 animals/genotype, 15 sections/animal. Bars and error represent mean with 95% CI. WT: Uncomplemented: 1.00, 0.66-1.34; OSN Complemented: 0.67, 0.45-0.90; OMP-DTA: Uncomplemented: 1.00, 0.73-1.27; OSN Complemented: 1.23, 0.74-1.71; OMP-TeNT: Uncomplemented: 1.00, 0.69-1.31; OSN Complemented: 1.63, 1.23-2.04. OMP-TeNT Uncomplemented vs OMP-TeNT OSN Complemented $p = 0.0113$. Two-way ANOVA followed by Sidak's multiple comparisons test. *$p < 0.05$, **$p < 0.01$, ****$p < 0.0001$.

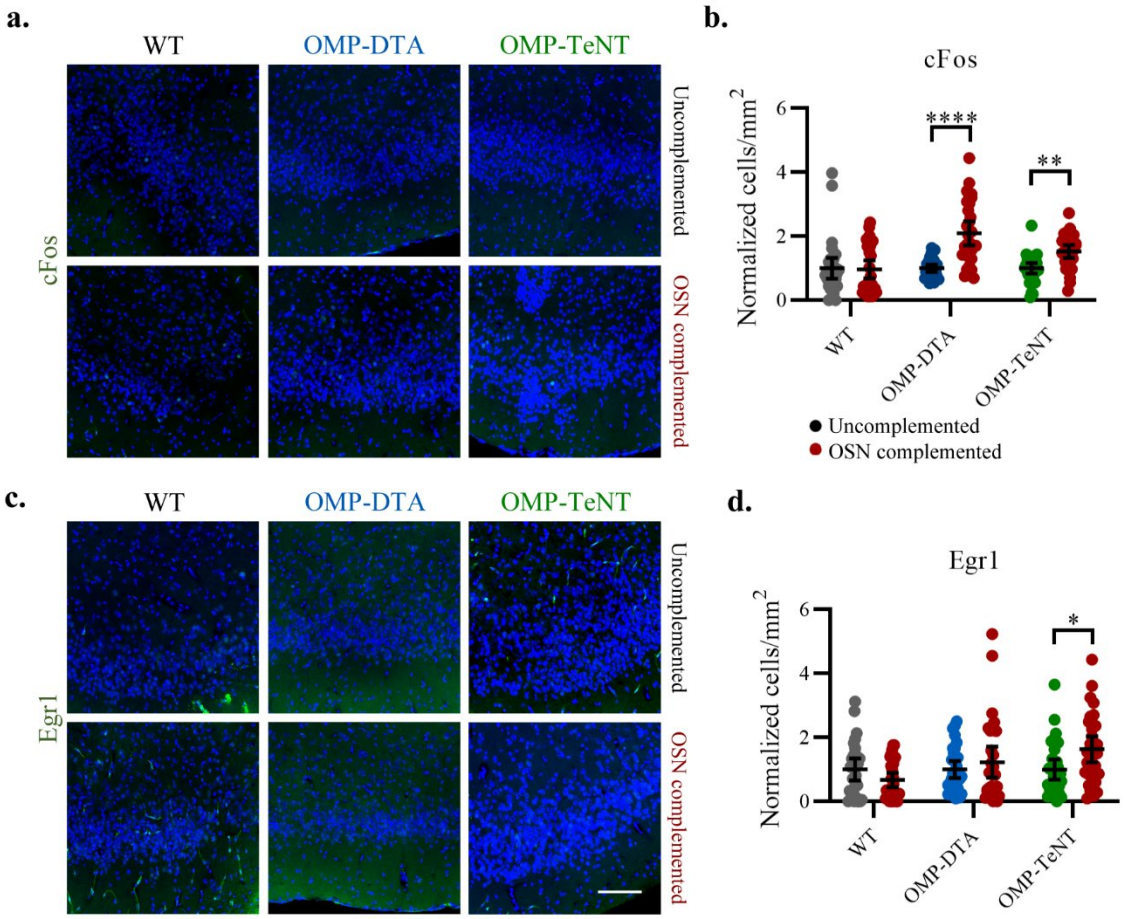
a.
WT
OMP-DTA
OMP-TeNT
cFos
Uncomplemented
OSN complemented
b.
cFos
Normalized cells/mm2
****
**
WT
OMP-DTA
OMP-TeNT
Uncomplemented
OSN complemented
c.
WT
OMP-DTA
OMP-TeNT
Egr1
Uncomplemented
OSN complemented
d.
Egr1
Normalized cells/mm2
*
WT
OMP-DTA
OMP-TeNT

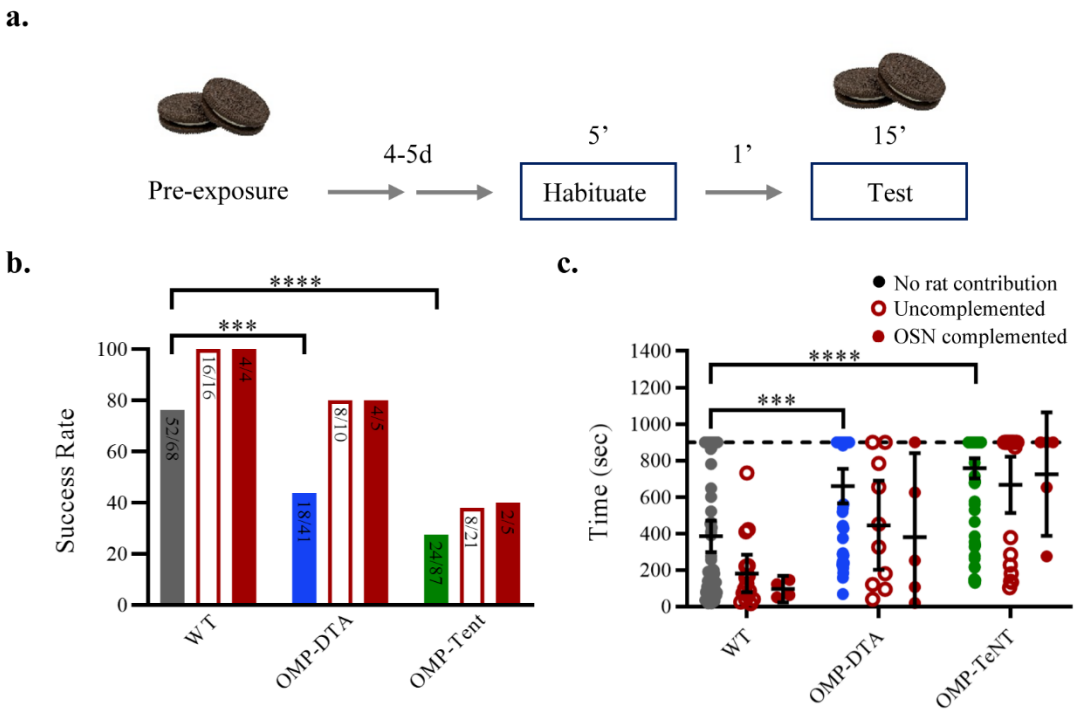

Figure 3.19: Olfactory behavior phenotype unresolved with rat OSN complementation.
(a) Schematic of buried cookie paradigm including pre-exposure, habituation, and testing.
(b) Quantifications of successful trials show olfactory deficits decrease the success rate for mice to find the cookie, but rat OSN complementation does not significantly rescue this behavior. Bars represents % and numbers detail the ratio. N: WT: 52/68, 16/16, 4/4; OMP-DTA: 18/41, 8/10, 4/5; OMP-TeNT: 24/87, 8/21, 2/5. WT (no contribution) vs OMP-DTA (no contribution) $p = 0.0009$, WT (no contribution) vs OMP-TeNT (no contribution) $p< 0.0001$. Fisher's exact tests, two-sided.
(c) The time to find the cookie is not apparently impacted by rat OSN complementation. Bars and error represent mean with 95% CI. WT: No rat contribution: 385.11, 299.16-471.06; Uncomplemented: 181.50, 79.06-283.94; OSN Complemented: 96.25, 23.14-169.36; OMP-DTA: No rat contribution: 660.66, 565.60-755.72; Uncomplemented: 445.85, 201.72-689.98; OSN Complemented: 381.26, -79.125-841.65; OMP-TeNT: No rat contribution: 758.00, 703.23-812.77; Uncomplemented: 667.86, 513.98-821.74; OSN Complemented: 726.00, 386.80-1065.20. WT (no contribution) vs OMP-DTA (no contribution) $p = 0.0002$, WT (no contribution) vs OMP-TeNT (no contribution) $p< 0.0001$. Two-way ANOVA followed by Tukey's multiple comparisons test. ***$p < 0.001$, ****$p < 0.0001$.

References

Balaban, E., Teillet, M.A., and Le Douarin, N. (1988) Application of the quail-chick chimera system to the study of brain development and behavior. Science 241(4871): 1339–1342.

Barry, C., Schmitz, M.T., Jiang, P., Schwartz, M.P., Duffin, B.M., Swanson, S., Bacher, R., Bolin, J.M., Elwell, A.L., McIntosh, B.E., Steward, R., and Thomson, J.A. (2018) Species-specific developmental timing is maintained by pluripotent stem cells ex utero. Developmental Biology 423(2): 101–110.

Belluscio, L., Lodovichi, C., Feinstein, P., Mombaerts, P., and Katz, L.C. (2002). Odorant receptors instruct functional circuitry in the mouse olfactory bulb. Nature 419(6904): 296–300.

Boland, M.J., Hazen, J.L., Nazor, K.L., Rodriguez, A.R., Gifford, W., Marting, G., Kupriyanov, S., and Baldwin K.K. (2009) Adult mice generated from induced pluripotent stem cells. Nature 461(7260): 91–94.

Bozza, T., Feinstein, P., Zheng, C., and Mombaerts, P. (2002). Odorant receptor expression defines functional units in the mouse olfactory system. Journal of Neuroscience 22(8): 3033–3043.

Buchsbaum, I.Y., and Cappello, S. (2019). Neuronal migration in the CNS during development and disease: insights from in vivo and in vitro models. Development 146(1).

Chang, A.N., Liang, Z., Dai, H.Q., Chapdelaine-Williams, A.M., Andrews, N., Bronson, R.T., Schwer, B., and Alt, F.W. (2018). Neural blastocyst complementation enables mouse forebrain organogenesis. Nature 563(7729): 126–130.

Chen, J., Lansford, R., Stewart, V., Young, F., and Alt., F.W. (1993). RAG-2-deficient blastocyst complementation: an assay of gene function in lymphocyte development. Proceedings of the National Academy of Sciences of the United States of America 90(10): 4528–4532.

Constantine-Paton, M., and Caprianica, R.R. (1975). Central projection of optic tract from translocated eyes in the leopard frog (Rana pipiens). Science 189(4201): 480–482.

Eggan, K., Baldwin, K., Tackett, M., Osborne, J., Gogos, J., Chess, A., Axel, R., and Jaenisch, R. (2004). Mice cloned from olfactory sensory neurons. Nature 428(6978): 44–49.

Elliott, K.L., Houston, D.W., and Fritzsch, B. (2015). Sensory afferent segregation in three-eared frogs resemble the dominance columns observed in three-eyed frogs. Scientific Reports 5:8338.

Espuny-Camacho, I., Michelsen, K.A., Gall, D., Linaro, D., Hasche, A., Bonnefont, J., Bali, C., Orduz, D., Bilheu, A., Herpoel, A., Lambert, N., Gaspard, N., Péron, S., Schiffmann, S.N., Giugliano, M., Gaillard, A., and Vanderhaeghen, P. (2013). Pyramidal neurons derived from human pluripotent stem cells integrate efficiently into mouse brain circuits in vivo. Neuron 77(3): 440–456.

Espuny-Camacho, I., Michelsen, K.A., Linaro, D., Bilheu, A., Acosta-Verdugo, S., Herpoel, A., Giugliano, M., Gaillard, A., and Vanderhaeghen, P. (2018) Human pluripotent stem-cell-derived cortical neurons integrate functionally into the lesioned adult murine visual cortex in an area-specific way. Cell Reports 23(9): 2732–2743.

Falkner, S., Grade, S., Dimou, L., Conzelmann, K.K., Bonhoeffer, T., Götz, M., and Hübener, M. (2016). Transplanted embryonic neurons integrate into adult neocortical circuits. Nature 539(7628): 248–253.

Franks, K.M., and Isaacson, J.S. (2005). Synapse-specific downregulation of NMDA receptors by early experience: a critical period for plasticity of sensory input to olfactory cortex. Neuron 47(1): 101–14.

Gaspard, N., Bouschet, T., Hourez, R., Dimidschstein, J., Naeije, G., van den Ameele, J., Espuny-Camacho, I., Herpoel, A., Passante, L., Schiffmann, S.N., Gaillard, A., and Vanderhaeghen, P. (2008) An intrinsic mechanism of corticogenesis from embryonic stem cells. Nature 455(7211): 351–357.

Go, W.Y., and Ho, S.N. (2002). Optimization and direct comparison of the dimerizer and reverse tet transcriptional control systems" Journal of Gene Medicine 4(3): 258–270.

Greig, L.C., Woodworth, M.B., Galazo, M.J., Padmanabhan, H., and Macklis, J.D. (2013). Molecular logic of neocortical projection neuron specification, development and diversity. Nature Reviews Neuroscience 14(11): 755–769.

Gogos, J.A., Osborne, J., Nemes, A., Mendelsohn, M., and Axel, R. (2000). Genetic ablation and restoration of the olfactory topographic map. Cell 103(4): 609–620.

Isotani, A., Hatayama, H., Kaseda, K., Ikawa, M., and Okabe, M. (2010). Formation of a thymus from rat ES cells in xenogeneic nude mouse↔rat ES chimeras. Genes to Cells 16(4): 397–405.

Isotani, A., Yamagata, K., Okabe, M., and Ikawa, M. (2016) Generation of Hprt-disrupted rat through mouse←rat ES chimeras. Scientific Reports 6: 24215.

James, K.N. (2013). Static and dynamic aspects of olfactory processing circuits. University of California, San Diego: PhD dissertation.

Kim, H.H., Puche, A.C., and Margolis, F.L. (2006). Odorant deprivation reversibly modulates transsynaptic changes in the NR2B-mediated CREB pathway in mouse piriform cortex. Journal of Neuroscience 26(37): 9548–9959.

Kim, Y., Yang, G.R., Pradhan, K., Venkataraju, K., Bota, M., Del Molino, L.C.G., Fitzgerald, G., Ram, K., He, M., Levine, J.M., Mitra, P., Huang, Z.J., Wang, X.J., and Osten, P. (2017). Brain-wide maps reveal stereotyped cell-type-based cortical architecture and subcortical sexual dimorphism. Cell 171(2): 456–469.

Kobayashi, T., Yamaguchi, T., Hamanaka, S., Kato-Itoh, M., Yamazaki, Y., Ibata, M., Sato, H., Lee, Y.S., Usui, J., Knisely, A.S., Hirabayashi, M., and Nakauchi, H. (2010). Generation of rat pancreas in mouse by interspecific blastocyst injection of pluripotent stem cells. Cell 142(45): 787–799.

Li, P., Tong, C., Mehrian-Shai, R., Jia, L., Wu, N., Yan, Y., Maxson, R.E., Schulze, E.N., Song, H., Hsieh, C.L., Pera, M.F., and Ying, Q.L. (2008). Germline competent embryonic stem cells derived from rat blastocysts. Cell 135(7): 1299–1310.

Linaro, D., Vermaercke, B., Iwata, R., Ramaswamy, A., Libé-Philippot, B., Boubakar, L., Davis, B.A., Wierda, K., Davie, K., Poovathingal, S., Penttila, P.A., Bilheu, A., De Bruyne, L., Gall, D., Conzelmann, K.K., Bonin, V., and Vanderhaeghen, P. (2019) Xenotransplanted human cortical neurons reveal species-specific development and functional integration into mouse visual circuits. Neuron 104(5): 972–986.

Mansour, A.A., Gonçalves, J.T., Bloyd, C.W., Li, H., Fernandes, S., Quang, D., Johnston, S., Parylak, S.L., Jin, X., and Gage, F.H. (2018). An in vivo model of functional and vascularized human brain organoids. Nature Biotechnology 36(5): 432–441.

McLean, J.H., and Shipley, M.T. (1988) Postmitotic, postmigrational expression of tyrosine hydroxylase in olfactory bulb dopaminergic neurons. Journal of Neuroscience 8(10): 3658–3669.

Molyneaux, B.J., Arlotta, P., Menezes, J.R., and Macklis, J.D. (2007). Neuronal subtype specification in the cerebral cortex. Nature Reviews Neuroscience 8(6): 427–437.

Pacitti, D., Privolizzi, R., and Bax, B.E. (2019). Organs to cells and cells to organoids: the evolution of in vitro central nervous system modelling. Frontiers in Cellular Neuroscience 13:129.

Pologruto, T.A., Sabatini, B.L., and Svoboda, K. (2003). ScanImage: flexible software for operating laser scanning microscopes. Biomedical Engineering Online 2:13.

Schindelin, J., Arganda-Carreras, I., Frise, E., Kaynig, V., Longair, M., Pietzsch, T., Preibisch, S., Rueden, C., Saalfeld, S., Schmid, B., Tinevez, J.-Y., White, D.J., Hartenstein, V., Eliceiri, K., Tomancak, P., and Cardona, A. (2012). Fiji: an open-source platform for biological-image analysis. Nature Methods 9(7): 671–675.

Schneider, S.P., and Scott, J.W. (1983). Orthodromic response properties of rat olfactory bulb mitral and tufted cells correlate with their projection patterns. Journal of Neurophysiology 50(2): 358–378.

Scott, J.W. (1981). Electrophysiological identification of mitral and tufted cells and distributions of their axons in olfactory system of the rat. Journal of Neurophysiology 46(5): 918–931.

Semple, B.D., Blomgren, K., Gimlin, K., Ferriero, D.M., and Noble-Haeusslein, L.J. (2013). Brain development in rodents and humans: identifying benchmarks of maturation and vulnerability to injury across species. Progress in Neurobiology 106–107: 1–16.

Shen, Q., Wang, Y., Dimos, J.T., Fasano, C.A., Phoenix, T.N., Lemischka, I.R., Ivanova, N.B., Stifani, S., Morrisey, E.E., and Temple, S. (2006). The timing of cortical neurogenesis is encoded within lineages of individual progenitor cells. Nature Neuroscience 9(6): 743–751.

Stettler, D.D., and Axel, R. (2009). Representations of odor in the piriform cortex. Neuron 63(6): 854–864.

Voehringer, D., Liang, H.E., and Locksley, R.M. (2008). Homeostasis and effector function of lymphopenia-induced 'memory-like' T cells in constitutively T cell-depleted mice. Journal of Immunology 180(7): 4742–4753.

Wu, J., Okamura, D., Li, M., Suzuki, K., Luo, C., Ma, L., He, Y., Li, Z., Benner, C., Tamura, I., Krause, M.N., Nery, J.R., Du, T., Zhang, Z., Hishida, T., Takahashi, Y., Aizawa, E., Young Kim, N., Lajara, J., Guillen, P., Campistol, J.M., Rodriguez Esteban, C., Ross, P.J., Saghatelian, A., Ren, B., Ecker, J.R., and Izpisua Belmonte, J.C. (2015). An alternative pluripotent state confers interspecies chimaeric competency. Nature 521(7552): 316–321.

Wu, J., Platero-Luengo, A., Sakurai, M., Sugawara, A., Gil, M.A., Yamauchi, T., Suzuki, K., Bogliotti, Y.S., Cuello, C., Morales Valencia, M., Okumura, D., Luo, J., Vilarino, M., Parrilla, I., Soto, D.A., Martinez, C.A., Hishida, T., Sanchez-Bautista, S., Martinez-Martinez, M.L., Wang, H., Nohalez, A., Aizawa, E., Martinez-Redondo, P., Ocampo, A., Reddy, P., Roca, J., Maga, E.A., Esteban, C.R., Berggren, W.T., Nunez Delicado, E., Lajara, J., Guillen, I., Guillen, P., Campistol, J.M., Martinez, E.A., Ross, P.J., and Izpisua Belmonte, J.C. (2017). Interspecies Chimerism with Mammalian Pluripotent Stem Cells. Cell 168(3): 473–486.

Yamaguchi, T., Sato, H., Kato-Itoh, M., Goto, T., Hara, H., Sanbo, M., Mizuno, N., Kobayashi, T., Yanagida, A., Umino, A., Ota, Y., Hamanaka, S., Masaki, H., Rashid, S.T., Hirabayashi, M., and Nakauchi, H. (2017). Interspecies organogenesis generates autologous functional islets. Nature 542(7640): 191–196.

Young, J.M., Friedman, C., Williams, E.M., Ross, J.A., Tonnes-Priddy, L., and Trask, B.J. (2002). Different evolutionary processes shaped the mouse and human olfactory receptor gene families. Human Molecular Genetics 11(5): 535–546.

Zhang, F., Wang, L.P., Brauner, M., Liewald, J.F., Kay, K., Watzke, N., Wood, P.G., Bamberg, E., Nagel, G., Gottschalk, A., and Deisseroth, K. (2007). Multimodal fast optical interrogation of neural circuitry. Nature 446(7136): 633–639.

Zhang, X., and Firestein, S. (2002). The olfactory receptor gene superfamily of the mouse. Nature Neuroscience 5(2): 124–133.

Zhang, X., Zhang, X., and Firestein, S. (2007) Comparative genomics of odorant and pheromone receptor genes in rodents. Genomics 89(4): 441–450.

Zhang, Y., Narayan, S., Geiman, E., Lanuza, G.M., Velasquez, T., Shanks, B., Akay, T., Dyck, J., Pearson, K., Gosgnach, S., Fan, C.M., and Goulding, M. (2008). V3 spinal neurons establish a robust and balanced locomotor rhythm during walking. Neuron 60(1): 84–96.